

國立交通大學

應用化學系博士班

博士論文

高電容量錫基奈米結構作為鋰離子電池
之陽極

High Capacity Tin-Based Nanostructures as
Anodes for Lithium-Ion Batteries

研究生：許凱捷

指導教授：裘性天 教授

李紫原 教授

中華民國一百零三年九月

高電容量錫基奈米結構作為鋰離子電池
之陽極

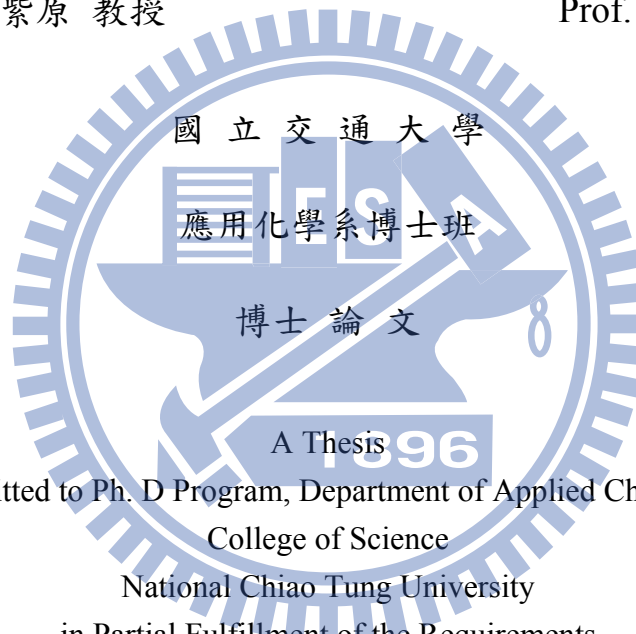
High Capacity Tin-Based Nanostructures as
Anodes for Lithium-Ion Batteries

研究生：許凱捷

Student : Kai-Chieh Hsu

指導教授：裘性天 教授
李紫原 教授

Advisor : Prof. Hsin-Tien Chiu
Prof. Chi-Young Lee



Submitted to Ph. D Program, Department of Applied Chemistry
College of Science
National Chiao Tung University
in Partial Fulfillment of the Requirements
for the Degree of Doctor
in
Applied Chemistry
September 2014
Hsinchu, Taiwan, Republic of China

中華民國一百零三年九月

High Capacity Tin-Based Nanostructure as Anodes for Lithium-Ion Batteries

Student: Kai-Chieh Hsu
Advisor: Dr. Hsin-Tien Chiu
Dr. Chi-Young Lee

Abstract

In this studies, we demonstrate the synthesis of tin-based nanostructures include SnO₂ nanorods (NRs), hollow spheres (HSs), nanosheets (NSs) and Sn@C core-shell nanowires (NWs) without the usage of template and catalysts. Growth mechanism and electrochemical properties of tin-based samples were also investigated.

First, phase-segregated SnO₂ nanorods (NRs, length 1-2 μm and diameter 10-20 nm) were developed in a matrix of CaCl₂ salt by reacting CaO particles with a flowing mixture of SnCl₄ and Ar gases at elevated temperatures *via* a vapor–solid reaction growth (VSRG) pathway. And developed a facile hydrothermal method to synthesize SnO₂ hollow spheres (HSs) and nanosheets (NSs). The morphologies and structures of SnO₂ could be controlled by Sn^{+4/+2} precursors. The shell thickness of the HSs was around 200 nm with diameter 1-3 μm, while thickness of the NSs was 40 nm. The correlation between the morphological characteristics and the electrochemical properties of SnO₂ NRs, HSs and NSs were discussed. The SnO₂ nanomaterials were investigated as a potential anode material for Li-ion batteries (LIBs). SnO₂ NRs, HSs and NSs exhibit superior electrochemical performance and deliver 435, 522 and 490 mA h g⁻¹ up to the one hundred cycles at a current density of 100 mA g⁻¹ (0.13 C), which is ascribed to the unique structure of SnO₂ which be surrounded in the inactive amorphous byproduct matrix. The matrix probably buffered and reduced the stress caused by the volume change of the electrode during the charge-discharge cyclings.

Development tin-based nanocomposites containing suitably chosen matrix elements to achieve higher performance and reduce irreversibility processes. Designed strategy to fabricate a novel tin-carbon nanocomposites as electrodes of LIBs. Sn@C core-shell nanowires (NWs) were synthesized by reacting SnO₂ particles with a flowing mixture of C₂H₂ and Ar gases at elevated temperatures. The overall diameter of the core-shell nanostructure was 100-350 nm. The C shell thickness was 30-70 nm. The NW length was several micrometers. Inside the shell, a void space was found. The reaction is proposed to be *via* a vapor-solid reaction growth (VSRG) pathway. The NWs were investigated as a potential anode material for Li-ion batteries (LIBs). The half-cell constructed from the as-fabricated electrode and a Li foil exhibited a reversible capacity of 525 mA h g⁻¹ after one hundred cycles at a current density of 100 mA g⁻¹. At a current density as high as 1000 mA g⁻¹, the battery still maintained a capacity of 486 mA h g⁻¹. The excellent performance is attributed to the unique 1D core-shell morphology. The core-shell structure and the void space inside the shell can accommodate large volume changes caused by the formation and decomposition of Li_xSn alloys in the charge-discharge steps.

高電容量錫基奈米結構作為鋰離子電池之陽極

研究生：許凱捷

指導教授：裘性天 博士

李紫原 博士

摘要

此次研究中，我們提出在不使用模板與金屬催化劑的環境下，合成出錫基奈米結構，其中包含奈米棒、空球狀、奈米片狀之二氧化錫以及碳材包覆金屬錫之核殼一維奈米線作為陽極材料。此外，本研究也對錫基奈米結構的成長機制以及電化學性質作了詳細的探討。

首先，藉由氣固相反應，以氧化鈣及四氯化錫作為前驅物，氫氣作為載流氣體之環境，合成出具有相分離奈米棒之二氧化錫(短軸為 10-20 奈米長度；長軸為 1-2 微米長度)及氯化鈣鹽類。接著，藉由水熱法以不同的+4/+2 價態錫之前驅物，合成出空球狀、奈米片狀之二氧化錫，其中空球之殼厚大約為 200 奈米厚度，球狀大小為 1-3 微米長度；片狀為 40 奈米厚度。根據實驗所觀察之結果，提出成長機制，藉其嘗試了解成長過程。並且進一步討論，在電化學性質上與不同形貌奈米棒、空球狀、奈米片狀之二氧化錫之間相關性。電池測試方面，以二氧化錫奈米結構作為電極(充放電速率為 100 mA g^{-1})，奈米棒、空球狀、奈米片狀之二氧化錫經過 100 次循環充放電分別有 435、522

以及 490 mA h g^{-1} ，其效能表現優異，主要原因為二氧化錫具有獨特之奈米形貌以及被非活性物質圍繞著，故此在充放電過程中，以至於能達到降低材料體積變化之壓力。

為了達到更佳效能以及減少不可逆現象，並以錫基為基礎的複合材料，故此設計一新穎之錫碳複合奈米材料作為電極材料。我們提出一簡單方式製備碳材包覆金屬錫之核殼一維奈米線材料。以二氧化錫作為前驅物，通入乙炔氣體及氫氣作為載流氣體之環境成長；其中短軸為 100-350 奈米長度；長軸為數十微米長度；碳層為 30-70 奈米厚度，並發現管壁中具有中空區域。根據實驗所觀察之結果，提出一氣固相反應的成長機制，藉其嘗試了解成長過程。電池測試方面，以碳錫材料作為電極（充放電速率為 100 mA g^{-1} ），經過 100 次循環充放電仍有 525 mA h g^{-1} ；甚至在快速充放電狀況(1000 mA g^{-1})，依然保有 486 mA h g^{-1} 。因本材料具有獨特之一維形貌與中空區域作為體積膨脹之緩衝區域，故其效能之表現優異。

Acknowledgements

在這個實驗室六年了~終於可以寫篇謝誌！每年看著大夥一個一個離去真是有點感傷，現在換我自己想到要離開這 Chiulab 真的也有些不捨。

碩博期間能順利完成這段學業，首先要感謝的就是指導教授裘性天老師以及李紫原老師，兩位老師總是能在學生困惑時，適時地推一把，讓學生找到方向，不管是在學業或是生活上，都能給予適當建議與想法。在此還要感謝百忙之中抽空參加口試的陳登銘教授、李積琛教授、陳金銘博士，對於論文內容給予寶貴的建議，使得論文更加完整。

在 Chiulab 中，有個特色就是裘老師會跟大夥一起吃飯，這時裘老師就像是位老朋友般跟大家一起聊天打哈哈，與大家分享生活趣事，解解大家實驗之餘的苦悶，我想自己一定會懷念這一起吃飯的時刻。在 Chiulab 這個大家庭中，每個人互相扶持、互相幫忙，真的是謝謝各位的幫忙。感謝彭志偉學長、佳兒學姊、煌凱、亭凱、蕭蕭、weiwei、大銘、劉文志、柏欽、Kimi、心安、yoyo、鯊魚哥、亦諄、小童、鄒宗育、阿龍、明甥、千千、麥子、奕佑、彥伶、乃瑛、好靜、鮑魚、小臉、毓翔、凱歆、Sponge、顏詩芸、胡庭禎、楊晉嘉、麻立、李祖源、資竣和在職班的程壹、朝和、貴虹以及其他學弟妹。另外 LeeLab 的成員，雖然一周只有咪挺才相會，但大家也都是一起奮鬥的好夥伴，感謝旻橋、蕙仁、聰明哥、弘麒、久萱、婷婷、逸群、閔涵、淵為、Shalini、曉萍、景翔、猴子、庭輝、建甫、雅蓁、欣俞、緯祥、郁書、尹捷、貴麟、玠城、甘軒、世明和其他學弟妹。

最後要感謝我的家人，爸媽、兩位哥哥、大嫂，還有 Gigi。謝謝你們願意當作我的靠山，讓我能無憂無慮地完成這學業，願意等待我這讀書的時間，謝謝你們！感謝在這段日子上所有曾經幫助與指點過我的人。

Content

Abstract.....	I
摘要.....	III
Acknowledgements.....	
VI	
Content.....	VII
Content of Tables and Schemes	IX
List of Figures.....	X
Chapter 1 Introduction.....	1
1.1 Introduction.....	1
1.2 Battery systems.....	1
1.3 Lithium-ion batteries (LIBs).....	3
1.4 Electrode materials.....	5
1.5 Approaches for improving anode performance.....	7
1.6 Synthetic approaches to novel nanomaterials.....	8
1.7 Aim of the thesis.....	9
1.8 References.....	10
Chapter 2 Vapor Solid Reaction Growth of SnO₂ Nanorods as an Anode Material for Lithium-Ion Batteries	14
2.1 Introduction.....	14
2.2 Experimental.....	18
2.2.1 Growth of SnO ₂ nanorods.....	18
2.2.2 Materials characterizations	19
2.2.3 Electrochemical tests	19

2.3 Results and discussion	20
2.3.1 Characterization of SnO ₂ NRs	20
2.3.2 Proposed reaction pathway	25
2.3.3 Electrochemical properties of SnO ₂ NRs.....	28
2.4 Conclusions.....	38
2.5 References.....	39

Chapter 3 Template-Free Hydrothermal Syntheses of SnO₂ Structures for Anodes in Lithium-Ion Batteries..... 42

3.1 Introduction.....	42
3.2 Experimental.....	43
3.2.1 Growth of SnO ₂ structures.....	43
3.2.2 Materials characterizations.....	43
3.2.3 Electrochemical tests	44
3.3 Results and discussion	45
3.3.1 Characterization of SnO ₂ HSs.....	45
3.3.2 Characterization of SnO ₂ NSs.....	47
3.3.3 Electrochemical properties of SnO ₂	51
3.4 Conclusions.....	58
3.5 References.....	59

Chapter 4 One-Step Vapor–Solid Reaction Growth of Sn@C Core–Shell Nanowires as an Anode Material for Li-Ion Batteries..... 62

4.1 Introduction.....	62
4.2 Experimental.....	66
4.2.1 Growth of Sn@C core–shell NWs.....	66
4.2.2 Materials characterizations	66
4.2.3 Electrochemical tests	67

4.3 Results and discussion	67
4.3.1 Characterization of Sn@C core-shell NWs.....	68
4.3.2 Proposed reaction pathway	74
4.3.3 Electrochemical properties of Sn@C core-shell NWs.....	75
4.4 Conclusions.....	82
4.5 References.....	82
Chapter 5 Conclusions.....	87



Content of Tables and Schemes

Table 1.1 List of common commercial battery systems.....	2
Table 1.2 Comparison of the theoretical specific capacity, charge density, volume change and onset potential of various anode materials.....	7
Table 2.1 Summary of electrochemical properties of Sn containing electrodes for rechargeable Li-ion batteries.....	16
Table 2.2 Experimental conditions for samples prepared by reacting SnCl _{4(g)} and CaO _(s)	19
Table 2.3 Fitted impedance parameters obtained from EIS using the circuit in Figure 2.13b.....	38
Table 4.1 Summary of electrochemical properties of Sn containing electrodes for rechargeable Li-ion batteries.....	64
Table 4.2 Summary of Sn@C NW samples.....	66
Scheme 2.1 Proposed VSRG pathway to form SnO ₂ NRs and schematic diagram showing the role of the amorphous byproduct matrix during the lithiation and delithiation.	28
Scheme 4.1 Proposed VSRG pathway to form Sn@C core-shell NWs.	75
Scheme 5.1 Illustration of tin-based nanostructures as electrochemical test for LIBs.	88

List of Figures

Figure 1.1 Energy storage capability of common rechargeable battery systems.....	3
Figure 1.2 Components of a typical lithium-ion battery and the electrochemical processes in charging and discharging.....	4
Figure 1.3 Voltage vs. capacity for positive and negative electrode materials.....	5
Figure 1.4 Schematic the volume change of alloy materials during the cyclings.....	7
Figure 2.1 Low and high magnifications SEM images of A. (a) Sample with both NRs and particles, (b) enlarged view of the squared area in (a), (c and d) views of NRs, and (e and f) views of particles. (g) EDX and (h) XRD pattern.....	22
Figure 2.2 Low magnification SEM image in (a) shows the presence of a less observed morphology at the centre. (b) Enlarged view of the morphology.....	23
Figure 2.3 TEM studies of A. (a) Image of a section of a NR, (b) SAED pattern, and (c) HRTEM image from the circled area in (a), (d) a bundle of NRs, (e) high magnification image, and (f) SAED pattern from the squared area in (d).....	25
Figure 2.4 (a) Low and (b) high magnification SEM images and (c) EDX data from an area of sample B. (d) – (f) Corresponding data from another area of B.....	26
Figure 2.5 XRD patterns of samples B and C. Standard XRD patterns and the corresponding JCPDS file numbers are shown also.....	27
Figure 2.6 Low and high magnification SEM images of samples D and E. The EDX data are from the selected areas marked by red rectangles. Images and EDX of D are shown in (a) – (c). The data suggest that D is composed of SnO ₂ . Images and EDX of E are shown in (d) – (h). There two types of solids. The NRs shown in (d) and (e) are SnO ₂ , indicated by the EDX result in (f). According to the EDX in (h), the particles in (g) are CaSnO ₃ . The assignments are consistent with the XRD results shown in Figure	

2.7.....	27
Figure 2.7 XRD patterns of samples A, D and E. Standard XRD patterns and the corresponding JCPDS file numbers are shown also.	28
Figure 2.8 (a) CV of a SnO ₂ NR electrode scanned at 0.5 mV s ⁻¹ . (b) Specific capacity and columbic efficiency of a SnO ₂ NR electrode cycled at 100 mA g ⁻¹ . (c) Discharge capacity of a SnO ₂ NR electrode as a function of discharge rate (100–3000 mA g ⁻¹). All experiments were cycled between 0.005 V and 2.0 V vs. Li/Li ⁺	31
Figure 2.9 (a) Discharge capacities of electrodes fabricated from commercial SnO ₂ powders (sizes: 1 - 10 μm and 100 nm) at a cycling rate 100 mA g ⁻¹ . (b) Electrochemical performance of a SnO ₂ NR electrode cycled between 0.005 V and 2.0 V vs. Li/Li ⁺ after first ten cycles were cycled at 100 mA g ⁻¹ . 100 mA g ⁻¹ (□), 500 mA g ⁻¹ (○), 1000 mA g ⁻¹ (△), and 3000 mA g ⁻¹ (◇).	32
Figure 2.10 SEM images of (a) an electrode after one hundred cycles of lithiation and de-lithiation (without being washed) and (b) the original SnO ₂ NR electrode. The electrode was fabricated from a mixture of SnO ₂ NRs, carbon black, and binder.	34
Figure 2.11 (a) EDX of a SnO ₂ NR electrode after 100 cycles of lithiation and de-lithiation. The upper result was obtained from the whole-scan of the area shown in Figure 2.10a. The Cl content was low. The Pt signal was from the sputtered Pt metal, used to enhance the sample conductivity. The lower result was from the centre–point of one NR. (b) XRD patterns of sample A before and after 100 cycles of lithiation and de-lithiation. Related XRD patterns and the corresponding JCPDS file numbers are shown also.	35
Figure 2.12 SEM image of an electrode fabricated from a mixture of commercial SnO ₂ powder, carbon black, and binder after 50 cycles of lithiation and de-lithiation.....	36
Figure 2.13 (a) Nyquist plots from coin cells composed of as-fabricated NR and commercial powder of SnO ₂ . (b) Equivalent circuit for experimental data fitting. <i>Re:</i>	

electrolyte resistance; $R_{(sf+ct)}$: surface film and charge transfer resistance; R_p : polarization resistance; CPE: constant phase elements; W : Warburg impedance; C : intercalation capacitance.37

Figure 3.1 (a-c) Low and high magnifications SEM images and (d) XRD pattern of the HSs. Standard XRD pattern and the corresponding JCPDS file number are shown also.45

Figure 3.2 Results of TEM studies. (a) Image of a broken of HS. (b) SAED pattern and (c) HRTEM image from the squared area in (a). (d) EDX.46

Figure 3.3 (a-c) Low and high magnifications SEM images and (d) XRD pattern of SnO₂ NSs. Standard XRD patterns and the corresponding JCPDS file numbers are shown also.48

Figure 3.4 Results of TEM studies. (a) Image of a section of a sheet. (b) SAED pattern and (c) HRTEM image from the squared area in (a). (d) EDX.49

Figure 3.5 BET surface area profiles of (a) HSs and (b) NSs of SnO₂.50

Figure 3.6 Electrochemical studies of (a, c, e) HSs and (b, d, f) NSs of SnO₂. (a, b) CVs of SnO₂ electrodes scanned at 0.5 mV s⁻¹. (c, d) Specific capacity and columbic efficiency of SnO₂ electrodes cycled at 100 mA g⁻¹. (e, f) Discharge capacities of SnO₂ electrodes at various discharge rates 100-3000 mA g⁻¹. All experiments were cycled at 0.005-2.0 V vs. Li/Li⁺.53

Figure 3.7 Electrochemical studies of (a) HSs and (b) NSs of SnO₂. Electrochemical performances of SnO₂ electrodes cycled at 0.005-2.0 V vs. Li/Li⁺. The first ten cycles were cycled at 100 mA g⁻¹. □: 100 mA g⁻¹, ○: 500 mA g⁻¹, △: 1000 mA g⁻¹, and ◇: 3000 mA g⁻¹.54

Figure 3.8 SEM images of (a) the original SnO₂ HS electrode and (b, c) the electrode after one hundred cycles of lithiation and de-lithiation (without being washed). (d) EDX of the SnO₂ HS electrode after 100 cycles of lithiation and de-lithiation. The Pt signal

was from the sputtered Pt metal, used to enhance the sample conductivity. The electrode was fabricated from a mixture of SnO₂, carbon black, and binder.55

Figure 3.9 XRD patterns of the SnO₂ HS electrode before and after 100 cycles of lithiation and de-lithiation. Related XRD patterns and the corresponding JCPDS file numbers are shown also.56

Figure 3.10 SEM images of (a) the original SnO₂ NS electrode and (b, c) the electrode after one hundred cycles of lithiation and de-lithiation (without being washed). (d) EDX of the SnO₂ NS electrode after 100 cycles of lithiation and de-lithiation. The Pt signal was from the sputtered Pt metal, used to enhance the sample conductivity. The electrode was fabricated from a mixture of SnO₂, carbon black, and binder.56

Figure 3.11 XRD patterns of the SnO₂ NS electrode before and after 100 cycles of lithiation and de-lithiation. Related XRD patterns and the corresponding JCPDS file numbers are shown also.57

Figure 3.12 Nyquist plots from coin cells composed of as-fabricated HSs and NSs of SnO₂.58

Figure 3.13 Equivalent circuit for experimental data fitting. R_e: electrolyte resistance; R_(sf+ct): surface film and charge transfer resistance; R_p: polarization resistance; CPE: constant phase elements; W: Warburg impedance; C: intercalation capacitance.58

Figure 4.1 SEM images. (a) Low and (b) high magnification views of product A. (c) Low and (d) high magnification views of product B. The core-shell structures can be observed in the regions marked in the insets.69

Figure 4.2 SEM image and energy dispersive X-ray spectrum (EDX) of product A. 69

Figure 4.3 XRD patterns of products A and B.70

Figure 4.4 Raman spectra of product A and SnO₂. (Excitation wavelength: 785 nm, power: 5 mW)70

Figure 4.5 Thermogravimetric analysis (TGA) profile of A. The Sn and C contents are

estimated to be 46.8 wt % (8.1 at %) and 53.2 wt % (91.9 at %), respectively. The analysis was taken in O₂ using a heating rate of 10 K min⁻¹..... 71

Figure 4.6 SEM images of samples prepared at (a) 873 K for 60 min, (b) 923 K for 30 min, (c) 973 K for 30 min, (d) 1073 K for 30 min, and (e) 1123 K for 30 min. C₂H₂ was flowing at 3 sccm under atmospheric pressure. 71

Figure 4.7 TEM studies of product A. (a) A completely filled core–shell NW, (b) a pair of partially filled NWs, (c) a section of a broken NW, (d) a high magnification image from the pointed region in (c), (e) SAED pattern from the rectangle area in (c) and (f) SAED pattern from the end of the core in (d). (g) HRTEM image from the region circled in (d). (h) EDX spectrum from (c). 73

Figure 4.8 TEM images of a Sn@C core–shell NW. (a) Low magnification image and (b) high magnification view of the area marked by the arrow in (a) images taken after irradiating the circled area in (b) by an electron beam for (c) 60 s and (d) 180 s. The void shown in the circled area in (b) was filled by melted Sn after the electron beam irradiation. 73

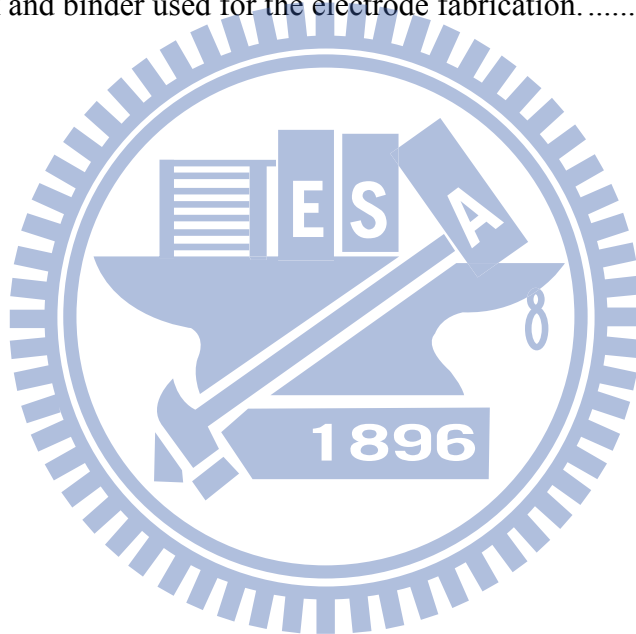
Figure 4.9 (a) Cyclic voltammograms of a Sn@C core–shell NW electrode (scan speed 0.5 mV s⁻¹). Electrochemical performance of the electrode cycled between 0.005 V and 2.0 V vs. Li/Li⁺ (cycling rate 500 mA g⁻¹); (b) voltage profiles of the electrode after 1, 2, 10, 25, 50, and 100 cycles and (c) capacity fading of the electrode. Coulombic efficiency and reversibility of each cycle of the electrode are presented in the secondary y-axis on the right of (c). The discharge capacity of an electrode fabricated from commercial Sn powder was cycled at 100 mA g⁻¹. 78

Figure 4.10 Electrochemical performance of a Sn@C core–shell NW electrode cycled between 0.005 V and 2.0 V vs. Li/Li⁺. (a) Curves of specific capacity versus cycle number of the electrode at cycling rates of 100 mA g⁻¹, 500 mA g⁻¹, 1000 mA g⁻¹ and 3000mA g⁻¹. (b) Discharge capacities of the electrode as a function of discharge rates

(100–3000 mA g⁻¹).....79

Figure 4.11 SEM images of the electrode prepared from Sn@C core-shell NWs. (a) Low and (b) high magnification views. (c) Low and (d) high magnification views of the electrode after 100 cycles of lithiation and delithiation. The electrode was fabricated with a mixture of carbon black and binder.....80

Figure 4.12 SEM images of (a) the commercial Sn powder, (b) the electrode prepared from the powder, and (c) low and (d) high magnification views of the electrode after 50 cycles of lithiation and delithiation. The Sn particles shown in (b) and (c) were mixed with carbon black and binder used for the electrode fabrication.81



Chapter 1 Introduction

1.1 Introduction

Energy consumption or production that rely on the combustion of fossil fuels is forecast to have a severe future impact on world economics and ecology. Electrochemical energy production is under serious consideration as an alternative energy and power source, as long as this energy consumption is designed to be more sustainable and more environmentally friendly.^{1,2} It is now almost universally recognized that gaseous emissions from the burning of fossil fuels and biomass are not only polluting the air of large, modern cities but are also creating a global warming with alarming consequences.³⁻⁶ The battery provides the portability of stored chemical energy with the ability to deliver this energy as electrical energy with a high conversion efficiency and no gaseous exhaust. Moreover, the alternative energy sources are preferably converted to D.C. electrical energy well-matched to storage as chemical energy in a battery. Therefore, of particular interest is a low-cost, safe, rechargeable battery of high voltage, capacity, and rate capability.^{7,8} The higher stored volume and gravimetric energy density of a Li battery has enabled realization of the mobile phone and tablet computer. However, the cost, safety, stored energy density, current rates, and service life are issues that continue to plague the development of the Li battery for the potential mass market of electric vehicles to alleviate distributed CO₂ emissions and noise pollution.

1.2 Battery systems

A list of common commercial systems is found in Table 1.1. A battery is one or more electrically connected electrochemical cells having terminals or contacts to supply electrical energy.⁹⁻¹² A primary battery is a cell, or group of cells, for the generation of

electrical energy intended to be used until exhausted and then discarded. Primary batteries are assembled in the charged state; discharge is the primary process during operation.¹³⁻¹⁹ A secondary battery is a cell or group of cells for the generation of electrical energy in which the cell, after being discharged, may be restored to its original charged condition by an electric current flowing in the direction opposite to the flow of current when the cell was discharged.²⁰⁻²⁶ Other terms for this type of battery are rechargeable battery or accumulator. As secondary batteries are usually assembled in the discharged state, they have to be charged first before they can undergo discharge in a secondary process.^{27,28}

Table 1.1 List of common commercial battery systems

common name	nominal voltage	anode	cathode	electrolyte
primary				
Leclanché (carbon–zinc)	1.5	zinc foil	MnO ₂ (natural)	aq ZnCl ₂ –NH ₄ Cl
zinc chloride (carbon–zinc)	1.5	zinc foil	electrolytic MnO ₂	aq ZnCl ₂
alkaline	1.5	zinc powder	electrolytic MnO ₂	aq KOH
zinc–air	1.2	zinc powder	carbon (air)	aq KOH
silver–zinc	1.6	zinc powder	Ag ₂ O	aq KOH
lithium–manganese dioxide	3.0	lithium foil	treated MnO ₂	LiCF ₃ SO ₃ or LiClO ₄ ^a
lithium–carbon monofluoride	3.0	lithium foil	CFx	LiCF ₃ SO ₃ or LiClO ₄ ^a
lithium–iron sulfide	1.6	lithium foil	FeS ₂	LiCF ₃ SO ₃ and/or LiClO ₄ ^a
rechargeable				
lead acid	2.0	lead	PbO ₂	aq H ₂ SO ₄
nickel–cadmium	1.2	cadmium	NiOOH	aq KOH
nickel–metal hydride	1.2	MH	NiOOH	aq KOH
lithium ion	4.0	Li(C)	LiCoO ₂	LiPF ₆ in nonaqueous solvents ^a
specialty				
nickel–hydrogen	1.2	H ₂ (Pt)	NiOOH	aq KOH
lithium–iodine	2.7	Li	I ₂	LiI
lithium–silver–vanadium oxide	3.2	Li	Ag ₂ V ₄ O ₁₁	LiAsF ₆ ^a
lithium–sulfur dioxide	2.8	Li	SO ₂ (C)	SO ₂ –LiBr
lithium–thionyl chloride	3.6	Li	SOCl ₂ (C)	SOCl ₂ –LiAlCl ₄
lithium–iron sulfide (thermal)	1.6	Li	FeS ₂	LiCl–LiBr–LiF
magnesium–silver chloride	1.6	Mg	AgCl	seawater

^a In nonaqueous solvents. Exact composition depends on the manufacturer, usually propylene carbonate–dimethyl ether for primary lithium batteries and ethylene carbonate with linear organic carbonates such as dimethyl carbonate, diethyl carbonate, and ethylmethyl carbonate for lithium ion cells.

The advancement in battery technology has been relying on the development and use of different types of materials for electrodes and electrolytes and thus with different electrochemical reactions. Figures 1.1 compares different types of batteries; lithium-ion batteries (LIBs) offer a balanced combination of high power and energy density, long cyclic life, and stability.^{12,29} The commercialization of lithium ion batteries has witnessed the soaring market share in the energy industry, especially in powering small electronic devices such as notebooks and cell phones.³⁰

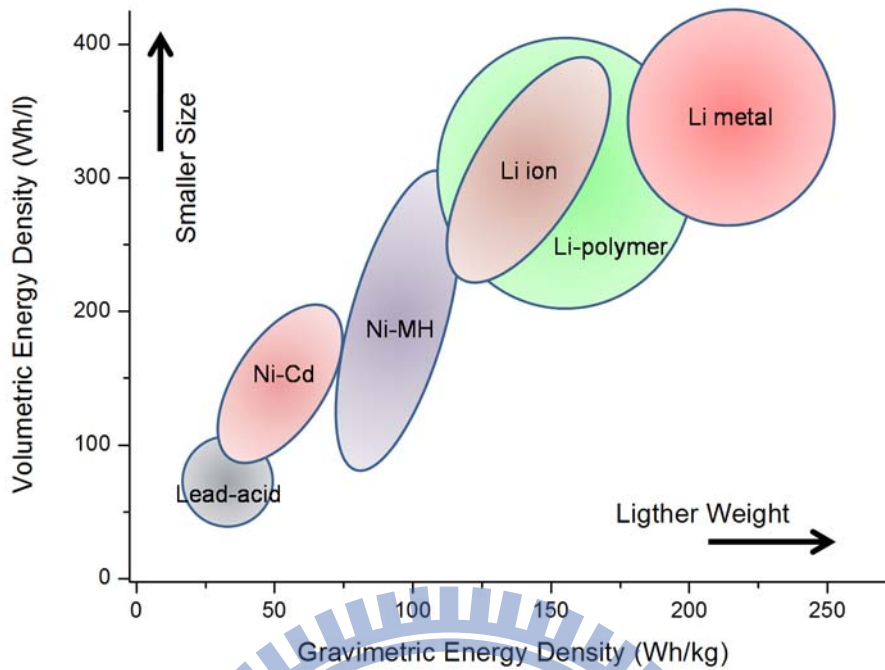


Figure 1.1 Energy storage capability of common rechargeable battery systems.

1.3 Lithium-ion batteries (LIBs)

Lithium-ion batteries (LIBs) are considered the most promising energy storage technologies for mobile electronics, electric vehicles and renewable energy systems operating on intermittent energy sources such as wind and solar.^{31,32} The anode is the negative electrode of a cell associated with oxidative chemical reactions that release electrons into the external circuit. The cathode is the positive electrode of a cell associated with reductive chemical reactions that gain electrons from the external circuit. Active mass is the material that generates electrical current by means of a chemical reaction within the battery. An electrolyte is a material that provides pure ionic conductivity between the positive and negative electrodes of a cell. A separator is a physical barrier between the positive and negative electrodes incorporated into most cell designs to prevent electrical shorting. The separator can be a gelled electrolyte or a microporous plastic film or other porous inert material filled with electrolyte. Separators must be permeable to the ions and inert in the battery environment. Usually

LIBs are connected in series or in parallel to deliver the user specified electrical characteristics. The active cathode and anode materials in a typical LIB are LiMO_2 (M: Fe, Co, Ni, Mn, etc.) and graphite respectively as shown in Figures 1.2; electrically insulated by a porous polypropylene membrane separator and an intervening electrolyte of LiClO_4 or LiPF_6 in a mixture of organic solvents (*e.g.* ethylene carbonate and dimethyl carbonate). During discharging, the electrochemical potential difference between the anode and cathode drives the Li^+ ions to move from anode to cathode internally through the electrolyte. The reverse process occurs during charging. The reversibility of the charge and discharge reactions at the electrodes determines the reversibility of the battery.^{33,34}

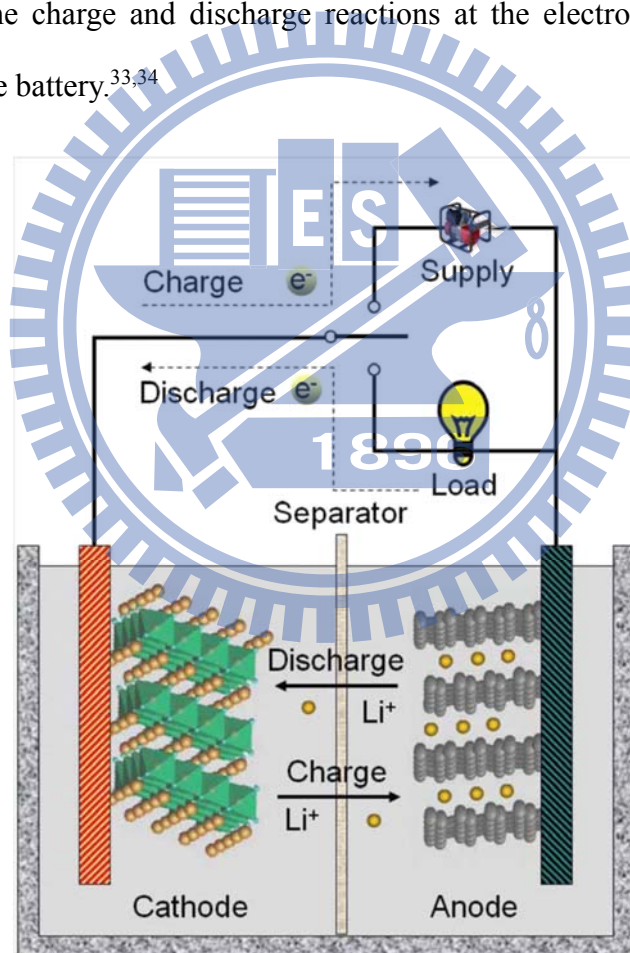


Figure 1.2 Components of a typical lithium-ion battery and the electrochemical processes in charging and discharging.

The three most important performance indicators for a LIB are capacity, cyclability and rate capability, which are strongly dependent on the properties of the

active electrode materials. For emerging applications, however, fundamental improvements are needed with regard to power, safety, cycle life, and cost.

1.4 Electrode materials

Summarizes the electrochemical potential and the typical lithium ion storage capacities of both anodic and cathodic materials as shown in Figure 1.3.^{33,35}

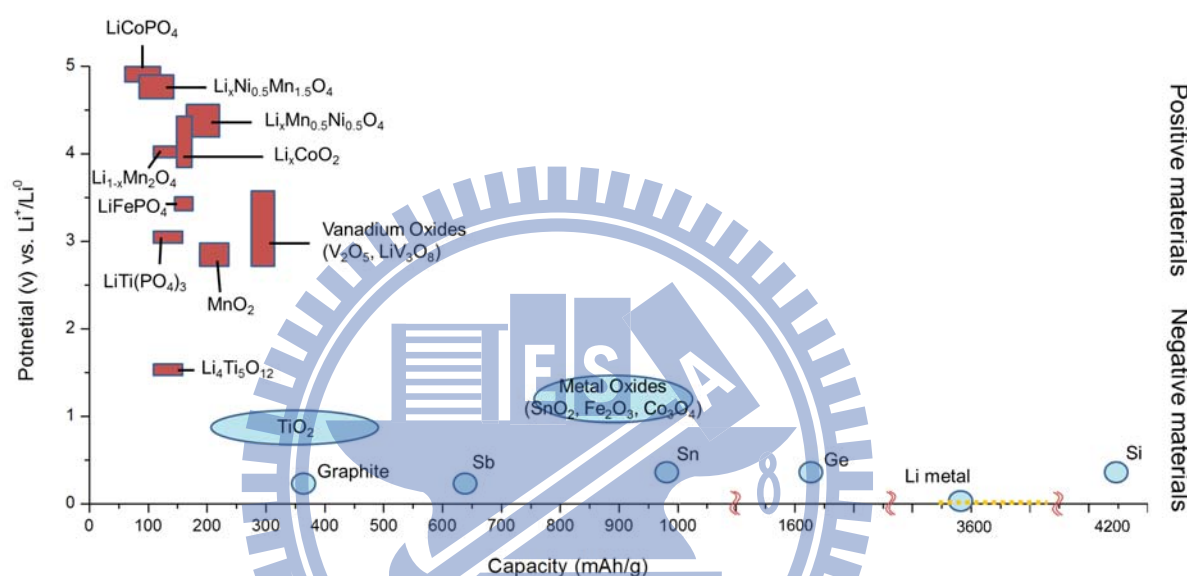


Figure 1.3 Voltage vs. capacity for positive and negative electrode materials.

Metal oxides have been explored for a number of years as lithium-ion battery anodes. The types of materials studied fall into three main categories: insertion compounds, notably Li₄Ti₅O₁₂, compounds that act as a source of an active main group metal, e.g. Sn-based materials, and compounds that act as a precursor to form a composite of Li₂O and a catalytic transition metal.³⁶⁻⁴¹ Each type of material has distinct advantages and disadvantages. For the insertion compound Li₄Ti₅O₁₂, high cycling stability is due in part to a negligible crystallographic volume contraction and expansion on lithium insertion and extraction, a flat voltage response at approximately 1.5 V (vs. Li/Li⁺), and excellent Li diffusivity.³⁶ Other related lithium titanates, such as Li₂MTi₆O₁₄ (M = Sr, Ba), have similar operating voltages and capacities but usually

display sloping discharge profiles due in part to the variety of crystallographic sites that are filled during single-phase reaction processes.³⁷ In contrast, certain main group metal oxides can react with lithium to form a matrix of Li₂O and an electrochemically active main group metal.^{38,39} These composite electrodes tend to offer a high initial capacity below 1 V; however, the reaction that forms the active matrix results in a high irreversible capacity and capacity fade on cycling remains an issue. More literatures have evaluated several transition metal oxides, e.g., CoO, in lithium cells.⁴¹ As with the main group metal oxides above, these materials work by metal displacement reactions to form lithia and, in this case, a transition metal. On charging to 3.0 V, however, the lithia is formally reduced due to the catalytic activity of the nanoscale transition metal in the electrode matrix, reducing the lithium cations at the counter electrode and reforming the metal oxide. This type of anode affords a stable, high capacity lithium-ion anode but the 3V voltage window required for reversibility may be too high for a commercially battery.³⁸⁻⁴¹ Research into low price and high efficiency energy storage materials have been recently intensified, and among various candidates, tin-based materials have been intensively investigated due to their versatile and easy modification of nanostructures.

Alloy anodes are known for their high specific capacity characteristics.^{34,42,43} The electrochemical properties of Sn-based alloy anodes, lithium metal and graphite are summarize in Table 1.2.³⁴ The theoretical specific capacities of alloy anodes are 2 times higher than that of graphite. Note that the charge densities (volumetric capacities) were calculated using the density of pristine metal. Even if the full volume expansion of lithiated products is considered, the charge densities of alloy anodes are still 8 times higher than those of graphite. The second merit of alloy anodes is their moderate operation potential vs. lithium. For example, Sn anodes have an onset voltage potential of 0.6 V above Li/Li⁺. This moderate potential averts the safety concern of lithium

deposition as with graphite anodes (~ 0.05 V vs. Li/Li⁺).

The main challenge for the implementation of alloy anodes is their large volume change (up to 300%) during lithium insertion and extraction, which often leads to pulverization of the active alloy particles and poor cycle stability as shown in Figure 1.4. In addition, the first-cycle irreversible capacity loss of alloy anodes is too high for practical application.⁴⁴⁻⁴⁶

Table 1.2 Comparison of the theoretical specific capacity, charge density, volume change and onset potential of various anode materials.

Lithiated phase	Specific capacity (mA h g ⁻¹)	Volumetric capacity (mA h cm ⁻³)	Potential vs. Li (V)	Volume change (%)
Li	3862	2047	0	-
Li _{4.4} Sn	994	7426	0.6	260
LiC ₆	372	834	0.05	12

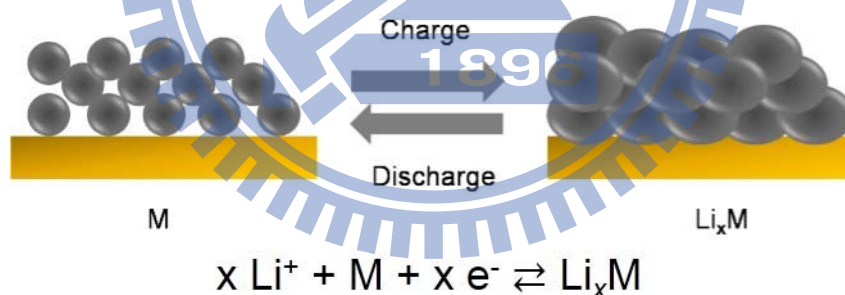


Figure 1.4 Schematic the volume change of alloy materials during the cyclings.

1.5 Approaches for improving anode performance

In an attempt to reduce the cyclic capacity fade and the first cycle irreversible capacity of alloy anodes, several strategies have been developed to reduce the detrimental effects of large volume changes and to alleviate the side reaction with electrolyte.

It has been confirmed in many studies that reducing the active particle size to the nanometer range and using the specific morphology of active materials can significantly improve the cycling performance of alloy anodes, especially when agglomeration of the particles is inhibited by a composite matrix.⁴⁷⁻⁵⁰

In addition, the purpose of dispersing active alloy particles within a composite matrix is to use the host matrix to buffer the large volume change of the active particles so that the electrode integrity and the electronic contact between the active particles and conductive phase can be maintained. To this end, the host matrix must allow rapid transport of electrons and Li^+ and maintain the microstructural stability of the whole anode. The host matrix also acts as a spacer to reduce the aggregation of active particles during cycling. Based on the type of host phase, composite anodes can be described as inactive matrix, active matrix, carbon-matrix composite and porous structures. The improved cycling stability was attributed primarily to the ability of nanosized particles to accommodate large stress and strain without cracking.⁵¹⁻⁵³

1.6 Synthetic approaches to novel nanomaterials

A widely accepted definition of a nanostructure is a system in which at least one dimension is down to 100 nm, typically including layer-like, wire-like, and particle-like structures.⁵⁴⁻⁵⁷ Since the successful synthesis of nanomaterials in our laboratory, the investigation of nanostructures has attracted considerable attention. Here, propose two simple synthesis method: hydrothermal method and vapor-solid reaction growth.⁵⁸⁻⁶⁶

Hydrothermal method is an environmentally friendly procedure due to the fact that it takes place at lower temperatures and the costs for energy, instrumentation and precursors are lower. In the past, hydrothermal methods were intensively studied and were applied to obtain a wide range of nanomaterials: powders, thin films, nanorods, fibers, nanotubes, etc. Some of the recent examples are presented below: The

TiO₂ fibers were synthesized using titanium isopropoxide (TTIP) under hydrothermal conditions; V₂O₅ nanobelt array was obtained by hydrothermal route starting from V₂O₅·xH₂O nanobelt array as precursor; SnO₂/carbon composite with double-shelled hollow spherical structure were synthesized involves two main steps.⁵⁸⁻⁶¹

Vapor-solid reaction growth (VSRG) is different from the the chemical vapor deposition reactions. However, the similar means that approaches are carried out by introducing precursors for the material to be deposited into a reaction chamber. Our group developed a unique route of phase segregation assisted VSRGs to synthesize one-dimensional (1D) nanostructures, including as cable-like Cu nanowires (NWs), *a*-silica encapsulated Ag NWs, CaF₂@*a*-C core-shell NWs, SiC nanotubes (NTs), Si NWs, and graphite fibers.⁶²⁻⁶⁶ Solid products generated in a VSRG may interact with others differently. Thus, they do not dissolve each other. Instead, the phase segregation cause the products develop cooperatively into unique morphology. The observed morphology variations are analogous to the examples found in block copolymer systems.

1.7 Aim of the thesis

Many research results related to improving the performance and cycle life of high-capacity electrode materials. Tin-based materials has been demonstrated as a potential anode material for LIBs because of its high lithium-ion storage capacity. Its theoretical specific capacity (Li_{4.4}Sn, 992 mA h g⁻¹) is much higher than that of graphitic carbon (LiC₆, 372 mA h g⁻¹). And Specific morphology materials are promising candidates for lithium-ion battery electrodes due to their faster charge transport, better conducting pathways, and good strain relaxation.

In this thesis, we will demonstrate a facile fabrication of tin-based nanostructures, include SnO₂ nanorods (NRs), hollow spheres (HSs), nanosheets (NSs) and Sn@C core-shell nanowires (NWs) *via* two kinds of synthetic approaches: hydrothermal

method and a unique VSRGs. The preparation, characterization, and growth mechanism of the tin-based nanostructures will be discussed in detail. And then, as-fabricated tin-based nanostructures will be used as electrochemical test for LIBs. Electrochemical properties and performance of the tin-based nanostructures are demonstrated in this work.

1.8 References

1. M. Granovskii, I. Dincer and M. A. Rosen, *J. Power Sources*, 2007, **167**, 461.
2. D. P. Birnie Iii, *J. Power Sources*, 2009, **186**, 539.
3. M. Z. Jacobson, *J. Geophys. Res.*, 2002, **107**, 4410.
4. S. H. Chung and J. H. Seinfeld, *J. Geophys. Res.*, 2002, **107**, 4407.
5. M. Z. Jacobson, *J. Geophys. Res.*, 2004, **109**, D21201.
6. M. Z. Jacobson, *Energy Environ. Sci.*, 2009, **2**, 148.
7. R. J. Brodd, K. R. Bullock, R. A. Leising, R. L. Middaugh, J. R. Miller and E. Takeuchi, *J. Electrochem. Soc.*, 2004, **151**, K1.
8. M. S. Whittingham, *Chem. Rev.*, 2004, **104**, 4271.
9. J. Besenhard, J. Heydecke, E. Wudy, H. Fritz and W. Foag, *Solid State Ionics*, 1983, **8**, 61.
10. K. Murata, S. Izuchi and Y. Yoshihisa, *Electrochim. Acta*, 2000, **45**, 1501.
11. J.-S. Chung and H.-J. Sohn, *J. Power Sources*, 2002, **108**, 226.
12. M. Winter and R. J. Brodd, *Chem. Rev.*, 2004, **104**, 4245.
13. S. Zaromb, *J. Electrochem. Soc.*, 1962, **109**, 1125.
14. B. Ratnakumar, *J. Appl. Electrochem.*, 1988, **18**, 268.
15. P. Hany, R. Yazami and A. Hamwi, *J. Power Sources*, 1997, **68**, 708.
16. C. F. Holmes, *J. Power Sources*, 2001, **97**, 739.
17. Y. Shao-Horn, S. Osmialowski and Q. C. Horn, *J. Electrochem. Soc.*, 2002, **149**,

A1499.

18. H. Yang, Y. Wang, X. Ai and C. Cha, *Electrochem. Solid-State Lett.*, 2004, **7**, A212.
19. M. Freitas, V. Pegoretti and M. Pietre, *J. Power Sources*, 2007, **164**, 947.
20. T. Sakai, H. Miyamura, N. Kuriyama, A. Kato, K. Oguro and H. Ishikawa, *J. Electrochem. Soc.*, 1990, **137**, 795.
21. C. J. Rydh, *J. Power Sources*, 1999, **80**, 21.
22. N. Vassal, E. Salmon and J. F. Fauvarque, *J. Electrochem. Soc.*, 1999, **146**, 20.
23. S. Okada, S. Sawa, M. Egashira, J.-i. Yamaki, M. Tabuchi, H. Kageyama, T. Konishi and A. Yoshino, *J. Power Sources*, 2001, **97**, 430.
24. S. Seki, Y. Kobayashi, H. Miyashiro, Y. Ohno, A. Usami, Y. Mita, N. Kihira, M. Watanabe and N. Terada, *J. Phy. Chem. B*, 2006, **110**, 10228.
25. H. Kim, B. Han, J. Choo and J. Cho, *Angew. Chem.*, 2008, **120**, 10305.
26. X. Zhao and L. Ma, *Int. J. Hydrogen Energy*, 2009, **34**, 4788.
27. S. Licht and B. Wang, *Electrochem. Solid-State Lett.*, 2000, **3**, 209.
28. J.-W. Lee and B. N. Popov, *J. Power Sources*, 2006, **161**, 565.
29. Y. Nishi, *J. Power Sources*, 2001, **100**, 101.
30. S. F. J. Flipsen, *J. Power Sources*, 2006, **162**, 927.
31. P. G. Bruce, B. Scrosati and J.-M. Tarascon, *Angew. Chem. Int. Ed.*, 2008, **47**, 2930.
32. D. Deng, M. G. Kim, J. Y. Lee and J. Cho, *Energy Environ. Sci.*, 2009, **2**, 818.
33. D. Liu and G. Cao, *Energy Environ. Sci.*, 2010, **3**, 1218.
34. W.-J. Zhang, *J. Power Sources*, 2011, **196**, 13.
35. M. Armand and J.-M. Tarascon, *Nature*, 2008, **451**, 652.
36. E. Ferg, R. Gummow, A. De Kock and M. Thackeray, *J. Electrochem. Soc.*, 1994, **141**, L147.
37. I. Belharouak and K. Amine, *Electrochem. Commun.*, 2003, **5**, 435.
38. M. Mohamedi, S.-J. Lee, D. Takahashi, M. Nishizawa, T. Itoh and I. Uchida,

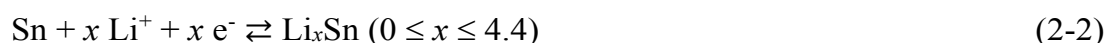
- Electrochim. Acta*, 2001, **46**, 1161.
39. P. Meduri, C. Pendyala, V. Kumar, G. U. Sumanasekera and M. K. Sunkara, *Nano Lett.*, 2009, **9**, 612.
40. F. Badway, I. Plitz, S. Grugeon, S. Laruelle, M. Dolle, A. Gozdz and J.-M. Tarascon, *Electrochem. Solid-State Lett.*, 2002, **5**, A115.
41. V. Pralong, J. B. Leriche, B. Beaudoin, E. Naudin, M. Morcrette and J. M. Tarascon, *Solid State Ionics*, 2004, **166**, 295.
42. D. Larcher, S. Beattie, M. Morcrette, K. Edstrom, J.-C. Jumas and J.-M. Tarascon, *J. Mater. Chem.*, 2007, **17**, 3759.
43. H. Kim, G. Jeong, Y.-U. Kim, J.-H. Kim, C.-M. Park and H.-J. Sohn, *Chem. Soc. Rev.*, 2013, **42**, 9011.
44. M. Winter and J. O. Besenhard, *Electrochim. Acta*, 1999, **45**, 31.
45. R. Benedek and M. M. Thackeray, *J. Power Sources*, 2002, **110**, 406.
46. U. Kasavajjula, C. Wang and A. J. Appleby, *J. Power Sources*, 2007, **163**, 1003.
47. L. Beaulieu, D. Larcher, R. Dunlap and J. Dahn, *J. Electrochem. Soc.*, 2000, **147**, 3206.
48. C. K. Chan, H. Peng, G. Liu, K. Mcllwath, X. F. Zhang, R. A. Huggins and Y. Cui, *Nat Nano*, 2008, **3**, 31.
49. N. Ding, J. Xu, Y. Yao, G. Wegner, I. Lieberwirth and C. Chen, *J. Power Sources*, 2009, **192**, 644.
50. H. Li, Z. Wang, L. Chen and X. Huang, *Adv. Mater.*, 2009, **21**, 4593.
51. J. Yang, M. Winter and J. O. Besenhard, *Solid State Ionics*, 1996, **90**, 281.
52. J. Yang, M. Wachtler, M. Winter and J. O. Besenhard, *Electrochem. Solid-State Lett.*, 1999, **2**, 161.
53. Q. Si, K. Hanai, N. Imanishi, M. Kubo, A. Hirano, Y. Takeda and O. Yamamoto, *J. Power Sources*, 2009, **189**, 761.

54. C. M. Lieber, *Solid State Commun.*, 1998, **107**, 607.
55. X. Zhou, L.-J. Wan and Y.-G. Guo, *Chem. Commun.*, 2013, **49**, 1838.
56. W. Tian, C. Zhang, T. Zhai, S.-L. Li, X. Wang, M. Liao, K. Tsukagoshi, D. Golberg and Y. Bando, *Chem. Commun.*, 2013, **49**, 3739.
57. S. I. Cha, K. H. Hwang, Y. H. Kim, M. J. Yun, S. H. Seo, Y. J. Shin, J. H. Moon and D. Y. Lee, *Nanoscale*, 2013, **5**, 753.
58. P.-C. Chen, M.-C. Tsai, H.-C. Chen, I. N. Lin, H.-S. Sheu, Y.-S. Lin, J.-G. Duh, H.-T. Chiu and C.-Y. Lee, *J. Mater. Chem.*, 2012, **22**, 5349.
59. P.-C. Chen, M.-C. Tsai, M.-H. Yang, T.-T. Chen, H.-C. Chen, I. C. Chang, Y.-C. Chang, Y.-L. Chen, I. N. Lin, H.-T. Chiu and C.-Y. Lee, *Appl. Catal. B: Environ.*, 2013, **142**, 752.
60. Y. Wang, H. J. Zhang, W. X. Lim, J. Y. Lin and C. C. Wong, *J. Mater. Chem.*, 2011, **21**, 2362.
61. X. W. Lou, D. Deng, J. Y. Lee and L. A. Archer, *Chem. Mater.*, 2008, **20**, 6562.
62. M. Y. Yen, C. W. Chiu, C. H. Hsia, F. R. Chen, J. J. Kai, C. Y. Lee and H. T. Chiu, *Adv. Mater.*, 2003, **15**, 235.
63. C.-H. Hsia, M.-Y. Yen, C.-C. Lin, H.-T. Chiu and C.-Y. Lee, *J. Am. Chem. Soc.*, 2003, **125**, 9940.
64. C.-H. Huang, Y.-H. Chang, C.-Y. Lee and H.-T. Chiu, *Langmuir*, 2005, **22**, 10.
65. C.-H. Wang, H.-K. Lin, T.-Y. Ke, T.-J. Palathinkal, N.-H. Tai, I. N. Lin, C.-Y. Lee and H.-T. Chiu, *Chem. Mater.*, 2007, **19**, 3956.
66. C.-H. Huang, Y.-H. Chang, H.-K. Lin, C.-W. Peng, W.-S. Chung, C.-Y. Lee and H.-T. Chiu, *J. Phys. Chem. C*, 2007, **111**, 4138.

Chapter 2 Vapor Solid Reaction Growth of SnO₂ Nanorods as an Anode Material for Lithium-Ion Batteries

2.1 Introduction

Li-ion batteries (LIBs) have been commonly used as a power source for portable electronic devices and are also considered as a candidate to power electric vehicles and hybrid electric vehicles.^{1,2} Nanoscale materials are expected to contribute significantly to realizing these important goals in LIB research because the device may achieve high capacity, power rate, and long cycle lifetime simultaneously.^{3,4} Graphite is the current choice of anode material for commercial LIBs. However, its theoretical capacity is low, 372 mA h g⁻¹.⁵ To achieve high energy density, novel materials are required to replace presently used graphite anodes. Many promising anode electrode materials, such as Si, TiO₂, and Sn-based materials,⁶⁻¹¹ have been explored in order to overcome the limitations. The high theoretical capacity of Sn-based materials are more than twice of that of the commercial graphite. The potential of Li⁺ ion intercalation of Sn-based materials is low. Among them, SnO₂ is regarded as one of the most promising candidates for anode application in LIBs.¹²⁻¹⁹ When SnO₂ is used as the active component in the LIBs, the electrochemical reactions are comprised of irreversible and reversible steps, (2-1) and (2-2), respectively:



However, these steps provide some drawbacks. Due to its irreversible nature, the first reaction is responsible for the severe capacity loss in the first few cycles. This is

the result of the formation of an inactive amorphous byproduct matrix. It probably contains Li_2O , formed from the reduction of SnO_2 by Li, the decomposed carbonate-based electrolyte, and the solid electrolyte interphase (SEI).²⁰ The second reaction is reversible, with Li^+ ions repeatedly stored and released during alloying and dealloying cycles. However, a drastic volume change, around 300% during the cyclings, is induced in this step.²¹ The so-called pulverization problem blocks the electrical contact pathways and leads to rapid deterioration of the electrode capacity. Unique SnO_2 structures prepared by different synthetic routes could overcome the problem.^{14–}
¹⁹ Literature example of electrodes composed of nanoparticles (NPs), one-dimensional (1D), two-dimensional (2D), and hollow nanostructures of SnO_2 showed improved electrochemical performances. These cases, with high surface-to-volume ratio and excellent surface activities, are summarized in Table 2.1.

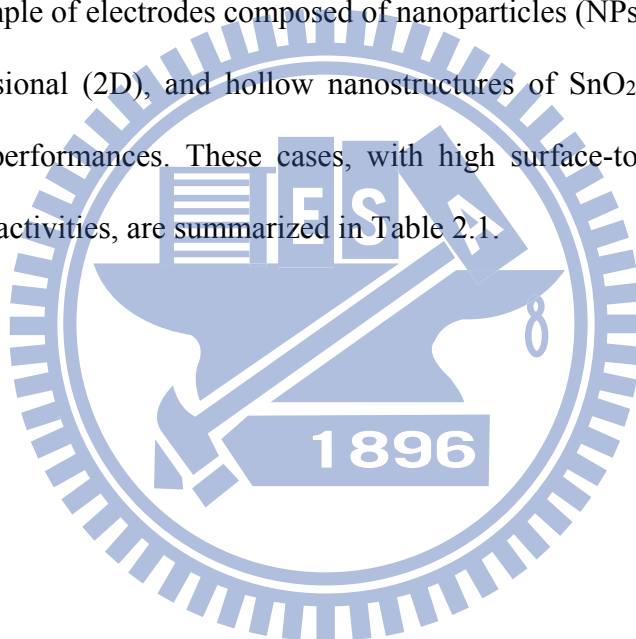
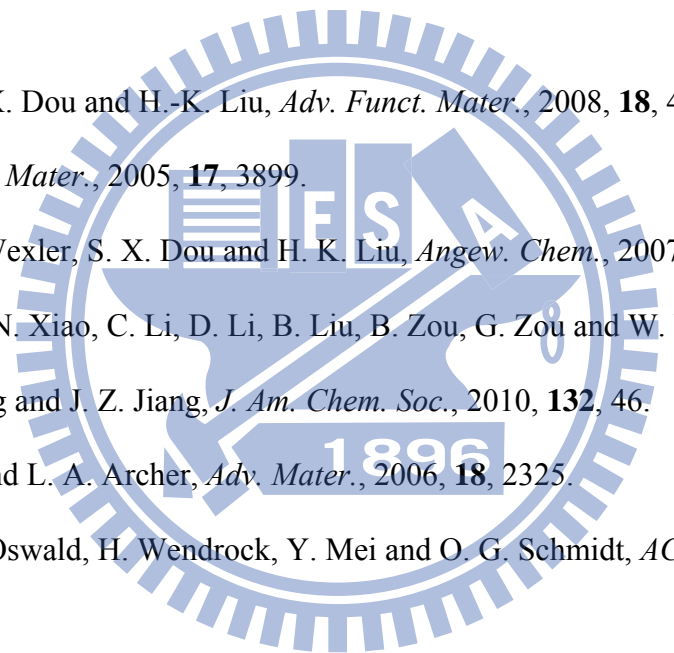


Table 2.1 Summary of electrochemical properties of Sn containing electrodes for rechargeable Li-ion batteries.

Electrode material	Experimental Method	Morphology and Composition	Electrochemical Performance			Ref
			Working Potential (V)	Cycling Rate	Capacity (mA h g ⁻¹)	
NTs SnO ₂ NWs NPs	Sol-gel vacuum-suction Thermal-evaporation sol-gel	D of NT: 200 nm D, L of NW: 200 nm, ~tens μm Size of NP < 100 nm	0.05 – 1.5	50 cycles at 100 mA g ⁻¹ (1 C = 790 mA g ⁻¹)	250 210 90	14 ^a
SnO ₂ NTs	Infiltration technique	Diameter: 180 – 230 nm	0.005 – 2	80 cycles at 0.05 mA·cm ⁻²	525	15 ^b
SnO ₂ NWs	Thermal evaporation	Diameter: 200 – 500 nm Length: 10 μm	0.005 – 2.5	50 cycles at 100 mA g ⁻¹ (1 C = 782 mA g ⁻¹)	460	16 ^c
SnO ₂ nanoflowers	Free cation-induced decomposition	Diameter: 50 – 110 nm	0.01 – 2	20 cycles at 0.1 C (1 C = 783 mA g ⁻¹)	450	17 ^d
SnO ₂ nanosheets	Hydrothermal method	Thin: 1.5 – 3 nm	0.005 – 3	20 cycles at 0.1 C (1 C = 782 mA g ⁻¹)	559	18 ^e
SnO ₂ hollow nanospheres	Hydrothermal method	Diameter: 50 – 200 nm Wall thickness: 10 nm	0.005 – 2	40 cycles at 0.2 C (1 C = 645 mA g ⁻¹)	450	19 ^f
SnO ₂ NRs	Vapor-Solid Reaction Growth (VSRG)	Diameter: 15 nm, Length: 1000 nm	0.005 – 2	100 cycles at 100 mA g ⁻¹ (1 C = 790 mA g ⁻¹)	435	This work

SnO ₂ /Cu nanosheets	Rolled-up nanotechnology	SnO ₂ film: 50 nm, Cu film: 3 nm	0.05 – 1.5	150 cycles at 100 mA g ⁻¹ (1 C = 782 mA g ⁻¹)	764	36 ^g
---------------------------------	--------------------------	--	------------	---	-----	-----------------

NT: nanotube, NW: nanowire, NP: nanoparticle.

- 
- a. M.-S. Park, Y.-M. Kang, G.-X. Wang, S.-X. Dou and H.-K. Liu, *Adv. Funct. Mater.*, 2008, **18**, 455.
- b. Y. Wang, J. Y. Lee and H. C. Zeng, *Chem. Mater.*, 2005, **17**, 3899.
- c. M. S. Park, G. X. Wang, Y. M. Kang, D. Wexler, S. X. Dou and H. K. Liu, *Angew. Chem.*, 2007, **119**, 764.
- d. J. Ning, Q. Dai, T. Jiang, K. Men, D. Liu, N. Xiao, C. Li, D. Li, B. Liu, B. Zou, G. Zou and W. W. Yu, *Langmuir*, 2009, **25**, 1818.
- e. C. Wang, Y. Zhou, M. Ge, X. Xu, Z. Zhang and J. Z. Jiang, *J. Am. Chem. Soc.*, 2010, **132**, 46.
- f. X. W. Lou, Y. Wang, C. Yuan, J. Y. Lee and L. A. Archer, *Adv. Mater.*, 2006, **18**, 2325.
- g. J. Deng, C. Yan, L. Yang, S. Baunack, S. Oswald, H. Wendrock, Y. Mei and O. G. Schmidt, *ACS Nano*, 2013, **7**, 6948.

In previous works, we have demonstrated the growths of 1D nanostructures, including as Sn@C core-shell nanowires (NWs), SiC nanotubes (NTs), Si NWs, and graphite fibers, by phase segregation assisted vapor-solid reaction growths (VSRGs).^{10,22,23} Solid products generated in a VSRG may interact with others differently. Thus, they do not dissolve each other. Instead, the phase segregation cause the products develop cooperatively into unique morphology. The observed morphology variations are analogous to the examples found in block copolymer systems.^{24,25} In these cases, due to chemical incompatibility, each one of the component blocks self-assembles into nanophases ordered and arranged discretely. In this study, we report a new reaction employing vapor phase SnCl₄ and CaO solid particles as the reactants. The products of the VSRG process are SnO₂ and CaCl₂ solids. After the removal of the CaCl₂ salt, SnO₂ nanorods (NRs) are isolated. Electrodes composed of the SnO₂ NRs are investigated for possible LIB electrode applications. Our observations are discussed below.

2.2 Experimental

2.2.1 Growth of SnO₂ nanorods

A typical reaction was carried out inside a hot-wall reactor composed of a Lindberg tubular furnace and a quartz tube (diameter 27 mm). Dehydration of Ca(OH)₂ (Sigma-Aldrich) uniformly placed in a quartz boat (length 10 cm) at the centre of the furnace at 1023 K for 1 h produced CaO. SnCl₄ (Acros Organics, 99%, anhydrous) was vaporized at room temperature and atmospheric pressure by a flowing stream of Ar (20 sccm) into the reactor and reacted with CaO at a designated temperature and time period. The products were cooled naturally to room temperature in Ar and collected. The products were washed with deionized (DI) water several times to remove the soluble portion. The insoluble portion was dried at 353 K overnight to offer a white product. A

summary of the experimental conditions and the obtained products are listed in Table 2.2.

Table 2.2 Experimental conditions for samples prepared by reacting $\text{SnCl}_{4(g)}$ and $\text{CaO}_{(s)}$.

Sample	Reaction Temperature (K)	Reaction Time (min)	Washed by $\text{H}_2\text{O}_{(l)}$	Observed Solid Phases in the Product
A	1023	360	Yes	$\text{SnO}_{2(s)}$
B	1023	360	No	$\text{SnO}_{2(s)}$, $\text{CaCl}_{2(s)}$
C	1023	60	No	$\text{SnO}_{2(s)}$, $\text{CaSnO}_{3(s)}$, $\text{CaCl}_{2(s)}$, $\text{CaO}_{(s)}$
D	1073	360	Yes	$\text{SnO}_{2(s)}$
E	973	360	Yes	$\text{SnO}_{2(s)}$, $\text{CaSnO}_{3(s)}$

$\text{SnCl}_{4(l)}$ was evaporated at room temperature by $\text{Ar}_{(g)}$ (10 sccm). Another flowing stream of $\text{Ar}_{(s)}$ (10 sccm) was also introduced into the reactor.

2.2.2 Materials characterizations

Samples were characterized by using a Bruker AXS D8 Advance X-ray diffractometer (XRD) with $\text{Cu K}_{\alpha 1}$ radiation. Scanning electron microscopic (SEM) images and energy dispersive X-ray (EDX) spectra were taken with a Hitachi S-4700I operated at 15 keV. Transmission electron microscopic (TEM), electron diffraction (ED), high-resolution TEM (HRTEM) images, and EDX data were acquired on a JEOL JEM-2010 at 200 kV.

2.2.3 Electrochemical tests

Typically, two-electrode 2032 coin-type cells were assembled using the materials described below in a dry room. An *N*-methyl pyrrolidone (NMP) (Timcal) slurry was prepared by mixing SnO_2 , carbon black (Super-P) (Timcal), and polyvinylidene fluoride (PVDF) with a weight ratio 80 : 10 : 10. A Cu foil (Furukawa) (thickness 14 μm),

vacuum dried at 403 K overnight, was compressed and cut into disks (diameter 14 mm). An electrolyte composed of LiClO₄ (Sigma-Aldrich) dissolved in a mixture of ethylenecarbonate (EC) (Alfa-Aesar) and dimethylcarbonate (DMC) (Alfa-Aesar) (1.0 M, volume ratio 1 : 1) was prepared also. A Li plate was cut into disks (diameter, 14 mm) and used as both the reference and the counter electrode. The amount of the composite was weighed and combined with the electrolyte and the electrodes into coin-type cells. Electrochemical measurements were performed with a battery test system (UBIQ technology, BAT-750B). Cyclic voltammetry (CV) and electrochemical impedance spectroscopy (EIS) experiments were carried out using a CHI 6081C (CH Instruments) electrochemical analyzer. Electrochemical experiments of the coin-type cells were cycled between 0.005 V and 2.0 V at room temperature. Some of the devices were disassembled after the tests. The composite solids after the cycling were investigated without being washed.

2.3 Results and discussion

In a horizontal hot-wall quartz tube reactor, Ca(OH)₂ powder was dehydrated. As shown by the XRD of the product, CaO was formed (JCPDS card file no. 44-1481 and 70-4068).²⁵ Then, the as-formed powder was reacted to a flowing mixture of SnCl₄ and Ar at 1023 K under atmospheric pressure. After the as-prepared product was washed with DI water to remove CaCl₂, the final product sample A, characterized to be SnO₂ NRs as described below, was obtained. Detailed experimental conditions and results are summarized in Table 2.2.

2.3.1 Characterization of SnO₂ NRs

SEM images of sample A are shown in Figure 2.1. Figure 2.1a displays the typical morphology found A. From a selected area in Figure 2.1a, numerous NRs

(diameter 10–20 nm, length 1–2 μm) on top of an aggregate of particles can be seen in the magnified view in Figure 2.1b. Figure 2.1c and 2.1d display the views on top of the NRs. Figure 2.1e and 2.1f present the low and high magnification views of representative aggregates of particles, respectively. From TEM studies (see below), the particles are characterized to be composed of bundles of NRs. An EDX of sample A shown in Figure 2.1g indicates that it contains both Sn and O. The XRD pattern in Figure 2.1h confirms that sample A is composed of SnO_2 (JCPDS card File no. 41-1445).²⁶ Another type of less observed morphology, shown in Figure 2.2, also presents bundles of branched NRs. The estimated amount of this morphology is *ca.* 5%.



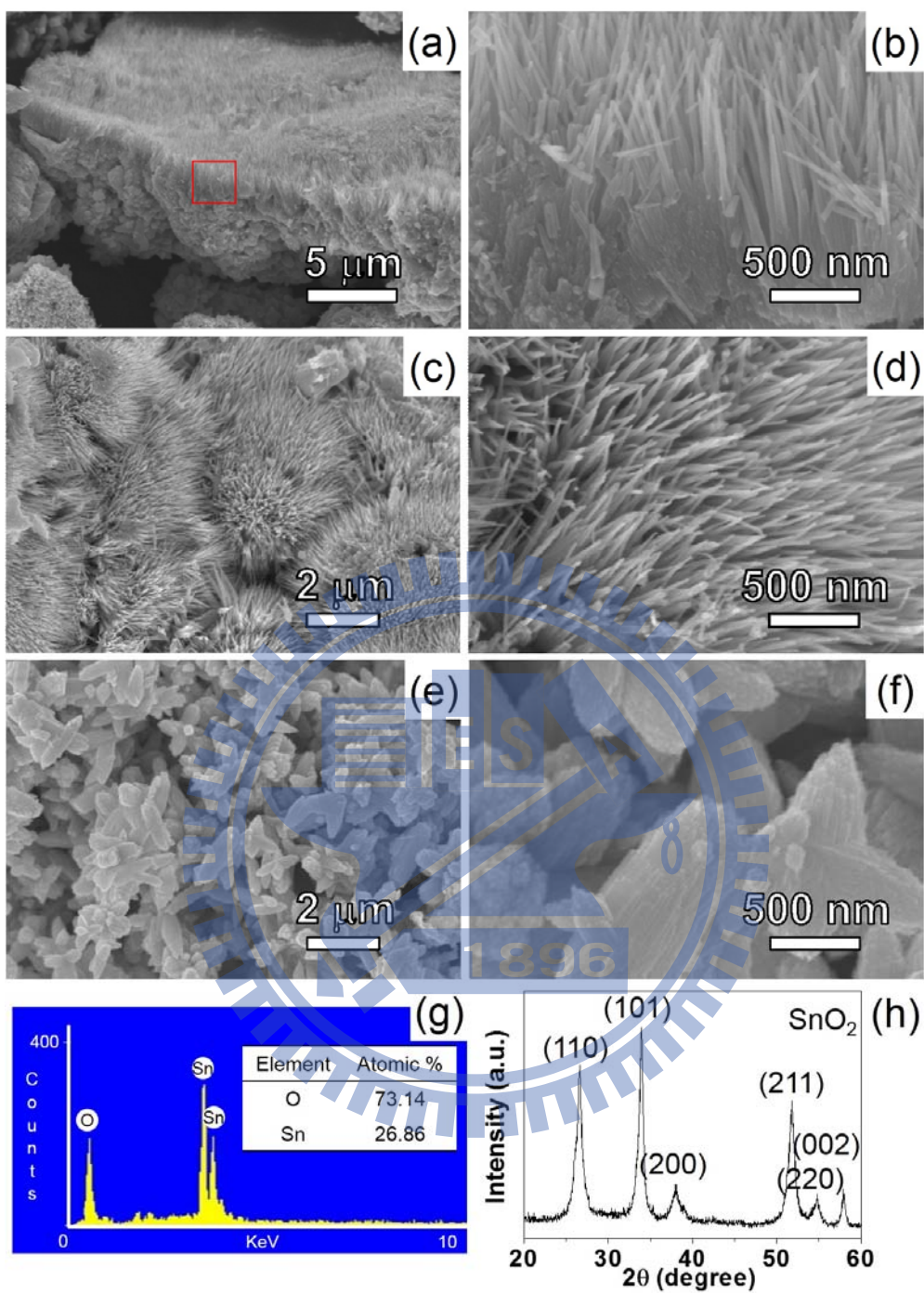


Figure 2.1 Low and high magnifications SEM images of A. (a) Sample with both NRs and particles, (b) enlarged view of the squared area in (a), (c and d) views of NRs, and (e and f) views of particles. (g) EDX and (h) XRD pattern.

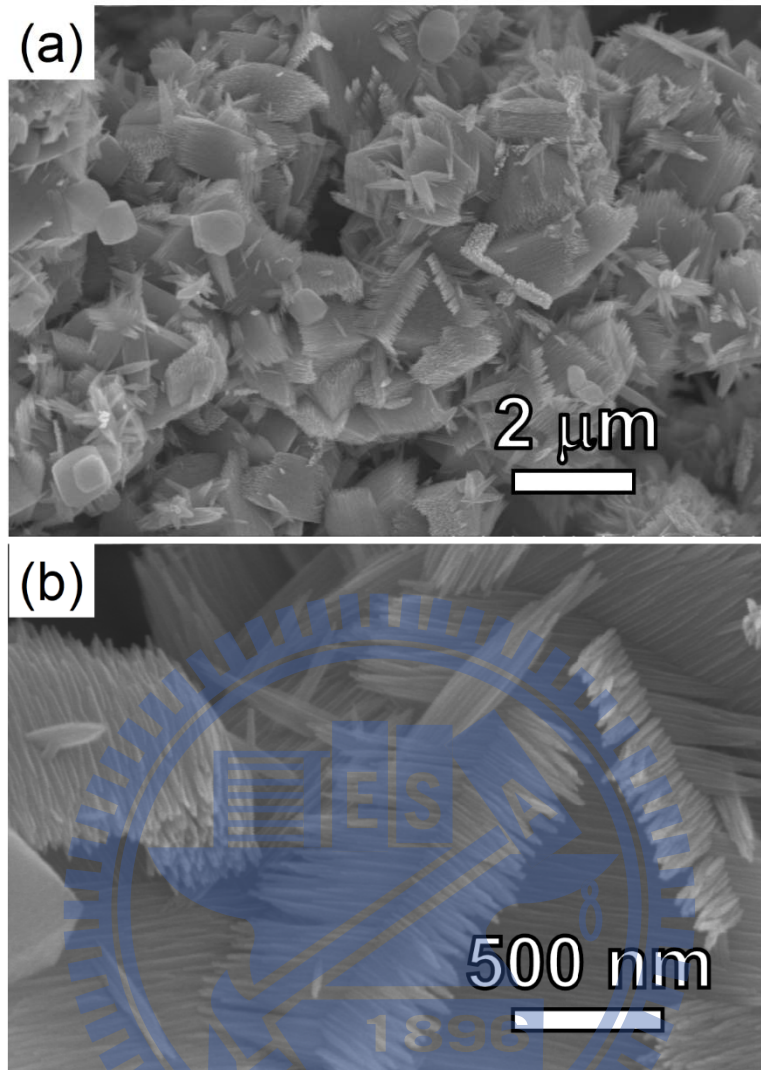
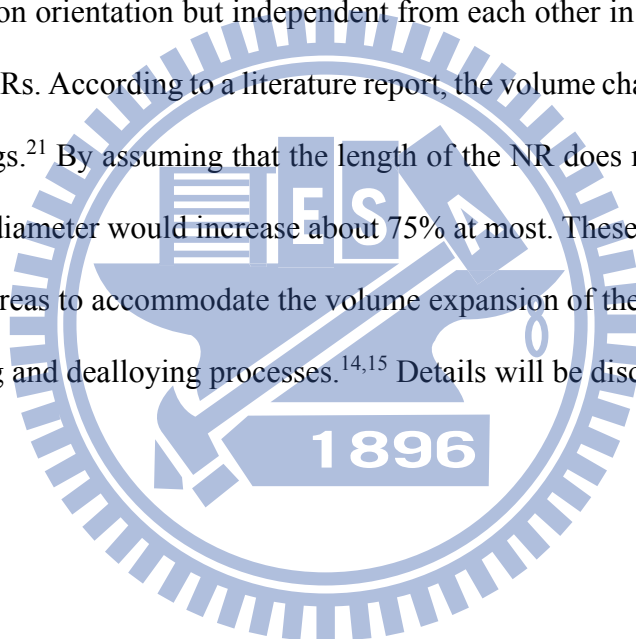


Figure 2.2 Low magnification SEM image in (a) shows the presence of a less observed morphology at the centre. (b) Enlarged view of the morphology.

TEM studies of sample A are shown in Figure 2.3. In Figure 2.3a, the image of a 1D material is presented. Its length, 150 nm, suggests that it is a fragment of a NR. It confirms that the NR structure with diameter 7–20 nm are observed shown. The SAED in Figure 2.3b shows a dot pattern. This indicates that the sample can be indexed to the $[0\ 1\ 0]$ zone axis of the single crystalline SnO_2 . From the image, the lattice parameters a and c of a tetragonal crystal system are estimated to be 0.47 nm and 0.31 nm, respectively.²⁶ Figure 2.3c shows a high resolution lattice image of the sample displayed in Figure 2.3a. The space between the parallel fringes from the crystalline structure was measured to be 0.24 nm and 0.27 nm. These are equal to the spacings of

the $\{2\ 0\ 0\}$ and $\{1\ 0\ 1\}$ planes of SnO_2 , respectively. Also, the image suggests that the diameter of the NR is 18 nm. Combined with the SAED result, the crystallization of the NR is determined to be along the $[0\ 0\ 2]$. Figure 2.3d displays the image of a particle found in sample A. The magnified view of a selected area shown in Figure 2.3d is presented in Figure 2.3e. From the image, it is clear that the particle is actually composed of bundles of numerous NRs with gaps among them. The SAED of the selected area displays a slightly diffused dot pattern which can be indexed to SnO_2 also.²⁶ This suggests that all NRs in the bundles are single crystalline, with the same crystallization orientation but independent from each other in space. Thus, voids exist among the NRs. According to a literature report, the volume change is about 300% during the cyclings.²¹ By assuming that the length of the NR does not increase during the cyclings, the diameter would increase about 75% at most. These gaps or voids may act as the buffer areas to accommodate the volume expansion of the electrode material during Li alloying and dealloying processes.^{14,15} Details will be discussed more below.



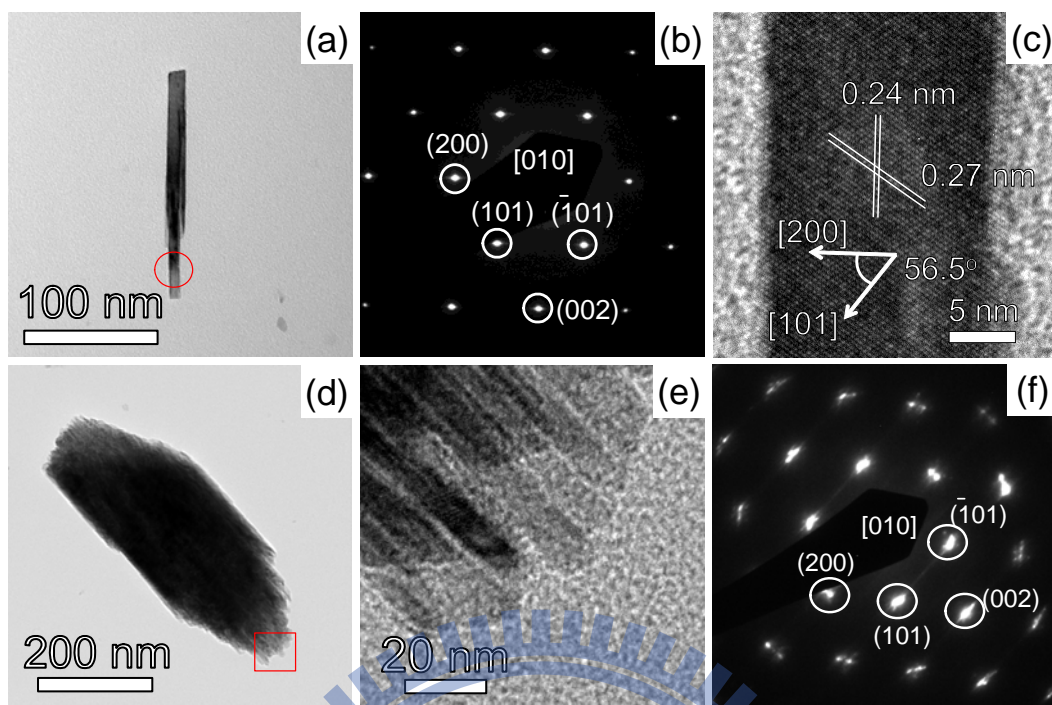
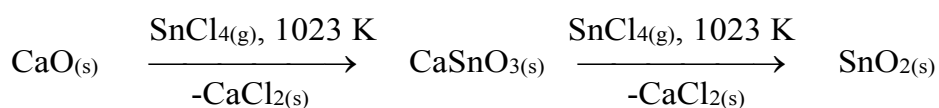


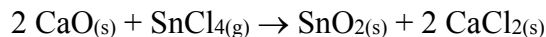
Figure 2.3 TEM studies of A. (a) Image of a section of a NR, (b) SAED pattern, and (c) HRTEM image from the circled area in (a), (d) a bundle of NRs, (e) high magnification image, and (f) SAED pattern from the squared area in (d).

2.3.2 Proposed reaction pathway

To understand more about the factors affecting the NRs growths, several samples prepared at different reaction conditions were investigated. Sample B was the as-synthesized product formed at 1023 K without DI water washing. The co-existence of SnO₂ and CaCl₂ was observed by SEM, EDX and XRD, as shown in Figure 2.4 and 2.5. SEM and XRD characterizations of samples C, D and E are displayed in Figure 2.5-2.7. In samples C and E, prepared by using a shorter reaction time or a lower temperature, respectively, than the condition employed to form sample A, the coexistence of SnO₂ and CaSnO₃ is found. We attribute CaSnO₃ as an observed intermediate and describe the overall reactions in the equation below.



The overall reaction stoichiometry is proposed to be:



$$\Delta G_r^\circ = -356.2 \text{ kJ/mol}$$

The reaction is thermodynamically favoured due to the negative standard Gibbs free energy of reaction ΔG_r° .²⁷ In addition, we suggest that SnO₂ NRs are grown *via* a VSRG pathway similar to the one proposed for the growths of nanosized graphite and Si crystals with various morphologies.²³ The overall phenomena resembled the morphology alterations caused by the phase segregation in block copolymer systems.^{24,25} In this study, the initial products were CaSnO₃ and CaCl₂. Further reactions between the SnCl₄ vapor and the CaSnO₃ solid would produce a molten mixture of SnO₂ and CaCl₂. The solubility of the high melting point SnO₂ (mp 1903 K) in the low melting ionic CaCl₂ (mp 1045 K) is expected to be extremely low. As the reaction prolongs, SnO₂ crystallizes into the NR shape in the molten CaCl₂. These are summarized in Scheme 2.1.

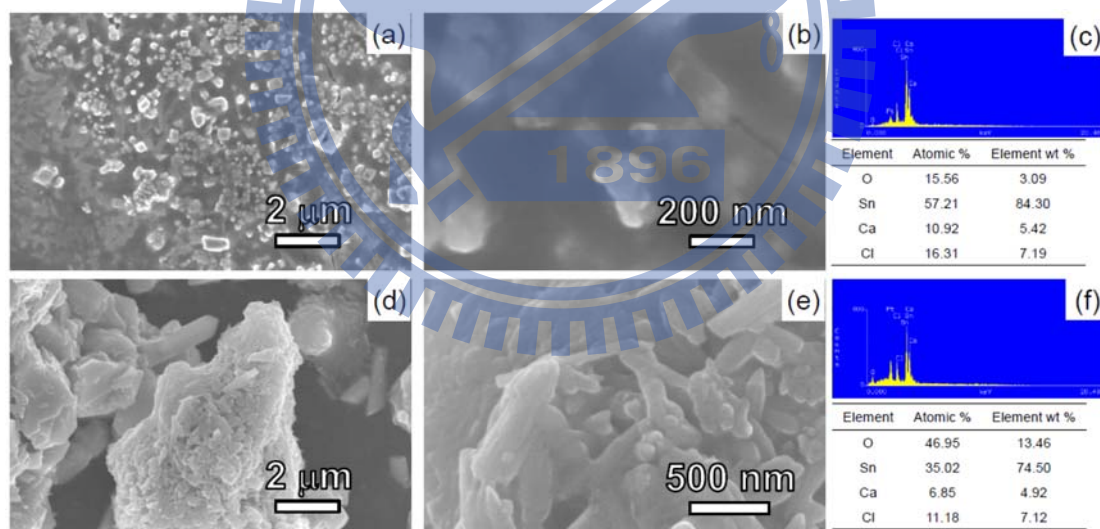


Figure 2.4 (a) Low and (b) high magnification SEM images and (c) EDX data from an area of sample B. (d) – (f) Corresponding data from another area of B.

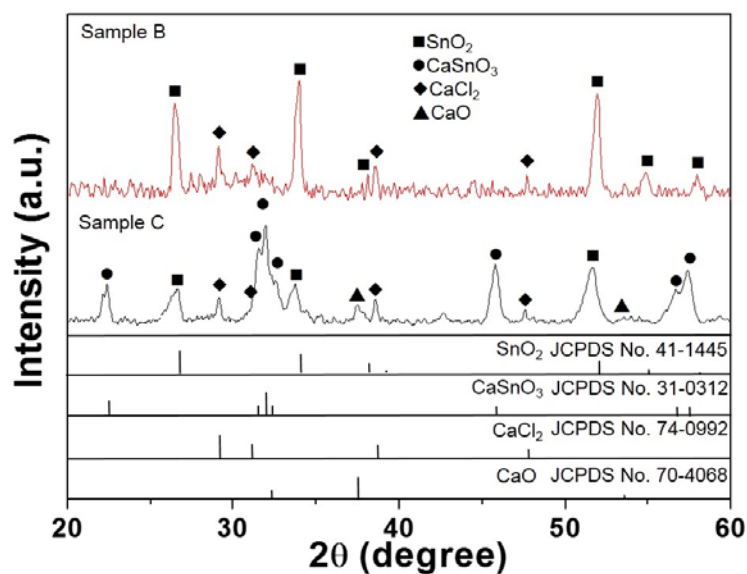


Figure 2.5 XRD patterns of samples B and C. Standard XRD patterns and the corresponding JCPDS file numbers are shown also.

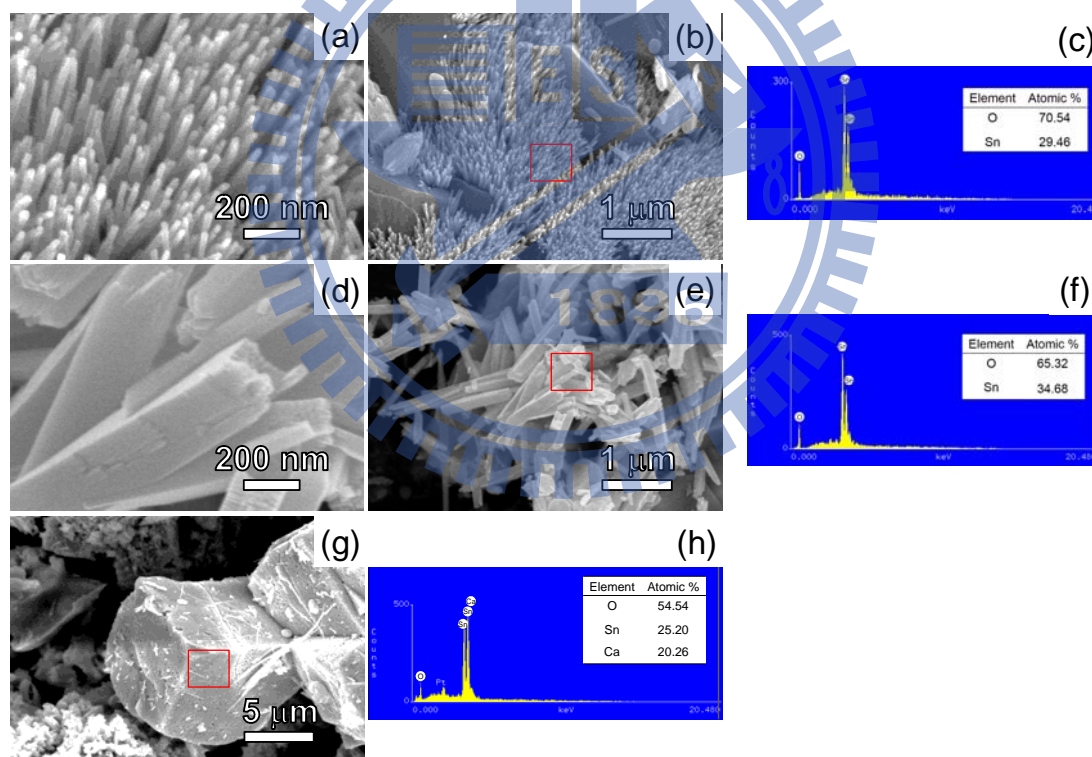


Figure 2.6 Low and high magnification SEM images of samples D and E. The EDX data are from the selected areas marked by red rectangles. Images and EDX of D are shown in (a) – (c). The data suggest that D is composed of SnO₂. Images and EDX of E are shown in (d) – (h). There two types of solids. The NRs shown in (d) and (e) are SnO₂, indicated by the EDX result in (f). According to the EDX in (h), the particles in (g) are CaSnO₃. The assignments are consistent with the XRD results shown in Figure 2.7.

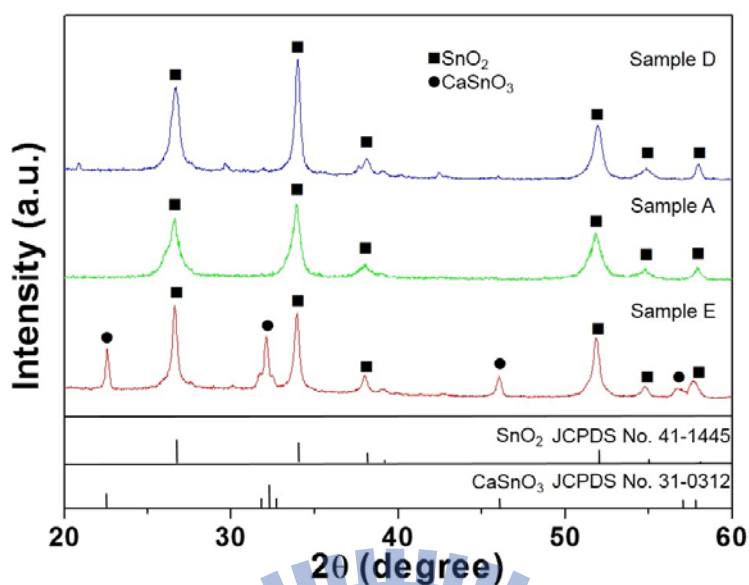
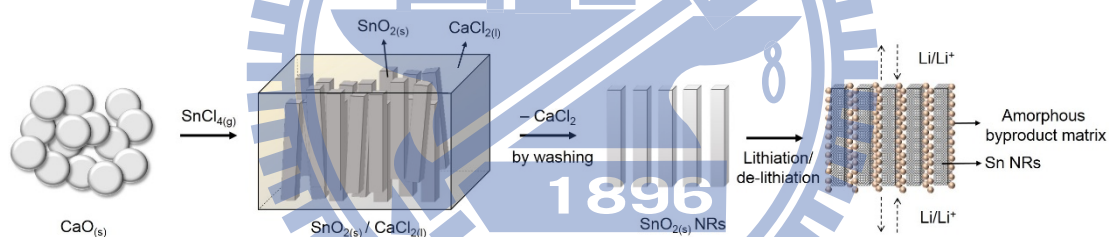


Figure 2.7 XRD patterns of samples A, D and E. Standard XRD patterns and the corresponding JCPDS file numbers are shown also.



Scheme 2.1 Proposed VSRG pathway to form SnO_2 NRs and schematic diagram showing the role of the amorphous byproduct matrix during the lithiation and de-lithiation.

2.3.3 Electrochemical properties of SnO_2 NRs

Half-cells composed of a Li foil, as the negative electrode (anode), and SnO_2 NRs, as the positive electrode (cathode), were assembled into test cells for the following electrochemical studies. To understand the electrochemical reactions during the cell cycling, CV measurements were performed and presented in Figure 2.8a. In the first cathodic sweep, a broad peak at 0.59 V is attributed to the reduction of SnO_2 to form Sn, as described in eqn (1-1), and the formation of the SEI layer.^{28,29} In the following

cycles, the peak disappears while two peaks, at 0.88 V and 1.15 V, are observed. Another peak at 0.07 V is found in the first cycle. It shifts slightly in the subsequent scans to 0.2 V with reduced peak current. The observations are attributed to the occurrence of irreversible processes initially and the formation of various Li_xSn alloys, as suggested by eqn (2-2), during the cathodic sweeps.^{30,31} In the anodic sweeps, two peaks are found. The one at *ca.* 0.61 V is assigned to the dealloying process of Li_xSn , the reverse reaction in eqn (2-2). The other peak is at *ca.* 1.34 V, which is associated with partial oxidation of Sn to form tin oxides. The signal corresponds to a small peak at *ca.* 0.55 V in the cathodic scans, indicating the reduction of the oxides to Sn metal.²⁸ Figure 2.8b depicts the specific capacity and the columbic efficiency of the discharge–charge process of the half-cell with a cycling rate 100 mA g^{-1} (0.13 C). The first discharge and charge steps deliver specific capacities 1583 and 1044 mA h g^{-1} , respectively. The large initial capacity loss can be attributed to the reduction of SnO_2 to form Sn, the formation of the SEI layer on the electrode surface during the first discharge step, and the storage of Li^+ ions in the EC/DMC-based electrolytes.^{28–31} These materials are attributed to the major components in the inactive amorphous byproduct matrix formed among the NRs and will be discussed more below. Obviously, the capacity dropped swiftly for the first twenty five cycles. In the later cycles, the specific capacity and the columbic efficiency stay relatively stable. At the end of the one hundredth cycle, a respectable specific capacity 435 mA h g^{-1} and a columbic efficiency over 98% are observed. In contrast, the cycling performances of half-cells constructed from commercial SnO_2 powders (particle sizes 1–10 μm and 100 nm) at 100 mA g^{-1} are poor, as shown in Figure 2.9a. Figure 2.9b displays the discharge capacities of the device fabricated from SnO_2 NRs at high current rates 500, 1000, and 3000 mA g^{-1} (0.63, 1.26 and 3.78 C). After one hundred cycles, the discharge (Li alloying) capacities are found to be 357, 290 and 215 mA h g^{-1} , respectively. In Figure

2.8c, a capacity 997 mA h g^{-1} is observed after the battery is cycled at 100 mA g^{-1} for five times. Then, after it is cycled at 500 mA g^{-1} , 1000 mA g^{-1} , and finally 3000 mA g^{-1} for five times each, the half-cell shows a capacity 510 mA h g^{-1} at 100 mA g^{-1} , very close to value found in the twenty fifth measurement shown in Figure 2.8b, 518 mA h g^{-1} . These observations demonstrate that even after the fast discharge–charge cycles at 3000 mA g^{-1} , the electrode did not degrade severely so that the half-cell still exhibited excellent cycling properties.



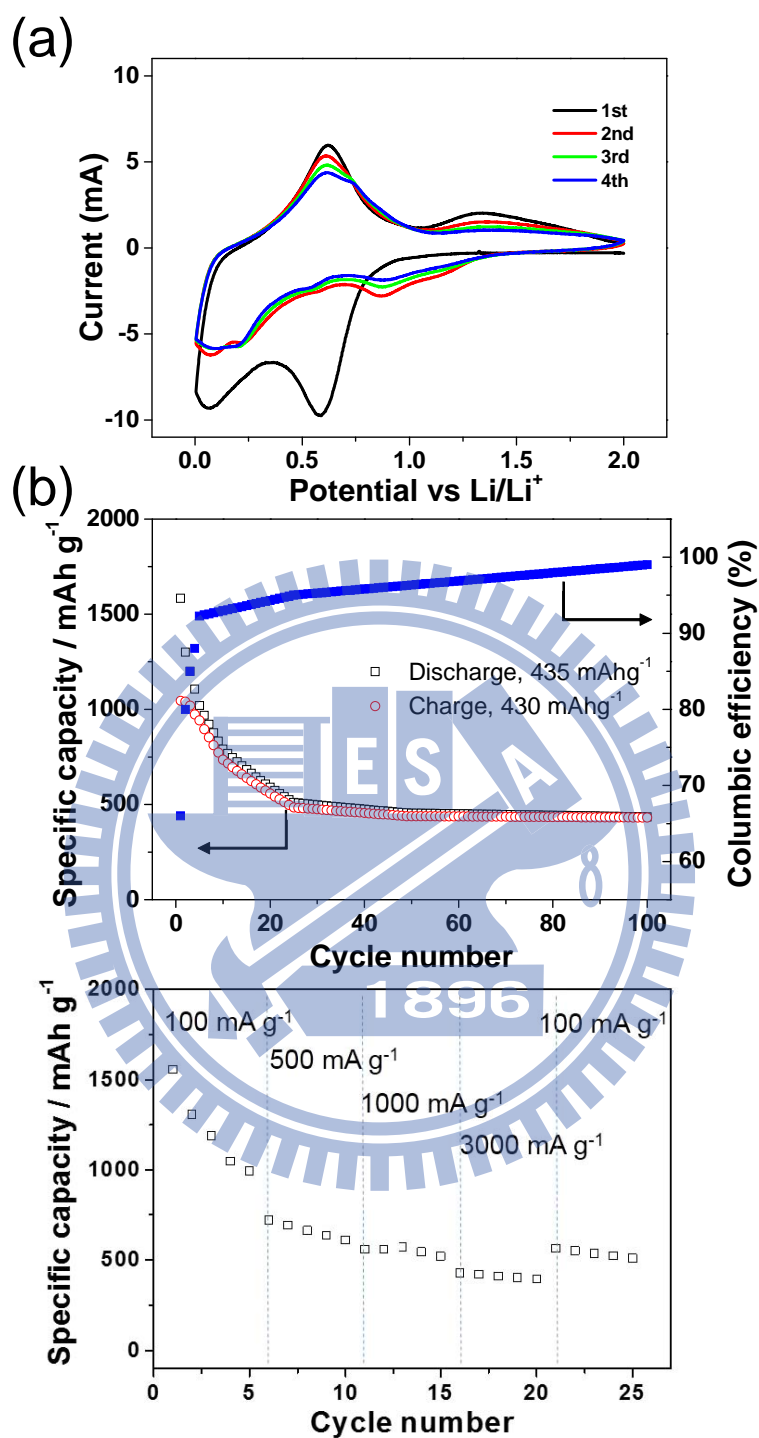


Figure 2.8 (a) CV of a SnO₂ NR electrode scanned at 0.5 mV s⁻¹. (b) Specific capacity and columbic efficiency of a SnO₂ NR electrode cycled at 100 mA g⁻¹. (c) Discharge capacity of a SnO₂ NR electrode as a function of discharge rate (100–3000 mA g⁻¹). All experiments were cycled between 0.005 V and 2.0 V vs. Li/Li⁺.

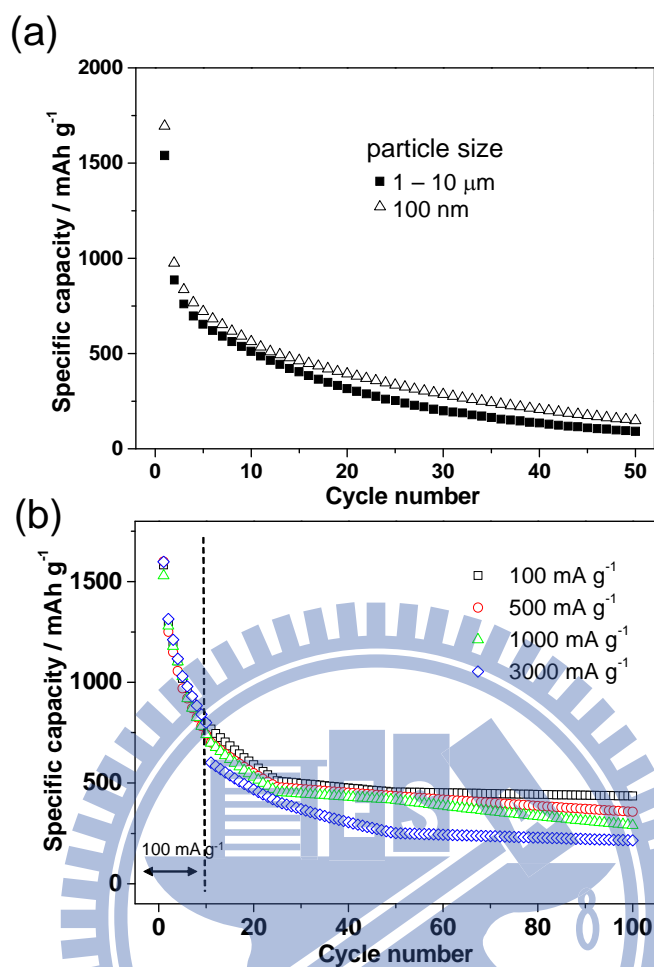


Figure 2.9 (a) Discharge capacities of electrodes fabricated from commercial SnO₂ powders (sizes: 1 - 10 μm and 100 nm) at a cycling rate 100 mA g⁻¹. (b) Electrochemical performance of a SnO₂ NR electrode cycled between 0.005 V and 2.0 V vs. Li/Li⁺ after first ten cycles were cycled at 100 mA g⁻¹, 100 mA g⁻¹ (□), 500 mA g⁻¹ (○), 1000 mA g⁻¹ (△), and 3000 mA g⁻¹ (◇).

Clearly, the half-cells constructed from the SnO₂ NRs demonstrate much better performance than the ones from the commercial SnO₂ powders do. To understand the alteration of the electrode material after repeated lithiation and de-lithiation processes, a SEM image of the electrode after one hundred discharge–charge cycles is shown in Figure 2.10a. Clearly, many NRs still maintain their original 1-D morphology when they are compared to the image of the original electrode shown in Figure 2.10b. In addition, the EDX and the XRD data of the electrode material after one hundred cycles are displayed in Figure 2.11. The EDX spectra in Figure 2.11a suggest that both Sn and

O atoms are the major components of the electrode. The XRD pattern in Figure 2.11b indicates the presence of Sn and Cu metals, which is the foil for the electrode contact. This suggests that the SnO₂ NRs has been completely converted into Sn metal NRs during the discharge–charge cycles. Based on the results, we assign the O signal found in the EDX to Li₂O, formed from the reduction of SnO₂ by Li, the irreversible decomposition of the electrolyte, and the SEI layer on the surface of the active material formed during the cell cyclings.^{20,28–33} Due to its light mass, Li cannot be observed by EDX. These inactive components appear to be amorphous because no related XRD signals can be found in Figure 2.11b. We assume that the amorphous byproduct matrix played an important role for maintaining the cell performance over extended discharge–charge cycles.³³ The soft and low density matrix appears to intersperse uniformly among the NRs. The separations could effectively minimize the aggregation of the as-formed Sn NRs. Also, due to the even distribution of the voids among the inactive matrix, the mechanical stress caused by the volume changes in the lithiation and delithiation process could be alleviated, as shown in Scheme 2.1. In contrast, the electrode fabricated from commercial SnO₂ show severe aggregations after fifty discharge–charge cycles, as demonstrated in the SEM image shown in Figure 2.12. Considering a relatively wide voltage window applied in this study, we summarize the enhanced capacity of the SnO₂ NRs based cells at long cycles and variable rates to the following reasons. First of all, the amorphous byproduct matrix in the voids among the NRs might effectively buffer the drastic volume changes during the lithiation and de-lithiation process. Also, due to the presence of the matrix, the NR structure was maintained after SnO₂ was reduced to Sn. The NR structure may provide effective electrolyte/electrode contact surfaces which shorten the transport lengths for both electrons and Li⁺ ions. In addition, the diffusion time of ions could be reduced in the nanocomposite so that the rates of phase transitions are increased.

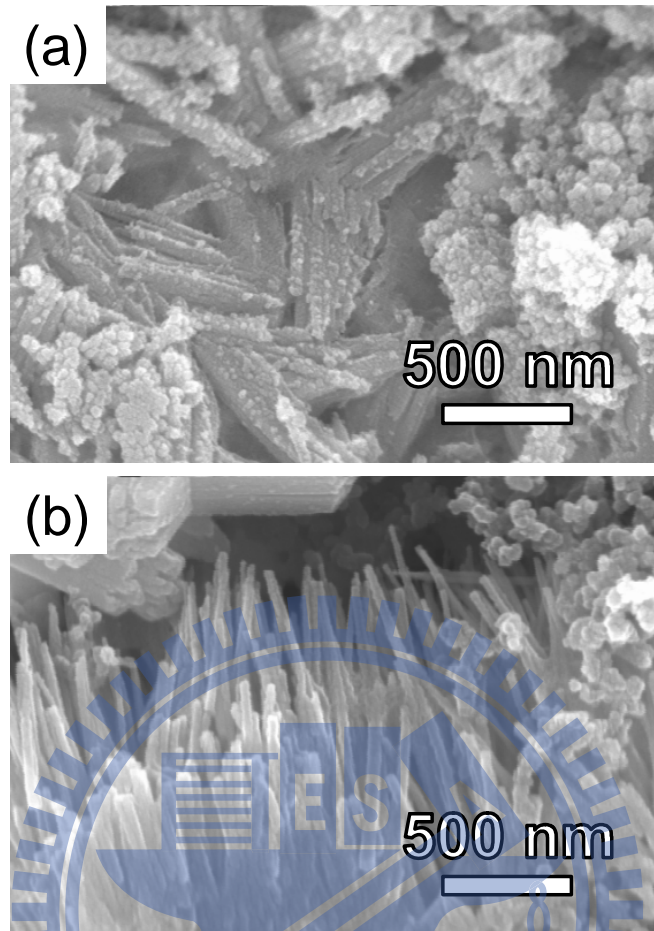


Figure 2.10 SEM images of (a) an electrode after one hundred cycles of lithiation and de-lithiation (without being washed) and (b) the original SnO₂ NR electrode. The electrode was fabricated from a mixture of SnO₂NRs, carbon black, and binder.

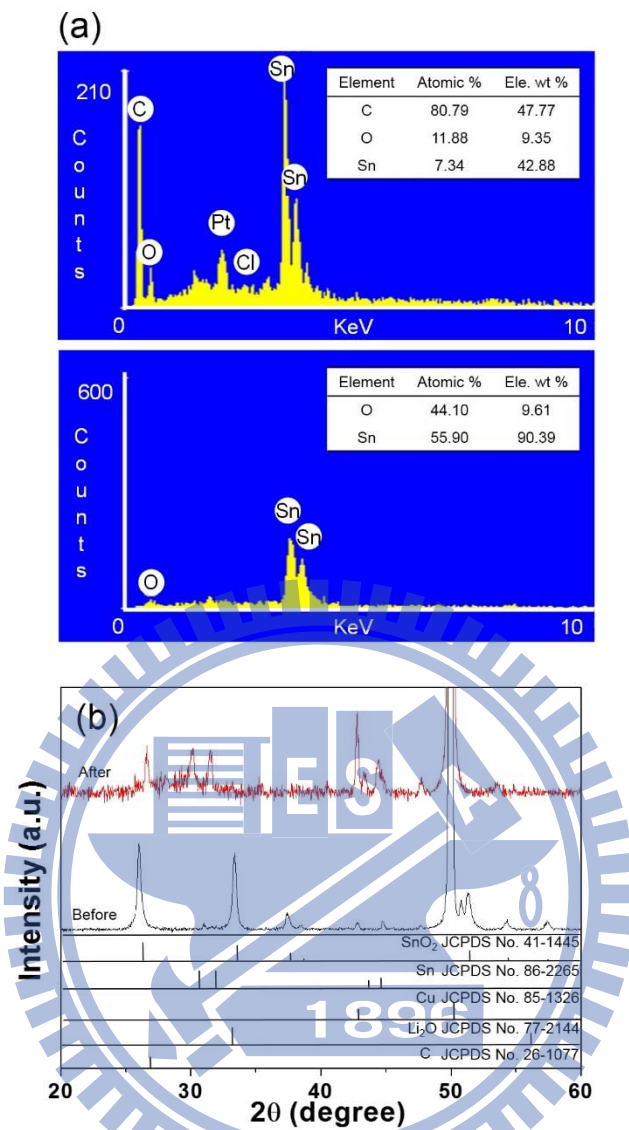


Figure 2.11 (a) EDX of a SnO₂ NR electrode after 100 cycles of lithiation and delithiation. The upper result was obtained from the whole-scan of the area shown in Figure 2.10a. The Cl content was low. The Pt signal was from the sputtered Pt metal, used to enhance the sample conductivity. The lower result was from the centre-point of one NR. (b) XRD patterns of sample A before and after 100 cycles of lithiation and delithiation. Related XRD patterns and the corresponding JCPDS file numbers are shown also.

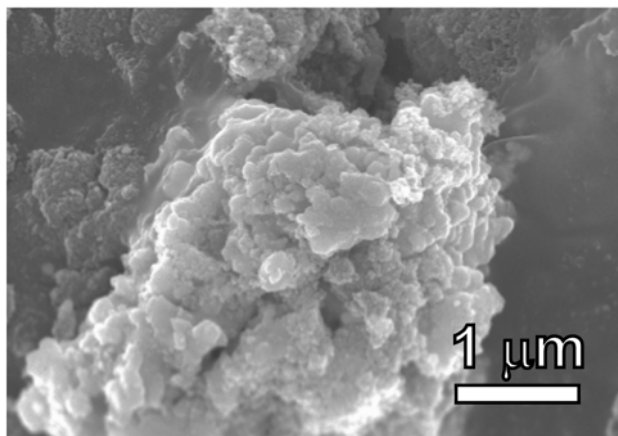


Figure 2.12 SEM image of an electrode fabricated from a mixture of commercial SnO₂ powder, carbon black, and binder after 50 cycles of lithiation and de-lithiation.

To understand the effect of the SnO₂ morphology on the electrochemical performances further, EIS studies were carried out.^{34,35} As shown in Figure 2.13a, the EIS spectra of the half-cells constructed from the NRs and the commercial powder of SnO₂ exhibit typical Nyquist plots. Each one consists of a high frequency semicircle (100 k-10 Hz) and a low frequency inclined line (10-0.1 Hz). The high frequency semicircle represents the charge transfer resistance of the electrochemical reactions across the interface between the electrolyte and the electrode surface, and the contact resistance among the components on the electrode. The semicircle from the SnO₂ NRs-based cell shows a smaller diameter, implying its better electrochemical performance.

To quantify the experimental EIS results, the spectra were fitted with the equivalent electrical circuit shown in Figure 2.13b.³⁵ It consists of a serial connection of R_e , $R_{(sf+ct)} + W//CPE$, and $R_f//C$. Here, R_e is the electrolyte resistance, $R_{(sf+ct)}$ is the surface film and charge transfer resistance, R_f is the polarization resistance, CPE (constant phase element) is the indicator for the roughness, porosity, and inhomogeneity of the electrode surface, W is the Warburg impedance, and C is the intercalation capacitance. The fitted results are listed in Table 2.3. $R_{(sf+ct)}$ of the cell value 81 Ω while the cell constructed from the commercial powder is high, 424 Ω. The observation

implies that in the cell fabricated from the SnO₂ NRs, the charge transfer and Li⁺ ion fabricated from the SnO₂ NRs exhibit a low diffusion pathways are efficient. Thus, the enhanced electrode performance can be attributed to the presence of the LiO₂/Sn NRs nanocomposite structure which not only enhances the diffusion and the charge transfer but also buffers the large volume changes during the discharge–charge cycles.

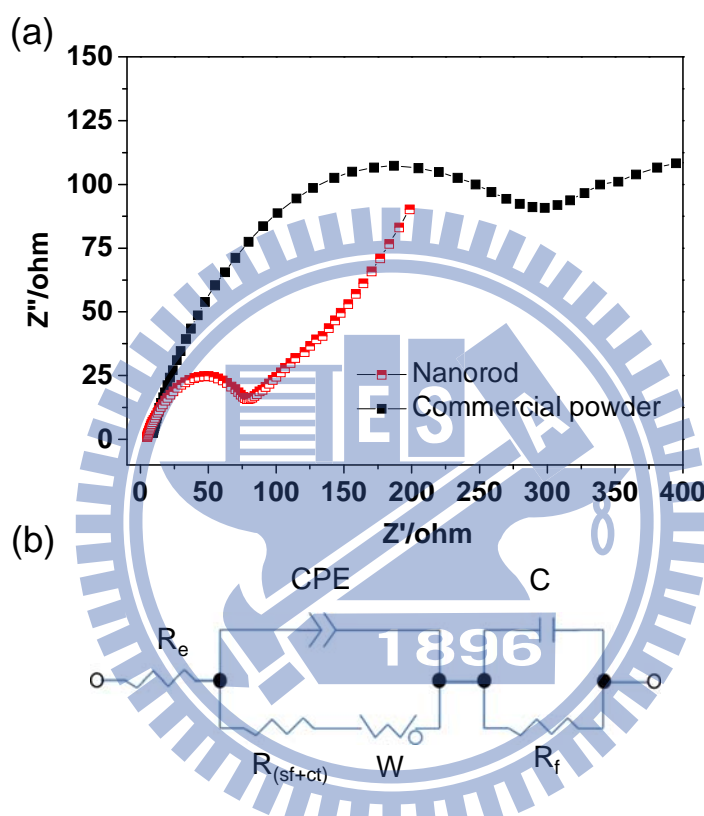


Figure 2.13 (a) Nyquist plots from coin cells composed of as-fabricated NR and commercial powder of SnO₂. (b) Equivalent circuit for experimental data fitting. R_e : electrolyte resistance; $R_{(sf+ct)}$: surface film and charge transfer resistance; R_f : polarization resistance; CPE: constant phase elements; W : Warburg impedance; C : intercalation capacitance.

Table 2.3 Fitted impedance parameters obtained from EIS using the circuit in Figure 2.13b

Electrode materials	Re (Ω)	R _(sf+ct) (Ω)	CPE (μ F)	R _f (Ω)	C (μ F)
NR	3	81	488	22	8
Commercial powder	5	424	2493	111	4

2.4 Conclusions

In summary, SnO₂ NRs have been prepared in high yields by a simple and unique process. By reacting SnCl₄ vapor with CaO solid, SnO₂ NRs are formed *via* VSRG pathway. The crystallization of SnO₂ in the phase segregated molten salt of CaCl₂ assists the growth of the NRs. The half-cells fabricated from SnO₂ NRs morphology perform much better than the ones constructed from featureless commercial SnO₂ particles do. When SnO₂ NRs are reduced by Li in the cell, Sn NRs embedded in the inactive amorphous byproduct matrix are produced. The nanocomposite provides short diffusion lengths, efficient Li⁺ ion transport, and improved charge transfer. The amorphous byproduct matrix assists maintaining the original morphology by reducing the aggregation of the NRs. The matrix also provides space to buffer the large volume changes of the electrode material during the discharge–charge cycles. As a result, the cycling performance of the electrode fabricated from the SnO₂ NRs improves significantly over that of the one constructed from the commercial SnO₂. In addition, performance of the device fabricated from our SnO₂ NRs is comparable to and exceeds many literature cases shown in Table 2.1. For example, performances of the cells constructed from SnO₂ NTs, NWs, and NPs are 250, 210, and 90 mA h g⁻¹, respectively, after fifty cycles at 100 mA g⁻¹.¹⁴ For comparison, the value of the cell fabricated from the SnO₂ NRs reported in this study is 456 mA h g⁻¹ after the same number of cycles at the same rate. In another example, a cell made from

SnO₂ nanosheets shows a capacity 559 mA h g⁻¹ after twenty cycles at 78.2 mA g⁻¹ (0.1 C).¹⁸ The result of the cell fabricated in this study is 591 mA h g⁻¹ after twenty cycles at 100 mA g⁻¹. Lastly, a cell constructed from SnO₂ hollow nanospheres retains a capacity 450 mA h g⁻¹ after 40 cycles at a rate 130 mA g⁻¹ (0.2 C).¹⁹ The performance of the cell constructed from our NRs is, as mentioned above, 456 mA h g⁻¹ after fifty cycles at 100 mA g⁻¹. At the end of the one hundredth cycle, the specific capacity is 435 mA h g⁻¹. Recently, sandwich-stacked SnO₂/Cu hybrid nanosheets have been developed to demonstrate even better performance.³⁶ We anticipate that by coupling our SnO₂ NRs with other well-designed cell structures, further LIB performance improvements may be realized.

2.5 References

1. J.-M. Tarascon and M. Armand, *Nature*, 2001, **414**, 359.
2. B. Scrosati and J. Garche, *J. Power Sources*, 2010, **195**, 2419.
3. A. S. Aricò, P. Bruce, B. Scrosati, J.-M. Tarascon and W. Van Schalkwijk, *Nat. mater.*, 2005, **4**, 366.
4. P. G. Bruce, B. Scrosati and J. M. Tarascon, *Angew. Chem. Int. Ed.*, 2008, **47**, 2930.
5. M. Winter, J. O. Besenhard, M. E. Spahr and P. Novak, *Adv. Mater.*, 1998, **10**, 725.
6. C. Yu, X. Li, T. Ma, J. Rong, R. Zhang, J. Shaffer, Y. An, Q. Liu, B. Wei and H. Jiang, *Adv. Funct. Mater.*, 2012, **2**, 68.
7. N. Liu, H. Wu, M. T. McDowell, Y. Yao, C. Wang and Y. Cui, *Nano Lett.*, 2012, **12**, 3315.
8. P.-C. Chen, M.-C. Tsai, H.-C. Chen, I. N. Lin, H.-S. Sheu, Y.-S. Lin, J.-G. Duh, H.-T. Chiu and C.-Y. Lee, *J. Mater. Chem.*, 2012, **22**, 5349.

9. Y.-C. Chang, C.-Y. Lee and H.-T. Chiu, *ACS Appl. Mat. Interfaces*, 2014, **6**, 31.
10. K.-C. Hsu, C.-E. Liu, P.-C. Chen, C.-Y. Lee and H.-T. Chiu, *J. Mater. Chem.*, 2012, **22**, 21533.
11. Y. H. Kwon, S.-W. Woo, H.-R. Jung, H. K. Yu, K. Kim, B. H. Oh, S. Ahn, S.-Y. Lee, S.-W. Song, J. Cho, H.-C. Shin and J. Y. Kim, *Adv. Mater.*, 2012, **24**, 5192.
12. M. Armand and J.-M. Tarascon, *Nature*, 2008, **451**, 652.
13. D. Ahn, X. Xiao, Y. Li, A. K. Sachdev, H. W. Park, A. Yu and Z. Chen, *J. Power Sources*, 2012, **212**, 66.
14. M.-S. Park, Y.-M. Kang, G.-X. Wang, S.-X. Dou and H.-K. Liu, *Adv. Funct. Mater.*, 2008, **18**, 455.
15. Y. Wang, J. Y. Lee and H. C. Zeng, *Chem. Mater.*, 2005, **17**, 3899.
16. M. S. Park, G. X. Wang, Y. M. Kang, D. Wexler, S. X. Dou and H. K. Liu, *Angew. Chem.*, 2007, **119**, 764.
17. J. Ning, Q. Dai, T. Jiang, K. Men, D. Liu, N. Xiao, C. Li, D. Li, B. Liu, B. Zou, G. Zou and W. W. Yu, *Langmuir*, 2009, **25**, 1818.
18. C. Wang, Y. Zhou, M. Ge, X. Xu, Z. Zhang and J. Z. Jiang, *J. Am. Chem. Soc.*, 2010, **132**, 46.
19. X. W. Lou, Y. Wang, C. Yuan, J. Y. Lee and L. A. Archer, *Adv. Mater.*, 2006, **18**, 2325.
20. D. Aurbach, E. Zinigrad, Y. Cohen and H. Teller, *Solid State Ionics*, 2002, **148**, 405.
21. M. Winter and J. O. Besenhard, *Electrochim. Acta*, 1999, **45**, 31.
22. C.-H. Wang, H.-K. Lin, T.-Y. Ke, T.-J. Palathinkal, N.-H. Tai, I. N. Lin, C.-Y. Lee and H.-T. Chiu, *Chem. Mater.*, 2007, **19**, 3956.

23. C.-H. Huang, Y.-H. Chang, H.-K. Lin, C.-W. Peng, W.-S. Chung, C.-Y. Lee and H.-T. Chiu, *J. Phys. Chem. C*, 2007, **111**, 4138.
24. L. Leibler, *Macromolecules*, 1980, **13**, 1602.
25. M. W. Matsen and F. S. Bates, *Macromolecules*, 1996, **29**, 7641.
26. Joint Committee for Powder Diffraction (JCPDS), File No. 44-1481, File No. 70-4068 and File No. 41-1445, International Center for Diffraction Data, 2002.
27. Reaction-Web, Facility for the Analysis of Chemical Thermodynamics; CRCT, <http://www.crct.polymtl.ca>.
28. R. Demir-Cakan, Y.-S. Hu, M. Antonietti, J. Maier and M.-M. Titirici, *Chem. Mater.*, 2008, **20**, 1227.
29. X. W. Lou, J. S. Chen, P. Chen and L. A. Archer, *Chem. Mater.*, 2009, **21**, 2868.
30. J. S. Chen, Y. L. Cheah, Y. T. Chen, N. Jayaprakash, S. Madhavi, Y. H. Yang and X. W. Lou, *J. Phys. Chem. C*, 2009, **113**, 20504.
31. J. Lin, Z. Peng, C. Xiang, G. Ruan, Z. Yan, D. Natelson and J. M. Tour, *ACS Nano*, 2013, **7**, 6001.
32. J. M. Haag, G. Pattanaik and M. F. Durstock, *Adv. Mater.*, 2013, **25**, 3238.
33. C.-M. Wang, W. Xu, J. Liu, J.-G. Zhang, L. V. Saraf, B. W. Arey, D. Choi, Z.-G. Yang, J. Xiao, S. Thevuthasan and D. R. Baer, *Nano Lett.*, 2011, **11**, 1874.
34. M. Wachtler, J. O. Besenhard and M. Winter, *J. Power Sources*, 2001, **94**, 189.
35. L. Li, S. Peng, J. Wang, Y. L. Cheah, P. Teh, Y. Ko, C. Wong and M. Srinivasan, *ACS Appl. Mat. Interfaces*, 2012, **4**, 6005.
36. J. Deng, C. Yan, L. Yang, S. Baunack, S. Oswald, H. Wendrock, Y. Mei and O. G. Schmidt, *ACS Nano*, 2013, **7**, 6948.

Chapter 3 Template-Free Hydrothermal Syntheses of SnO₂ Structures for Anodes in Lithium-Ion Batteries

3.1 Introduction

The development of powerful lithium-ion batteries (LIBs) with high energy capacity and long cycle life is of great importance for applications such as electric vehicles and the storage of renewable energy.¹⁻³ One of the most interesting materials is the SnO₂ that reversibly forms Li_xSn alloy with lithium and a corresponding specific capacity of 790 mA h g⁻¹, which exceed higher than the theoretical value of the traditional graphite anode, 372 mA h g⁻¹.⁴⁻⁷ However, the dramatic volume change of tin-based materials is about 300 % during the discharge and charge processes, which can result in pulverization of the initial particle morphology and cause the breakdown of electrical connection of such anode materials from current collectors, therefore leading to poor electrochemical performance.⁸⁻¹⁰ In order to solve the above intractable problems, the unique SnO₂ structures have been developed by different synthetic routes. Previous literatures have been made to fabricate nanostructured SnO₂ materials with various shapes, including nanoparticles, nanorods, nanowires, nanosheets, nanotubes, and hollow nanostructures.⁸⁻¹⁶ Among them, the hydrothermal method is recognized as a low-cost and powerful one because the solution chemical approaches can allow the growth of SnO₂ materials at relatively lower temperatures, and can be used for large-scale production.

In previous work, we have demonstrated one-dimensional (1D) SnO₂ nanorods (NRs) by reacting SnCl₄ vapor with CaO solid *via* vapor–solid reaction growths (VSRG) pathway and their lithium storage properties.¹⁷ The SnO₂ NRs embedded in an inactive

amorphous byproduct matrix, which contains Li_2O , the decomposed electrolyte, and the solid electrolyte interphase (SEI), are produced. The matrix probably buffered and reduced the stress caused by the volume change of the electrode during the cyclings. Thus, unique morphology with high surface-to-volume ratio and excellent surface activities improved significantly electrochemical performances. In this study, a simple one-pot template-free hydrothermal method is put forward for the growth of hollow spheres (HSs) and two-dimensional (2D) nanosheets (NSs) of SnO_2 by $\text{Sn}^{+4/+2}$ precursors as the reactants. The effect of morphologies on the electrochemical performance of SnO_2 as anode materials for LIBs were further evaluated.

3.2 Experimental

3.2.1 Growth of SnO_2 structures

The procedures for the fabrication of the SnO_2 hollow spheres (HSs) and nanosheets (NSs) via a hydrothermal process. In a typical experiment, the precursors, tin(IV) tetrachloride pentahydrate ($\text{SnCl}_4 \cdot 5\text{H}_2\text{O}$, Sigma-Aldrich, 98%) and tin(II) dichloride dihydrate ($\text{SnCl}_2 \cdot 2\text{H}_2\text{O}$, Alfa Aesar, 98%), were added to a basic mixture of ethanol and water. The mixture was magnetically stirred to form a turbid mixture. After that, a certain amount of 0.4 M NaOH solution was slowly added to the mixture. The pH was 12 at the end of the reaction. Finally, the obtained turbid suspension was magnetically stirred for 5 min before being transferred to a Teflon-lined stainless steel autoclave and then heated in an electric oven at 453 K for 12 hr. The products were washed with deionized (DI) water several times to remove the soluble portion. The insoluble portion was dried at 353 K overnight to offer the product.

3.2.2 Materials characterizations

Samples were characterized by using a Bruker AXS D8 Advance X-ray

diffractometer (XRD) with Cu K α 1 radiation. Scanning electron microscopic (SEM) images and energy dispersive X-ray (EDX) spectra were taken with a Hitachi S-4700I operated at 15 keV. Transmission electron microscopic (TEM), electron diffraction (ED), high-resolution TEM (HRTEM) images, and EDX data were acquired on a JEOL JEM-2010 at 200 kV. Specific surface areas of the samples was measured by an ASAP2020 system.

3.2.3 Electrochemical tests

Typically, two-electrode 2032 coin-type cells were assembled using the materials described below in a dry room. An N-methyl pyrrolidone (NMP) (Timcal) slurry was prepared by mixing SnO $_2$, carbon black (Super-P) (Timcal), and polyvinylidene fluoride (PVDF) with a weight ratio 80:10:10. A Cu foil (Furukawa) (thickness 14 μ m), vacuum dried at 403 K overnight, was compressed and cut into disks (diameter 14 mm). An electrolyte composed of LiClO $_4$ (Sigma-Aldrich) dissolved in a mixture of ethylene carbonate (EC) (Alfa-Aesar) and dimethyl carbonate (DMC) (Alfa-Aesar) (1.0 M, volume ratio 1:1) was prepared also. A Li plate was cut into disks (diameter, 14 mm) and used as both the reference and the counter electrode. The amount of the composite was weighed and combined with the electrolyte and the electrodes into coin-type cells. Electrochemical measurements were performed with a battery test system (UBIQ technology, BAT-750B). Cyclic voltammetry (CV) and electrochemical impedance spectroscopy (EIS) experiments with a high frequency semicircle (100 k–10 Hz) and a low frequency inclined line (10–0.1 Hz) were carried out using a CHI 6081C (CH Instruments) electrochemical analyzer. Electrochemical experiments of the coin-type cells were cycled between 0.005 V and 2.0 V at room temperature. Some of the devices were disassembled after the tests. The composite solids after the cycling were investigated without being washed.

3.3 Results and discussion

3.3.1 Characterization of SnO₂ HSs

SnO₂ HSs were synthesized with SnCl₄•5H₂O precursors *via* a template-free hydrothermal method. Morphology and structure of the HSs were further investigated by SEM (Figure 3.1a-3.1c) and XRD (Figure 3.1d). Obviously the particle presents a hollow-shape from Figure 1a. The thickness of the shell of the partially broken HSs is found to be around 100-300 nm estimated from Figure 3.1b. Figure 3.1b and 3.1c present the high and low magnification views that numerous HSs (diameter of sphere, *ca.* 1-3 μm) can be clearly observed. The XRD pattern in Figure 3.1d conforms that HSs is composed of SnO₂ (JCPDS card File no. 41-1445).¹⁸

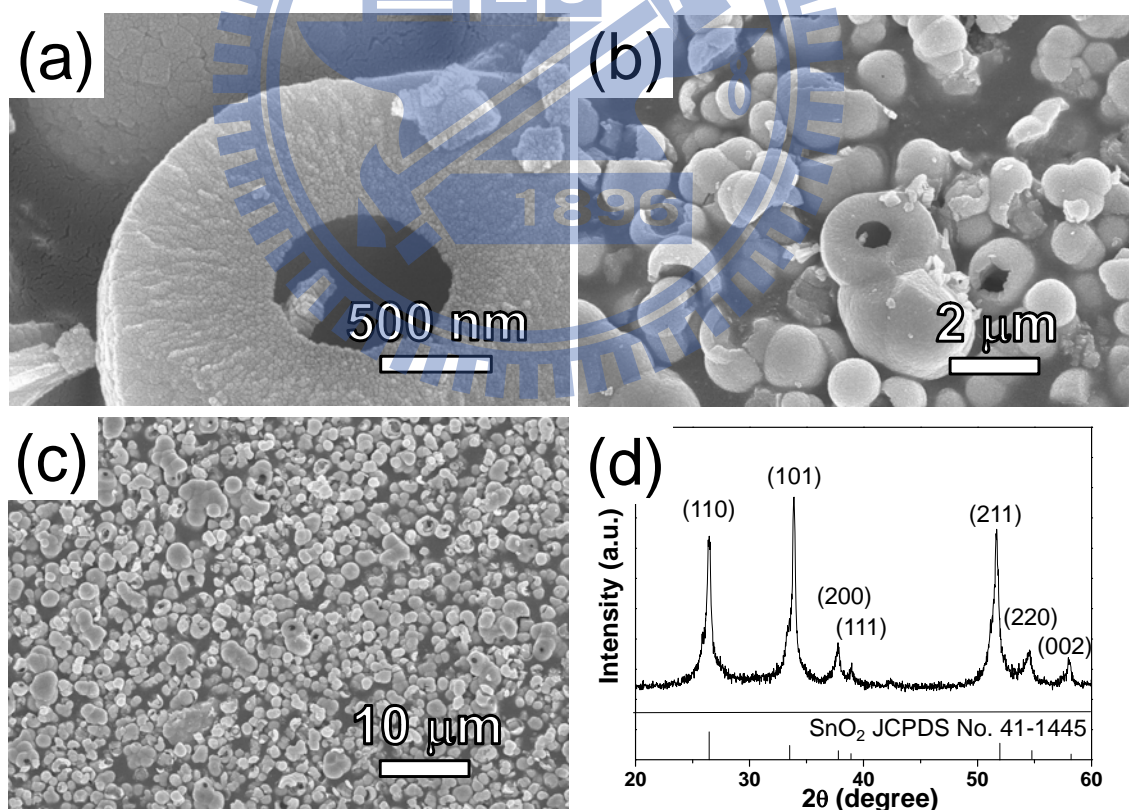


Figure 3.1 (a-c) Low and high magnifications SEM images and (d) XRD pattern of the HSs. Standard XRD pattern and the corresponding JCPDS file number are shown also.

TEM studies of HSs are shown in Figure 3.2. In Figure 3.2a, the image of a broken of a HS is presented. It confirms that the HS structure with thickness of shell 70-100 nm and diameter of sphere 700-1000 nm are observed shown. Furthermore the surface of the sphere is rough. Figure 3.2b presents a pattern composed of five diffused rings. Starting from the most inside, these are assigned to the reflections from (110), (101), (200), (210) and (211) planes of SnO₂, respectively. Figure 3.2c shows a high resolution lattice image of the sample displayed in Figure 2a. The space between the parallel fringes from the crystalline structure was measured to be 0.34 nm and 0.24 nm.¹⁸ These are equal to the spacings of the {1 1 0} and {2 0 0} planes of SnO₂, respectively. This indicates that the HS can be polycrystalline SnO₂. An EDX of sample shown in Figure 3.2d indicates that it contains both Sn and O.

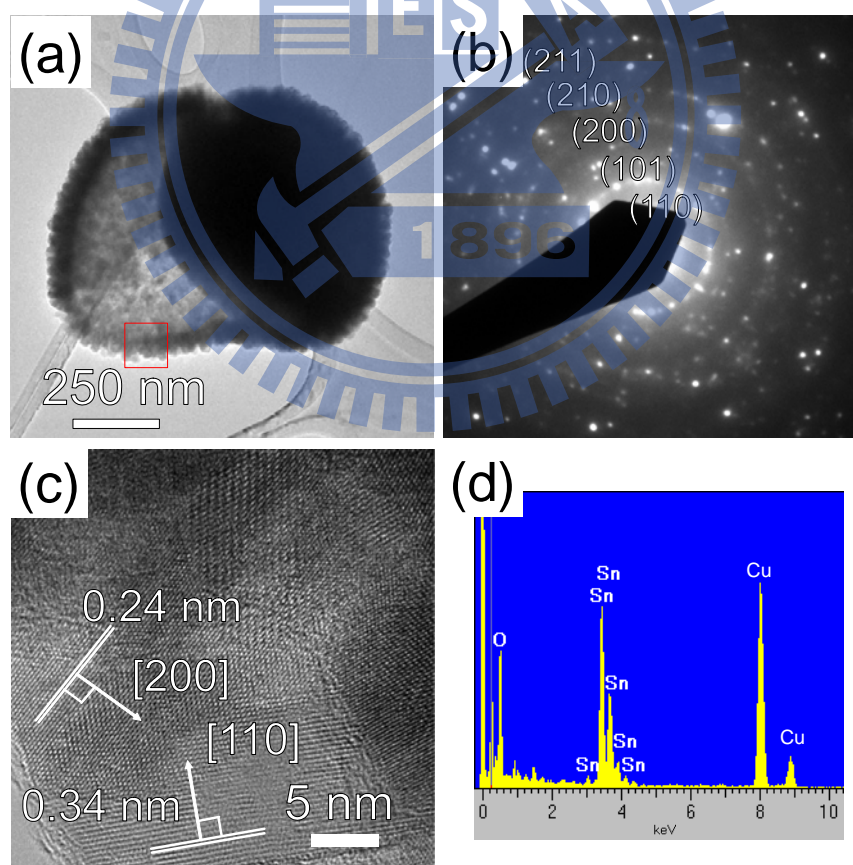


Figure 3.2 Results of TEM studies. (a) Image of a broken of HS. (b) SAED pattern and (c) HRTEM image from the squared area in (a). (d) EDX.

The reactions involved in the formation of SnO₂ HSs in the aqueous solutions can be discussed. Inside-out ripening process is a classic crystal growth mechanism wherein larger crystals grow at the expense of smaller ones, driven by the lowering of the total surface energy.^{19,20} Based on this mechanism, the growth of the SnO₂ HSs is through a self-assembly process. At the beginning of the reaction, the amorphous SnO₂ aggregates are produced. These particles would rapidly self-assembly into sphere-like crystallize on the surface of these aggregates. Outer are more stable than those that comprise the center of the aggregated structures. However, the hydrolysis reaction was slowly in alkaline media processed leading to not provide enough SnO₂ nanoparticles to growing. Thus, less crystalline are easier to dissolve and diffuse to the outer regions. After reaction, the hollow sphere structures would be formed.^{16,21}

3.3.2 Characterization of SnO₂ NSs

The morphology and structure of SnO₂ NSs were controlled by replace the precursors with SnCl₂·2H₂O precursors as the reactant, keeping other parameters unchanged and were further investigated by SEM (Figure 3.3a-3.3c) and XRD (Figure 3.3d). The thickness of the NSs is found to be around 40 nm estimated from Figure 3a. Figure 3b and 3c present the high and low magnification views that numerous NSs can be clearly observed and arranged vertically morphology. The XRD pattern in Figure 3.3d conforms that HSs is composed of SnO₂ (JCPDS card File no. 41-1445). Another the broadening of the peaks indicates the formation of Sn₂O₃ (JCPDS card File no. 25-1259).¹⁸ The tin-based compounds will be Li_xSn alloys forms to store Li⁺ ions in LIBs,¹¹⁻¹⁶ therefore the secondary phase of NSs sample do not further treatment.

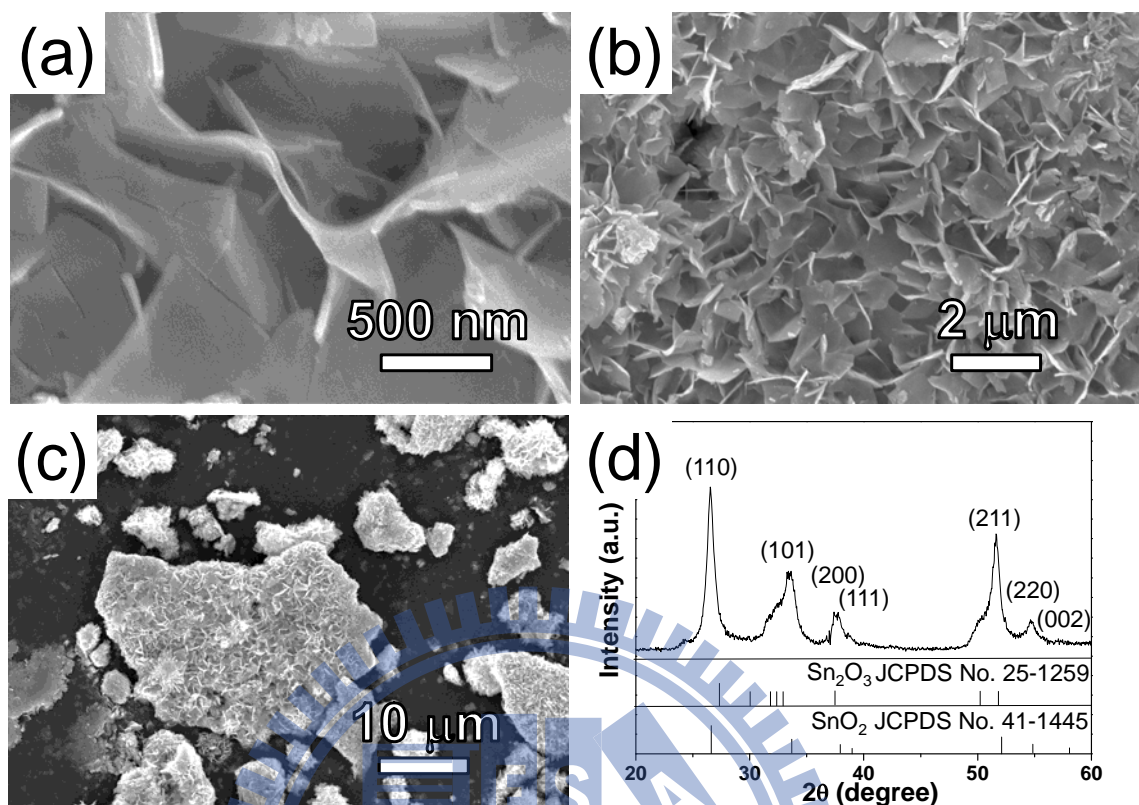


Figure 3.3 (a-c) Low and high magnifications SEM images and (d) XRD pattern of SnO₂ NSs. Standard XRD patterns and the corresponding JCPDS file numbers are shown also.

TEM studies of NSs are shown in Figure 3.4. In Figure 3.4a, the image of a fragment of a NS is presented. The SAED in Figure 3.4b shows a dot pattern. This indicates that the sample can be indexed to the [1 1 1] zone axis of the single crystalline SnO₂. From the image, the lattice parameters a and c of a tetragonal crystal system are estimated to be 0.47 nm and 0.31 nm, respectively.¹⁸ Figure 3.4c shows a high resolution lattice image of the sample displayed in Figure 3.4a. The space between the parallel fringes from the crystalline structure was measured to be 0.34 nm and 0.27 nm. These are equal to the spacings of the {1 1 0} and {1 0 1} planes of SnO₂, respectively. The NSs exhibited a single-crystalline structure with its (110) face dominated. An EDX of sample shown in Figure 3.4d indicates that it contains both Sn and O.

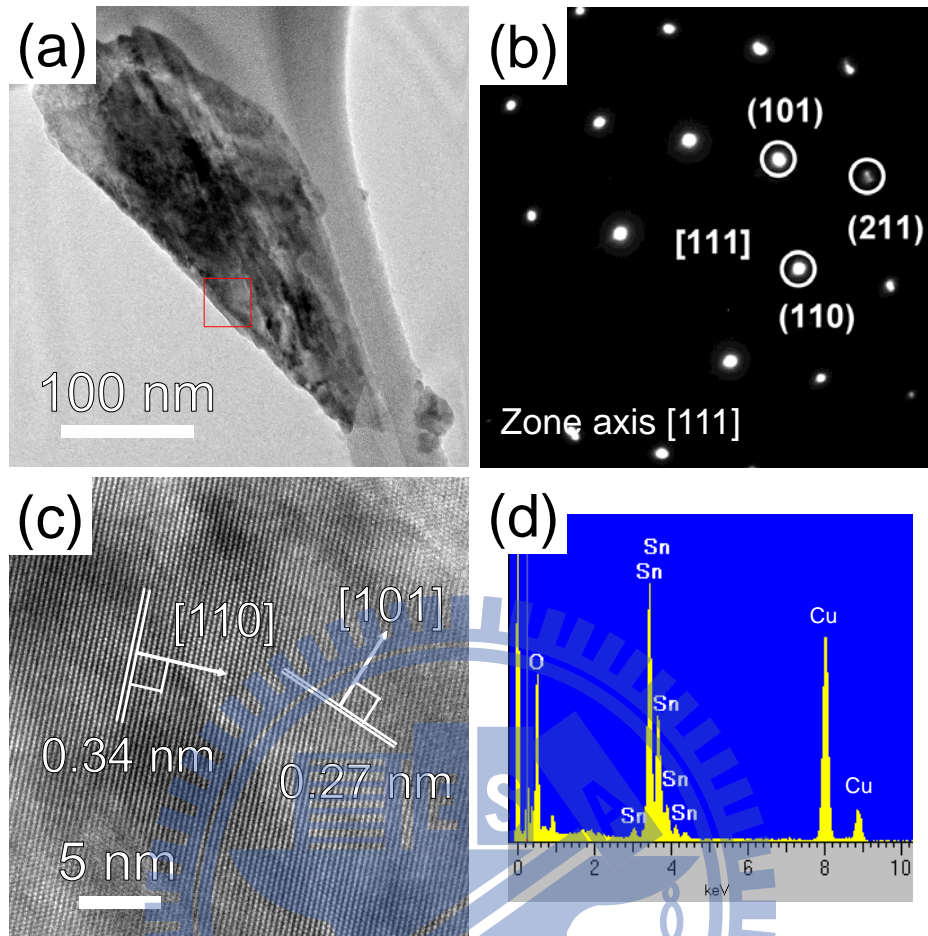


Figure 3.4 Results of TEM studies. (a) Image of a section of a sheet. (b) SAED pattern and (c) HRTEM image from the squared area in (a). (d) EDX.

Different from the formation of the SnO₂ HSs, the SnO₂ NSs were synthesized when SnCl₂•2H₂O was used as the reactant. Uchiyama et al. report the formation of SnO could be ascribed to the dehydration of basic chloride anhydrous oxide.²² Formation of SnO₂ NSs was due to the oxidation of SnO sheets during the hydrothermal treatments. On the basis of the structural similarity, it is possible that only the incorporation of an additional oxygen layer into SnO is required to obtain the SnO₂ structure. The SnO intermediate plays an important role in the formation of sheet-like structures.^{14,23}

The HSs and NSs samples are further characterized by nitrogen adsorption and desorption isotherms in Figure 3.5. The specific surface areas are measured by the Brunauer-Emmett-Teller (BET) equation. The BET surface areas of the HSs and NSs

samples were found to be $43.2 \text{ m}^2 \text{ g}^{-1}$ and $16.7 \text{ m}^2 \text{ g}^{-1}$, respectively. Both isotherms curve can be approximately classified as type IV.²⁴ The capillary phenomenon of NSs structure is more obvious at higher pressures in Figure 3.5b.

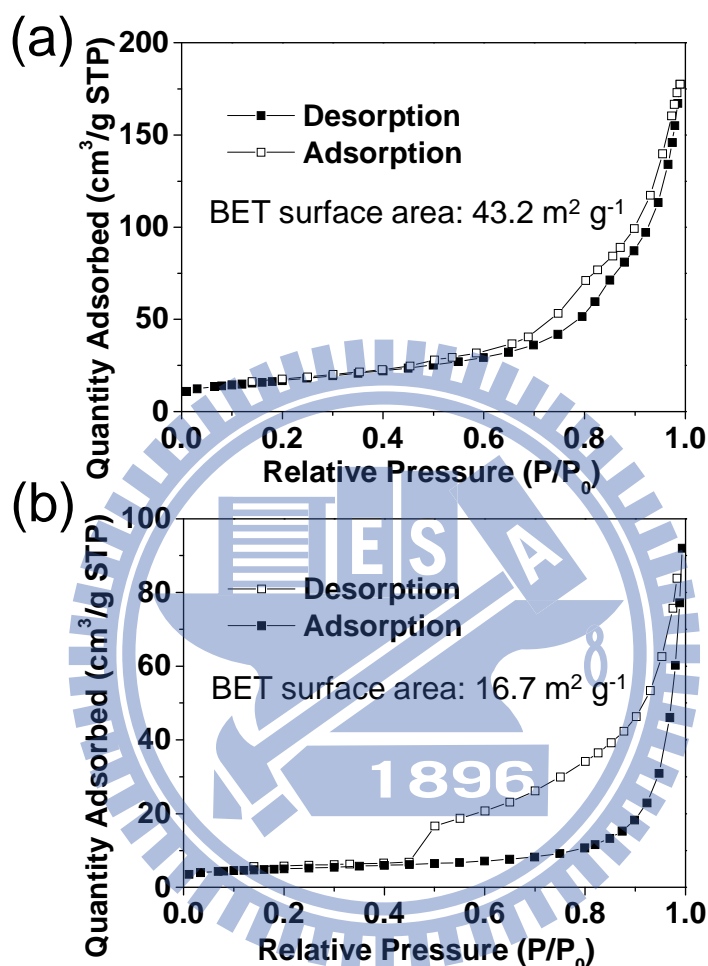


Figure 3.5 BET surface area profiles of (a) HSs and (b) NSs of SnO₂.

According to the literature report,^{25,26} the large surface area lead to multiple advances in the performance of LIBs by providing shorter path lengths for both electron and Li-ion transport. The high electrode/electrolyte contacting area helps to accommodate the strain of the Li-ion insertion/extraction. In previous work, unique structures were provided with pores or voids may act as the buffer areas to accommodate the volume expansion of the electrode material during Li alloying and dealloying processes.¹⁷ Here, we introduce distinctive electrochemical performances in

two types of SnO₂ nanomaterials with NSs and HSs. Details will be discussed more below.

3.3.3 Electrochemical properties of SnO₂

For the purpose of demonstrating the effect of morphological modification on the electrochemical performance of SnO₂, two different types of SnO₂ materials (HSs and NSs) were synthesized for use as anode materials. When SnO₂ is used as the active component in the LIBs, the electrochemical reactions are comprised of irreversible and reversible steps, (3-1) and (3-2), respectively:⁸⁻¹⁶



In the studies, half-cells composed of a Li foil, as the negative electrode (anode), and SnO₂ materials, as the positive electrode (cathode), were assembled into test cells for the following electrochemical studies. To identify the electrochemical reactions during cycling, cyclic voltammetry (CV) measurements were performed on the SnO₂ HSs and the results are presented in Figure 3.6a. In the first cathodic sweep, the HSs show two apparent reduction peaks around 0.65 V and 0.11 V, respectively. The peak at 0.65 V which can be derived from Li₂O formation and the reduction of SnO₂ to form Sn when the SnO₂ HSs react with Li⁺ as described in eqn (3-1), and the formation of a solid electrolyte interface (SEI) layer.²⁷ The peak disappear in the following cycles, indicating the irreversibility processes. The reversible peaks appear in the cathodic sweep at 0.11 V, 0.86 and 1.12V which can be attributed to the formation of Li_xSn alloys as described in eqn (3-2). In the anodic sweeps, two peaks are found. The one at *ca.* 0.60 V is assigned to the dealloying process of Li_xSn, the reverse reaction in eqn (3-2). The other peak is at 1.34 V, which is associated with partial oxidation of Sn to form tin oxides. The signal corresponds to a small peak at *ca.* 0.55 V in the cathodic scans,

indicating the reduction of the oxides to Sn metal.²⁸ In Figure 3.6b, the alloy/dealloy behavior of SnO₂ NSs for the first four cycles was also studied that found the same peaks in the CV profiles for the SnO₂ NSs over the same potential range and a similar mechanism was observed. Thus, it was confirmed that the different morphologies of materials make no difference on the redox reaction.

It is well-known that the electrochemical performance of LIBs is highly dependent on cycling rate. In this study, the cyclabilities of SnO₂ HSs and NSs at different cycling rate were compared with a voltage window of 0.005–2.0 V as shown in Figure 3.6c–3.6f and in Figure 3.7. Figure 3.6c and 3.6d depicts the specific capacity and the columbic efficiency of the discharge–charge process of the SnO₂ HSs and NSs half-cell with a cycling rate 100 mA g⁻¹ (0.13 C). In Figure 3.6c, the first discharge and charge of SnO₂ HSs deliver specific capacities 1877 and 1126 mA h g⁻¹, respectively. In Figure 3.6d, the first discharge and charge of SnO₂ NSs deliver specific capacities 1751 and 1138 mA h g⁻¹, respectively. Both specific capacities are higher than the theoretical value and lose large initial capacity that can be attributed to the reduction of SnO₂ to form Sn, the formation of the SEI layer on the electrode surface during the first discharge step, and the storage of Li⁺ ions in the EC/DMC-based electrolytes.²⁷⁻³⁰ Additionally, the SnO₂ HSs are more apparent due to its larger surface area. In the later cycles, the specific capacity and the columbic efficiency stay relatively stable. Specifically, after one hundred cycles, a higher reversible capacity of 522 mA h g⁻¹ is delivered by SnO₂ HSs as shown in Figure 3.6c and compared to 490 mA h g⁻¹ for SnO₂ NSs as shown in Figure 3.6d. In contrast, the cycling performances of half-cells constructed from commercial SnO₂ powders are poor as shown in previous report.¹⁷

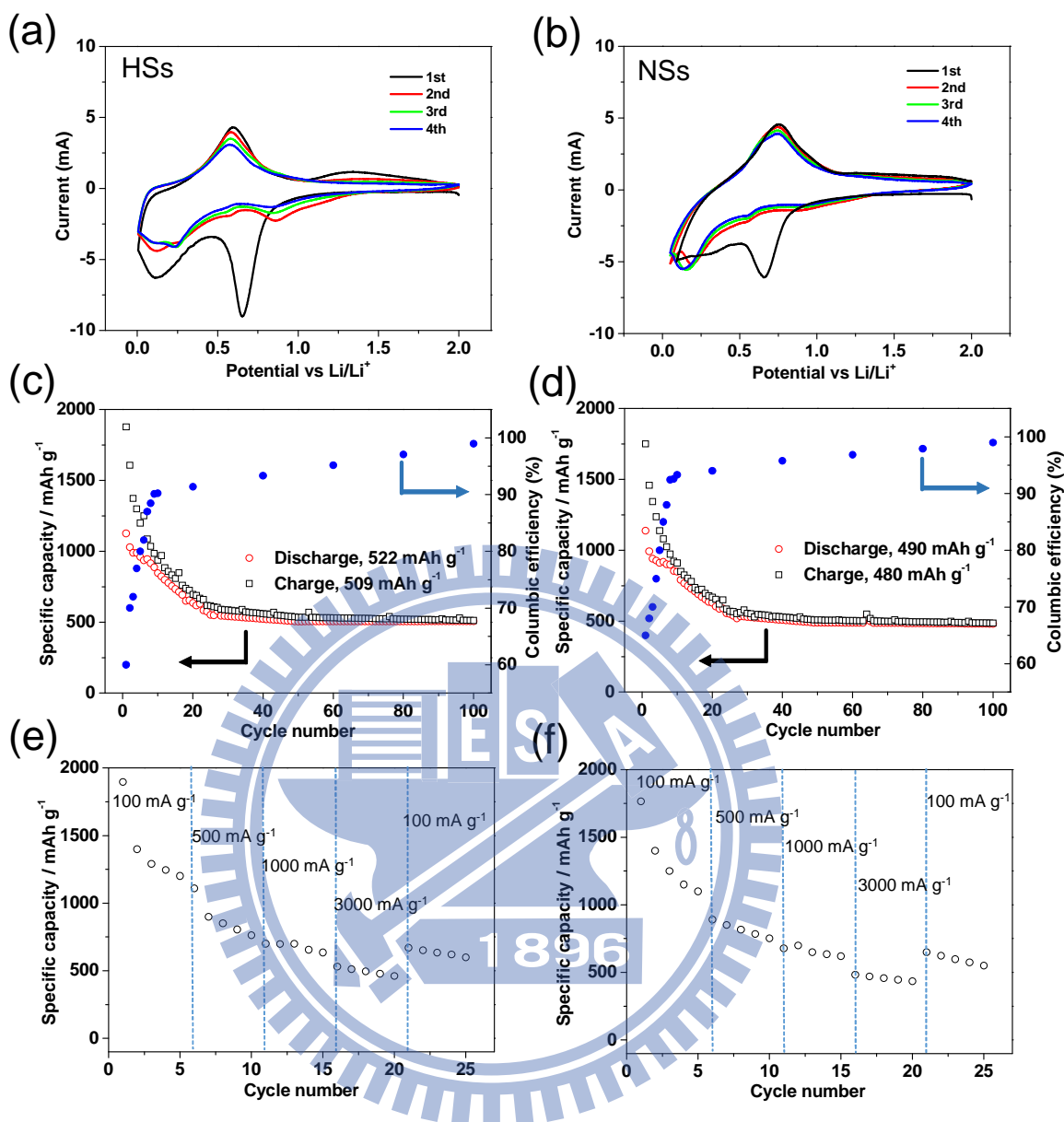


Figure 3.6 Electrochemical studies of (a, c, e) HSs and (b, d, f) NSs of SnO₂. (a, b) CVs of SnO₂ electrodes scanned at 0.5 mV s⁻¹. (c, d) Specific capacity and columbic efficiency of SnO₂ electrodes cycled at 100 mA g⁻¹. (e, f) Discharge capacities of SnO₂ electrodes at various discharge rates 100-3000 mA g⁻¹. All experiments were cycled at 0.005-2.0 V vs. Li/Li⁺.

Figure 3.7 displays the discharge capacities of the device fabricated from SnO₂ HSs and NSs at high current rates 500, 1000, and 3000 mA g⁻¹ (0.63, 1.26 and 3.78 C). After one hundred cycles, the discharge (Li alloying) of SnO₂ HSs capacities are found to be 436, 325 and 235 mA h g⁻¹, respectively. And the discharge (Li alloying) of SnO₂ NSs capacities are found to be 415, 315 and 226 mA h g⁻¹, respectively. The rate

capability of the SnO₂ with two different morphologies is evaluated at various cycling rates in Figure 3.6e and 3.6f. The specific capacity slightly decreases as the cycling rates increases, the HSs and NSs still shows a discharge capacity of 461 and 435 mA h g⁻¹ at a current density of 3000 mA g⁻¹. These observations demonstrate that even after the fast discharge-charge cycles at high cycling rate, the electrode did not degrade severely so that the half-cell still exhibited excellent cycling properties. SnO₂ HSs show the better rate performance compared with NSs at all cycling rates.

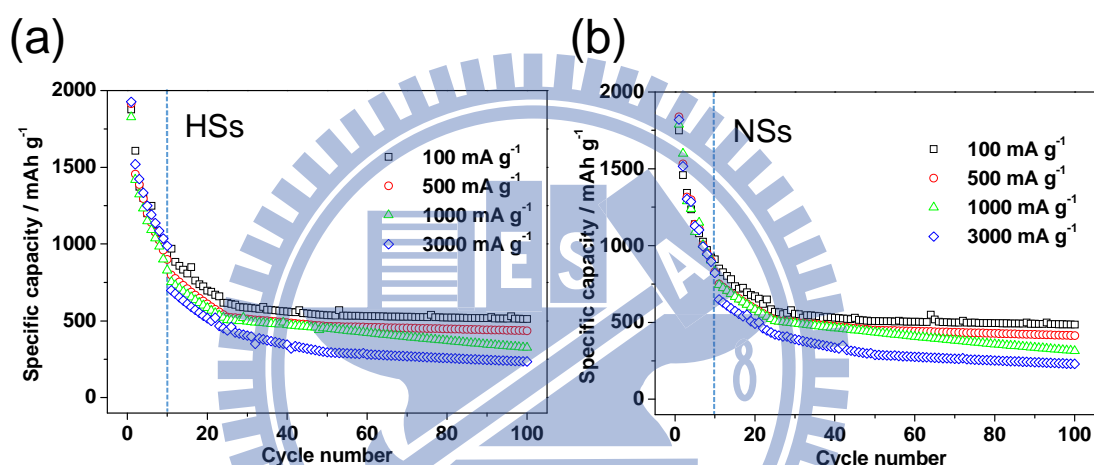


Figure 3.7 Electrochemical studies of (a) HSs and (b) NSs of SnO₂. Electrochemical performances of SnO₂ electrodes cycled at 0.005-2.0 V vs. Li/Li⁺. The first ten cycles were cycled at 100 mA g⁻¹. □: 100 mA g⁻¹, ○: 500 mA g⁻¹, △: 1000 mA g⁻¹, and ◇: 3000 mA g⁻¹.

In this studies, to understand the alteration of the SnO₂ HSs and NSs electrode material after repeated lithiation and de-lithiation processes, SEM studies and XRD of the electrode after one hundred discharge-charge cycles is shown in Figure 3.8-3.11. Based on the results and the previous work, the inactive amorphous byproduct matrix were present in the materials that formed from the reduction of SnO₂ by Li, the irreversible decomposition of the electrolyte, and the SEI layer on the surface of the active material formed during the cell cyclings. In addition, the significant improvement of the electrochemical performance is also attributed to the unique structure of SnO₂

HSs and NSs with a large contact area with short diffusion lengths, improved charge transfer and the electrolyte efficient Li^+ ion transport into the active materials. And the pores and void space between unique structures could effectively accommodate volume variations of the Sn phase during cycling, while the unique structure assemblies would probably better maintain the integrity of the electrode. Clearly, many HSs and NSs still maintain their original morphology when they are compared to the image of the original electrode shown in Figure 3.8 and 3.10. This observation lead a good cycling performance and high rate capability.

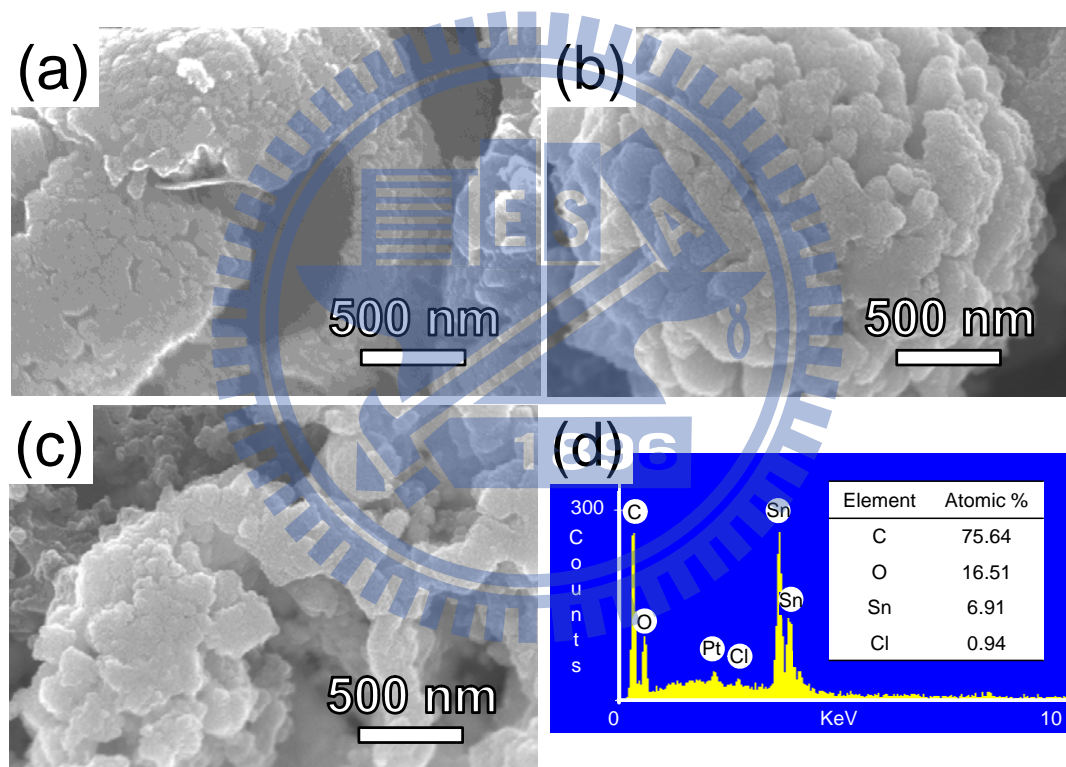


Figure 3.8 SEM images of (a) the original SnO₂ HS electrode and (b, c) the electrode after one hundred cycles of lithiation and de-lithiation (without being washed). (d) EDX of the SnO₂ HS electrode after 100 cycles of lithiation and de-lithiation. The Pt signal was from the sputtered Pt metal, used to enhance the sample conductivity. The electrode was fabricated from a mixture of SnO₂, carbon black, and binder.

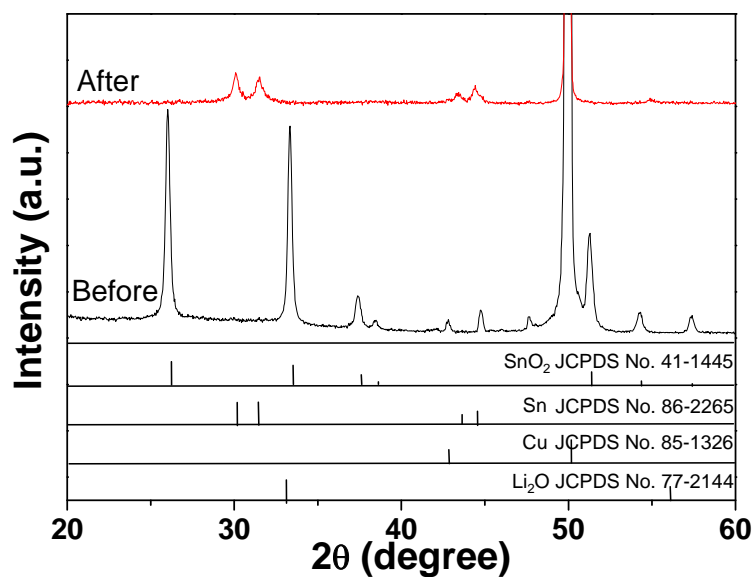


Figure 3.9 XRD patterns of the SnO₂ HS electrode before and after 100 cycles of lithiation and de-lithiation. Related XRD patterns and the corresponding JCPDS file numbers are shown also.

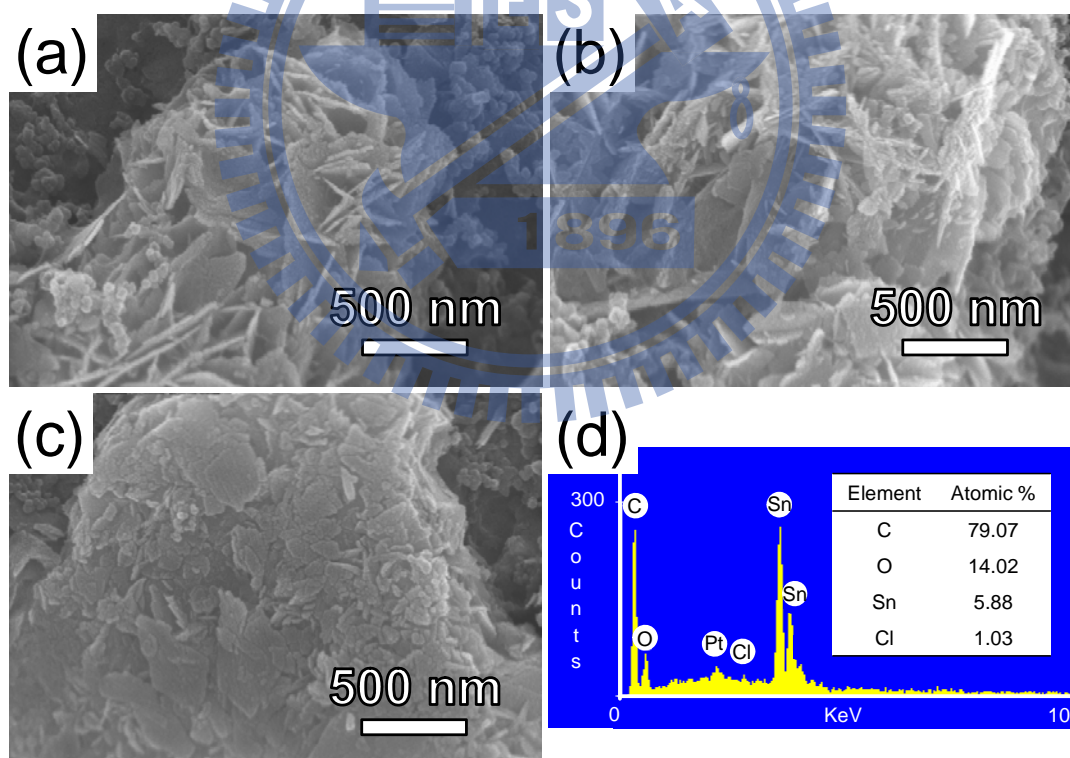


Figure 3.10 SEM images of (a) the original SnO₂ NS electrode and (b, c) the electrode after one hundred cycles of lithiation and de-lithiation (without being washed). (d) EDX of the SnO₂ NS electrode after 100 cycles of lithiation and de-lithiation. The Pt signal was from the sputtered Pt metal, used to enhance the sample conductivity. The electrode was fabricated from a mixture of SnO₂, carbon black, and binder.

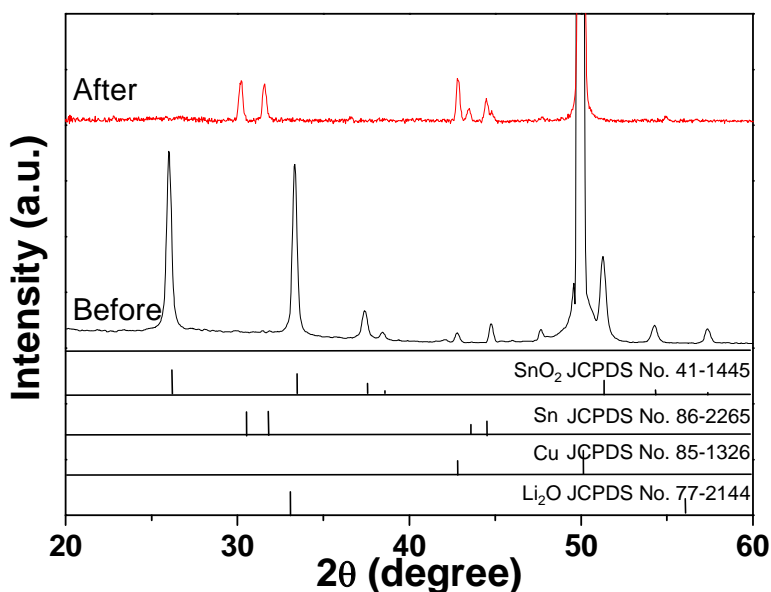


Figure 3.11 XRD patterns of the SnO₂ NS electrode before and after 100 cycles of lithiation and de-lithiation. Related XRD patterns and the corresponding JCPDS file numbers are shown also.

Electrochemical impedance spectroscopy (EIS) was conducted to determine the Li⁺ transfer behavior in SnO₂ HSs and NSs.³¹ In Figure 3.12, the EIS spectra of the half-cells constructed from the HSs and NSs exhibit typical Nyquist plots which were fitted with the equivalent electrical circuit shown in Figure 3.13. It can be observed that the NSs have a larger resistance in the high-frequency region. According to the impedance values and the shape of the curves, the HSs exhibit the lowest value of $R_{(sf+ct)}$ of 16 Ω and the NSs are 35 Ω, respectively. This may be related to the disparity between the HSs and NSs in their surface area and electronic conductivity. The value is smaller relative to commercial SnO₂ powders.

Summary, in this studies and the previous work, we test electrochemical performances in three types of SnO₂ including hollow, 2D and 1D nanomaterials such as HSs, NSs and NRs. The relationships between different structural features such as surface area and electronic conductivity from different crystallographic structures and observed electrochemical properties are discussed. Based on results, changes in the morphology of SnO₂ are not closely related with its electrochemical performance just

only a slight difference between them. We anticipate development tin-based nanocomposites containing suitably chosen matrix elements to achieve higher performance and reduce irreversibility processes.³²⁻³⁴

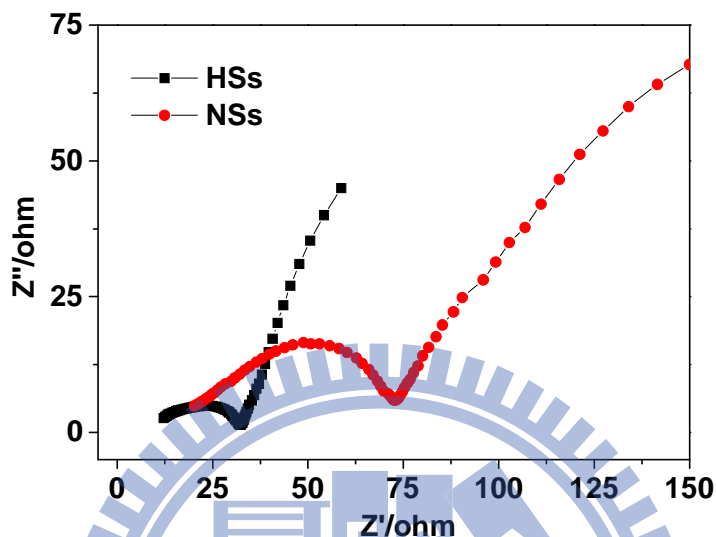


Figure 3.12 Nyquist plots from coin cells composed of as-fabricated HSs and NSs of SnO₂.

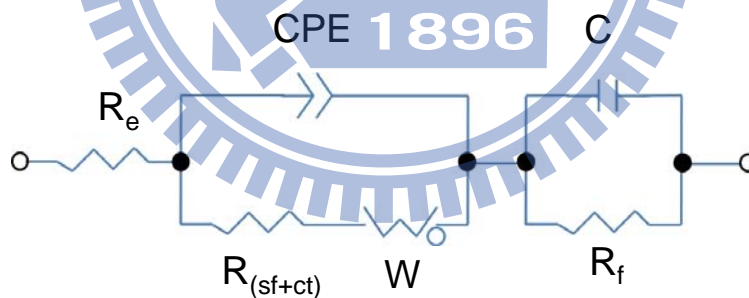


Figure 3.13 Equivalent circuit for experimental data fitting. R_e : electrolyte resistance; $R_{(sf+ct)}$: surface film and charge transfer resistance; R_f : polarization resistance; CPE: constant phase elements; W : Warburg impedance; C : intercalation capacitance.

3.4 Conclusions

In this studies, we have successfully developed a simple and template-free method to prepare SnO₂ nanomaterials by using hydrothermal. The morphologies of SnO₂ HSs and NSs could be easily controlled by adjusting Sn^{+4/+2} precursors. Electrochemical

performances revealed that the SnO₂ HSs exhibited better cyclability and rate capability, when compared with SnO₂ NSs. The reversible capacity of 522 mA h g⁻¹ was delivered after one hundred cycles at a cycling rate of 100 mA g⁻¹. These enhanced performances were caused by the unique structure, which could exhibited excellent cycling properties. The use of SnO₂ nanomaterials gives an important indication for the further improvement of the electrochemical properties of SnO₂ systems.

3.5 References

1. M. Armand and J. M. Tarascon, *Nature*, 2008, **451**, 652.
2. B. Dunn, H. Kamath and J.-M. Tarascon, *Science*, 2011, **334**, 928.
3. P. G. Bruce, B. Scrosati and J.-M. Tarascon, *Angew. Chem. Int. Ed.*, 2008, **47**, 2930.
4. X. M. Yin, C. C. Li, M. Zhang, Q. Y. Hao, S. Liu, L. B. Chen and T. H. Wang, *J. Phys. Chem. C*, 2010, **114**, 8084.
5. H. Wang, Y. Yang, Y. Liang, J. T. Robinson, Y. Li, A. Jackson, Y. Cui and H. Dai, *Nano Lett.*, 2011, **11**, 2644.
6. M. Yoshio, H. Wang, K. Fukuda, Y. Hara and Y. Adachi, *J. Electrochem. Soc.*, 2000, **147**, 1245.
7. E. Yoo, J. Kim, E. Hosono, H.-s. Zhou, T. Kudo and I. Honma, *Nano Lett.*, 2008, **8**, 2277.
8. Z. Ying, Q. Wan, H. Cao, Z. T. Song and S. L. Feng, *Appl. Phys. Lett.*, 2005, **87**, 113108.
9. M.-S. Park, G.-X. Wang, Y.-M. Kang, D. Wexler, S.-X. Dou and H.-K. Liu, *Angew. Chem.*, 2007, **119**, 764.
10. A. I. Hochbaum and P. Yang, *Chem. Rev.*, 2009, **110**, 527.
11. J. S. Chen, Y. L. Cheah, Y. T. Chen, N. Jayaprakash, S. Madhavi, Y. H. Yang and X. W. Lou, *J. Phys. Chem. C*, 2009, **113**, 20504.

12. J. Liu, Y. Li, X. Huang, R. Ding, Y. Hu, J. Jiang and L. Liao, *J. Mater. Chem.*, 2009, **19**, 1859.
13. C. Wang, G. Du, K. Ståhl, H. Huang, Y. Zhong and J. Z. Jiang, *J. Phys. Chem. C*, 2012, **116**, 4000.
14. H. B. Wu, J. S. Chen, X. W. Lou and H. H. Hng, *J. Phys. Chem. C*, 2011, 24605.
15. Y. Wang, H. C. Zeng and J. Y. Lee, *Adv. Mater.*, 2006, **18**, 645.
16. S. Han, B. Jang, T. Kim, S. M. Oh and T. Hyeon, *Adv. Funct. Mater.*, 2005, **15**, 1845.
17. K.-C. Hsu, C.-Y. Lee and H.-T. Chiu, *RSC Advances*, 2014, **4**, 26115.
18. Joint Committee for Powder Diffraction (JCPDS), File No. 41-1445 and File No. 25-1259, International Center for Diffraction Data, 2002.
19. A.-M. Cao, J.-S. Hu, H.-P. Liang and L.-J. Wan, *Angew. Chem. Int. Ed.*, 2005, **44**, 4391.
20. W. S. Choi, H. Y. Koo, Z. Zhongbin, Y. Li and D. Y. Kim, *Adv. Funct. Mater.*, 2007, **17**, 1743.
21. J. S. Chen, L. A. Archer and X. W. D. Lou, *J. Mater. Chem.*, 2011, **21**, 9912.
22. H. Uchiyama, H. Ohgi and H. Imai, *Cryst. Growth Des.*, 2006, **6**, 2186.
23. Y. Li, Y. Guo, R. Tan, P. Cui, Y. Li and W. Song, *Chin. Sci. Bull.*, 2010, **55**, 581.
24. M. Kruk and M. Jaroniec, *Chem. Mater.*, 2001, **13**, 3169.
25. C. Jiang, E. Hosono and H. Zhou, *Nano Today*, 2006, **1**, 28.
26. X. Zhao, B. M. Sánchez, P. J. Dobson and P. S. Grant, *Nanoscale*, 2011, **3**, 839.
27. Z. Wen, Q. Wang, Q. Zhang and J. Li, *Adv. Funct. Mater.*, 2007, **17**, 2772.
28. G. Kilibarda, D. V. Szabó, S. Schlabach, V. Winkler, M. Bruns and T. Hanemann, *J. Power Sources*, 2013, **233**, 139.
29. L. Zhang, G. Zhang, H. B. Wu, L. Yu and X. W. Lou, *Adv. Mater.*, 2013, **25**, 2589.
30. Y. Yang, X. Ji, F. Lu, Q. Chen and C. E. Banks, *Phys. Chem. Chem. Phys.*, 2013, **15**, 15098.

31. S. S. Zhang, K. Xu and T. R. Jow, *Electrochim. Acta*, 2006, **51**, 1636.
32. G. Chen, Z. Wang and D. Xia, *Chem. Mater.*, 2008, **20**, 6951.
33. P. Wu, N. Du, H. Zhang, C. Zhai and D. Yang, *ACS Appl. Mat. Interfaces*, 2011, **3**, 1946.
34. X. Huang, C. Tan, Z. Yin and H. Zhang, *Adv. Mater.*, 2014, **26**, 2185.



Chapter 4 One-Step Vapor–Solid Reaction Growth of Sn@C Core–Shell Nanowires as an Anode Material for Lithium-Ion Batteries

4.1 Introduction

Rechargeable lithium-ion batteries (LIBs) are important energy storage devices for mobile electronics, electric vehicles and renewable energy systems.^{1,2} To meet these applications, LIBs with high specific storage capacity and good cycle properties are essential.³ Many research results related to improving the performance and cycle life of high-capacity electrode materials, such as Fe₃O₄, MgH₂, Si, Si/C, Sn, and Sn-based composites, in LIBs have been published.⁴⁻¹⁵ Among them, metallic Sn has been demonstrated as a potential anode material for LIBs because of its high lithium-ion storage capacity.⁹⁻¹¹ Its theoretical specific capacity (Li_{4.4}Sn, 992 mA h g⁻¹) is much higher than that of graphitic carbon (LiC₆, 372 mA h g⁻¹).¹⁶⁻¹⁸ However, significant capacity fading after cycling has been a serious problem for Sn containing electrode materials. This has been attributed to enormous volume changes during charging and discharging processes leading to particle fracture and aggregation.¹⁹ In some cases, the volume expansion after cycling steps can be as high as 260%.^{17,19} In order to solve the volume expansion and fracture problems, a couple of new strategies have been explored recently. In one strategy, various Sn-containing composite materials, including core–shell structures and nanocomposites, are employed to improve the capacity and the electrochemical performance.^{9-11,14,21-26} For example, nanostructured Sn encapsulated in a hollow carbon shell can improve the electrode performance.²⁶ The shell acts as a barrier to prevent aggregation of Sn and provides a void space for the volume changes.²² Nanoparticles of Sn embedded in a C-based matrix also perform well.¹⁴ Other

representative cases are summarized in Table 4.1. In the other strategy, mesoporous Sn is used as the anode to demonstrate improved performance.¹⁵

Previously, we developed a vapor–solid reaction growth (VSRG) strategy to fabricate one-dimensional (1D) heterostructures. These include cable-like Cu nanowires (NWs), α -silica encapsulated Ag NWs, $\text{CaF}_2@ \alpha\text{-C}$ core–shell NWs, and tubular SiC.^{27–30} In the reactions, a vapor phase reactant was reacted with a solid. The as-grown solid products underwent phase-segregation and developed into 1D core–shell nanostructures. By using this strategy, we have designed a reaction in this study by employing vapor phase C_2H_2 and SnO_2 solid particles as the reactants to grow $\text{Sn}@ \text{C}$ core–shell NWs. The NWs are shown to be a stable electrode material, which leads to excellent electrochemical performance in coulombic efficiency, rate capability and capacity retention. Our observations are presented below.

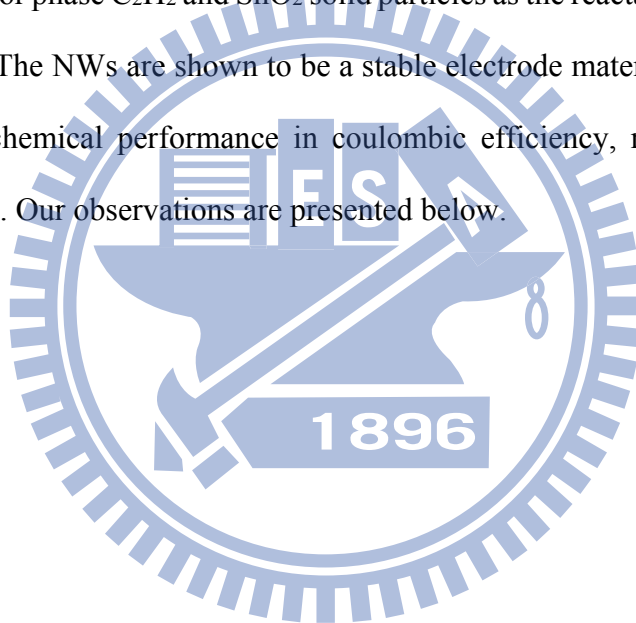
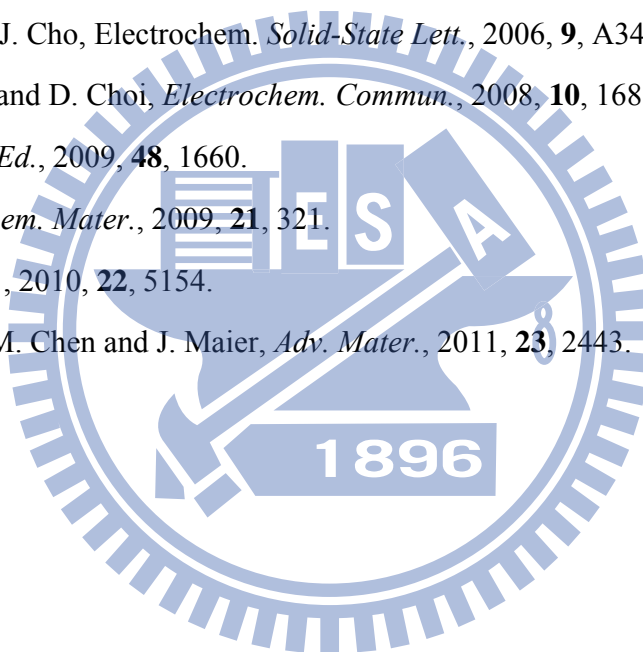


Table 4.1 Summary of electrochemical properties of Sn containing electrodes for rechargeable Li-ion batteries.

Electrode material	Morphology and Composition	Electrochemical Performance			Cathode	Ref
		Working Potential (V)	Cycling Rate	Capacity		
SnO ₂ NTs	Diameter: 180 – 230 nm	0.005 – 2	80 cycles at 0.05 mA·cm ⁻²	525 mAh/g	Li foil	21 ^a
SnO ₂ @C core/shell NTs	SnO ₂ NPs: 10 nm CNT diameter: 200 nm (SnO ₂ : 73.3 wt %)	0.005 – 3	200 cycles at 0.3 mA·cm ⁻² (0.3 mA·cm ⁻² ≅ 0.5 C)	540 mAh/g (200 mAh/g from CNT)	Li foil	22 ^b
Hydrobenzamide-capped Sn NPs	Particle size: 50 nm	0 – 1.5	30 cycles at 0.2 C (1 C = 900 mA/g)	500 mAh/g	Li foil	23 ^c
Vertical arrays of Sn NWs on Si substrates	Diameter: 50 – 100 nm	0.01 – 1.2	15 cycles at 4200 mA/g	400 mAh/g	Li foil	24 ^d
Sn@C nanocomposite	Sn@C rambutan-like nanoarchitecture (C: 73 wt %; Sn: 23 wt %)	0.005 – 2	200 cycles at 100 mA/g	311 mAh/g (168 mAh/g from C sphere)	Li foil	10 ^e
Sn@C@CNT nanostructures	Sn NPs: 50 – 170 nm C layer: 3 – 10 nm arrays of CNTs: length 30 μm diameter 180 – 280 nm	0.005 – 3	80 cycles at 0.1 mA·cm ⁻²	490 mAh/g	Li foil	9 ^f
Sn@Cu core/shell type NPs	Core, Sn NP: 8.65 nm Outer layer, Cu: 1.35 nm	2.7 – 4.3	170 cycles at 0.8 C (1C = 600 mA/g)	560 mAh/g	LiCoO ₂	25 ^g
Nanoporous Au-supported nanocrystalline Sn	Nanoporous Au Sn NPs (Au: 17.2 wt %; Sn: 82.8 wt %)	0.005 – 2 0.005 – 1	140 cycles at 0.1 C (1C = 1000 mA/g) 140 cycles at 8 C (1C = 1000 mA/g)	440 mAh/g 260 mAh/g	Li foil	11 ^h

Sn@C core/shell NWs	Core/shell NW diameter: 100 – 350 nm shell thickness: 30 – 70 nm length: tens μm (C: 91.9 at %; Sn: 8.1 at %)	0.005 – 2	100 cycles at 100 mA/g 100 cycles at 1000 mA/g 100 cycles at 3000 mA/g	525 mAh/g 486 mAh/g 290 mAh/g	Li foil	This work
---------------------	---	-----------	--	-------------------------------------	---------	-----------

- a. Y. Wang, J. Y. Lee and H. C. Zeng, *Chem. Mater.*, 2005, **17**, 3899.
- b. Y. Wang, H. C. Zeng and J. Y. Lee, *Adv. Mater.*, 2006, **18**, 645.
- c. Y. Kwon, M. G. Kim, Y. Kim, Y. Lee and J. Cho, *Electrochem. Solid-State Lett.*, 2006, **9**, A34.
- d. J.-H. Kim, S. Khanal, M. Islam, A. Khatri and D. Choi, *Electrochem. Commun.*, 2008, **10**, 1688.
- e. D. Deng and J. Y. Lee, *Angew. Chem. Int. Ed.*, 2009, **48**, 1660.
- f. Y. Wang, M. Wu, Z. Jiao and J. Y. Lee, *Chem. Mater.*, 2009, **21**, 321.
- g. M. G. Kim, S. Sim and J. Cho, *Adv. Mater.*, 2010, **22**, 5154.
- h. Y. Yu, L. Gu, X. Lang, C. Zhu, T. Fujita, M. Chen and J. Maier, *Adv. Mater.*, 2011, **23**, 2443.



4.2 Experimental

4.2.1 Growth of Sn@C core-shell NWs

The growths were carried out inside a hot-wall reactor composed of a Lindberg tubular furnace and a quartz tube (diameter 27 mm). A summary of the experimental conditions for the preparation of A and B is given in Table 4.2. SnO₂ powders (0.20 g, 1.3 mmol, Sigma-Aldrich) were uniformly placed in a quartz boat (length 10 cm) at the center of the furnace. At atmospheric pressure, C₂H₂ (3 sccm) mixed with Ar was passed into the reactor and reacted with SnO₂ at a designated temperature and time period. After the reactor was cooled naturally in Ar to room temperature, black products were collected.

Table 4.2 Summary of Sn@C NW samples

Sample	SnO ₂ size (μm)	C ₂ H ₂ (sccm)	Ar (sccm)	Growth temperature (K)	Growth time (h)	Morphology	Sn-C at% ratio	Electrochemical performance
A	0.1	3	150	973	8	Length 2–5 μm, diameter 200–350 nm, shell thickness 30–70 nm	8.1/91.9	525 mA h g ⁻¹ at 100 mA g ^{-1b} 486 mA h g ⁻¹ at 1000 mA g ^{-1b} 290 mA h g ⁻¹ at 3000 mA g ^{-1b}
B ^a	5	3	90	923	10	Length 5–10 μm, diameter 150–200 nm, shell thickness 30–70 nm	11.0/89.0	102 mA h g ⁻¹ at 100 mA g ^{-1c}

^a Contained unreacted SnO₂ 24.5%. Estimated from the relative intensity ratio of SnO₂ (110)/Sn (200) (0.68/0.32) in the XRD pattern. ^b 0.005–2 V, after 100 cycles. ^c 0.005–3 V, after 50 cycles.

4.2.2 Materials characterizations

Samples were characterized by XRD using a Bruker AXS D8 Advance with Cu K_{α1} radiation. SEM images and EDX spectra were taken with a Hitachi S-4000, a Hitachi S-4700I and a JEOL JSM-7401F operated at 15 keV. TEM, ED, HRTEM images and EDX data were acquired on a JEOL JEM-3000F at 300 kV and a JEOL JEM-2010 at 200 kV. Raman spectra were measured by a high resolution confocal Raman microscope (Horiba, LabRAM HR800) with an excitation wavelength of 633 nm and a portable Raman spectrometer (MiniRam II Raman spectrometer system) with an excitation wavelength of 785 nm. TGA studies were conducted using a Netzsch STA 409 PC in an O₂ environment to estimate Sn and C contents in samples.

4.2.3 Electrochemical tests

Electrochemical measurements were performed with a battery test system (Arbin Testing System). Typically, a two-electrode 2032 coin-type cell employing one of the composite powders and a Li foil as the electrodes was assembled in a dry room. An N-methyl pyrrolidone (NMP) slurry, prepared by mixing the composite powder, carbon black (Super-P), and the binder poly-(vinylidene fluoride) (PVDF) with a weight ratio of 80 : 10 : 10 was uniformly applied on to a Cu foil (thickness 14 μm). The foil was vacuum dried (403 K) overnight, compressed, cut into disks (diameter 14 mm), and combined with the electrolyte and the other electrode. The electrolyte was made of LiClO_4 dissolved in a mixture of ethylene carbonate (EC) and dimethyl carbonate (DMC) (1.0 M, volume ratio 1 : 1). A Li plate was cut into disks (diameter, 14 μm) and used as both the reference and the counter electrode. CV experiments were carried out using a CHI 6081C (CH Instruments) electrochemical analyzer. Electrochemical experiments of the coin-type cells were cycled between 0.005 V and 2.0 V at room temperature. During the battery assembly, the amount of the composite was weighed for electrochemical performance estimation. Some of the devices were disassembled after the tests so that the composite solids could be investigated further.

4.3 Results and discussion

The reactions for the fabrication of Sn@C core-shell NWs were carried out in a horizontal hot-wall quartz tube reactor. SnO_2 powders in a quartz boat inside the reactor were reduced at high temperatures by a flowing mixture of C_2H_2 and Ar at atmospheric pressure. At the end of each reaction, black products were collected as the product. By varying the particle sizes and quantity of SnO_2 and the reaction conditions, products with various morphology were collected. Products A and B, as summarized in Table 4.2, are listed as the examples in this article.

4.3.1 Characterization of Sn@C core-shell NWs

Scanning electron microscopic (SEM) images of samples A and B are shown in Figure 4.1. In the low magnification views Figure 4.1a and 4.1c, numerous one-dimensional NWs with lengths up to tens of micrometers are observed. Magnified images in Figure 4.1b and 4.1d suggest that diameters of the NWs in A and B are hundreds of nanometers. The insets reveal that the NWs contain an apparent core-shell tubular structure. It is easy to perceive the contrast differences displayed within these images, from the side-view and the top-view of the NWs in Figure 4.1b and 4.1d, respectively. An energy dispersive X-ray (EDX) spectrum of A displayed in Figure 4.2 indicates that the core-shell NWs contain both C and Sn. The presence of metallic Sn (JCPDS card file no. 86-2265) in both A and B is confirmed by the XRD patterns shown in Figure 4.3³¹. Product B, probably due to large original SnO₂ sizes, still contains unreacted SnO₂ as suggested by its diffraction pattern observed in the XRD (JCPDS card file no. 72-1147).³¹ In Figure 4.4, Raman spectra of A and unprocessed SnO₂ are compared. For A, two broad bands at 1328 cm⁻¹ and 1583 cm⁻¹ are observed. They correspond respectively to D band and G band, with a D/G intensity ratio of 1.46, of a less-ordered carbon material.³²⁻³⁴ Because no signals of SnO₂ are observed, we conclude that A does not contain any unreacted oxide. The quantities of Sn and C in A are estimated using the results from a thermogravimetric analysis (TGA) shown in Figure 4.5. After A was heated to 1273 K in an O₂ environment, obvious weight decrease was observed above 850 K. By assuming all Sn and C in A were fully oxidized, we estimate that the Sn and C contents are 8.1 at% and 91.9 at%, respectively. Morphology of the samples prepared under other reaction conditions is shown in the SEM images in Figure 4.6. From Figure 4.6b, the lowest NW growth temperature is determined to be 923 K.

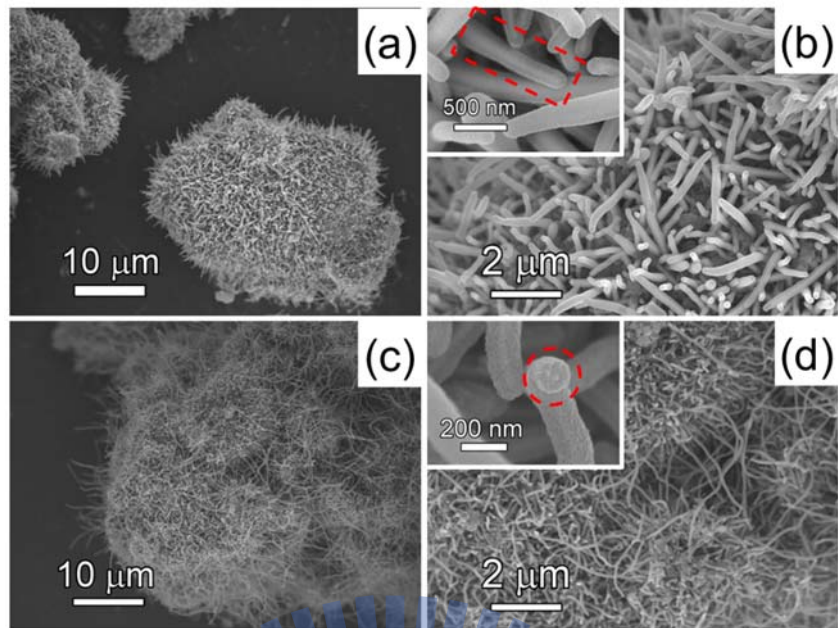


Figure 4.1 SEM images. (a) Low and (b) high magnification views of product A. (c) Low and (d) high magnification views of product B. The core-shell structures can be observed in the regions marked in the insets.

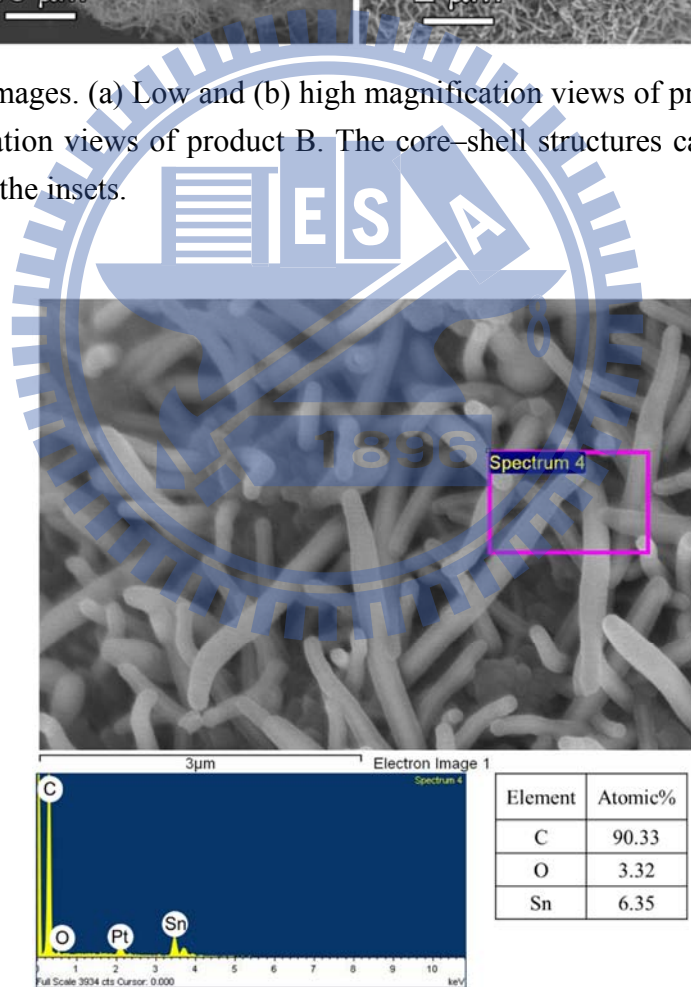


Figure 4.2 SEM image and energy dispersive X-ray spectrum (EDX) of product A.

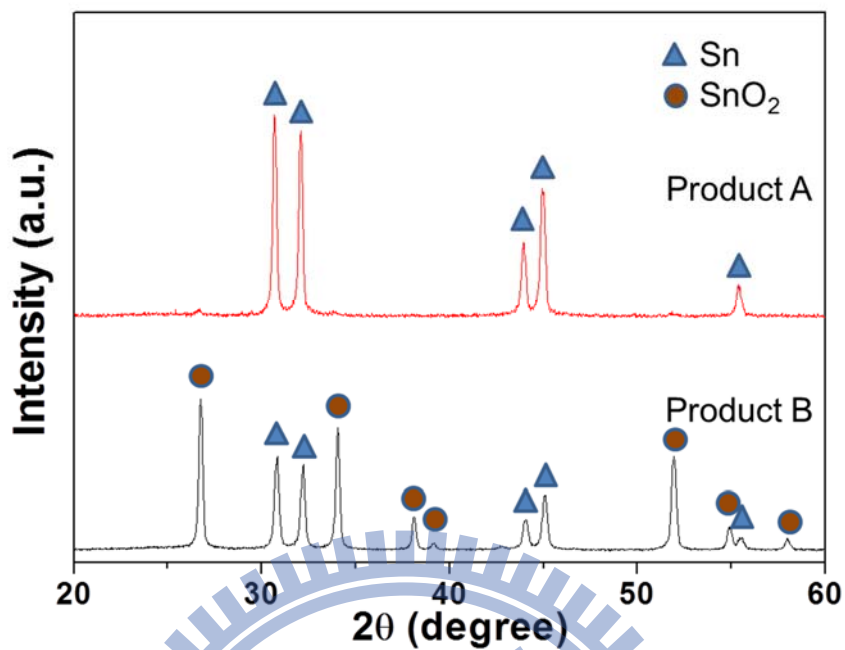


Figure 4.3 XRD patterns of products A and B.

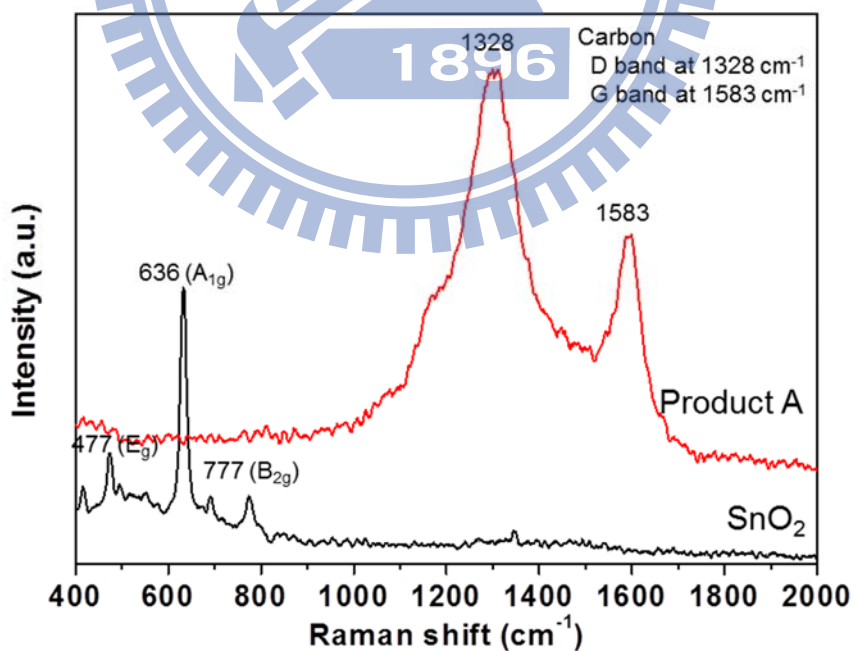


Figure 4.4 Raman spectra of product A and SnO₂. (Excitation wavelength: 785 nm, power: 5 mW)

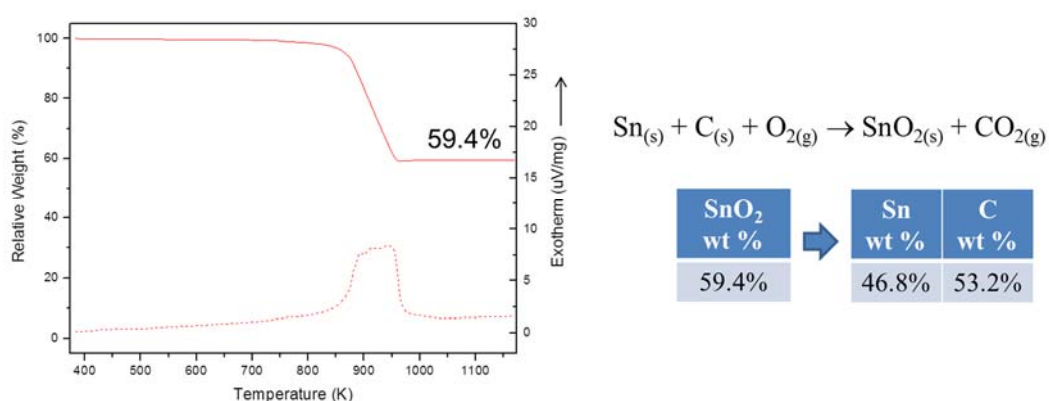


Figure 4.5 Thermogravimetric analysis (TGA) profile of A. The Sn and C contents are estimated to be 46.8 wt % (8.1 at %) and 53.2 wt % (91.9 at %), respectively. The analysis was taken in O₂ using a heating rate of 10 K min⁻¹.

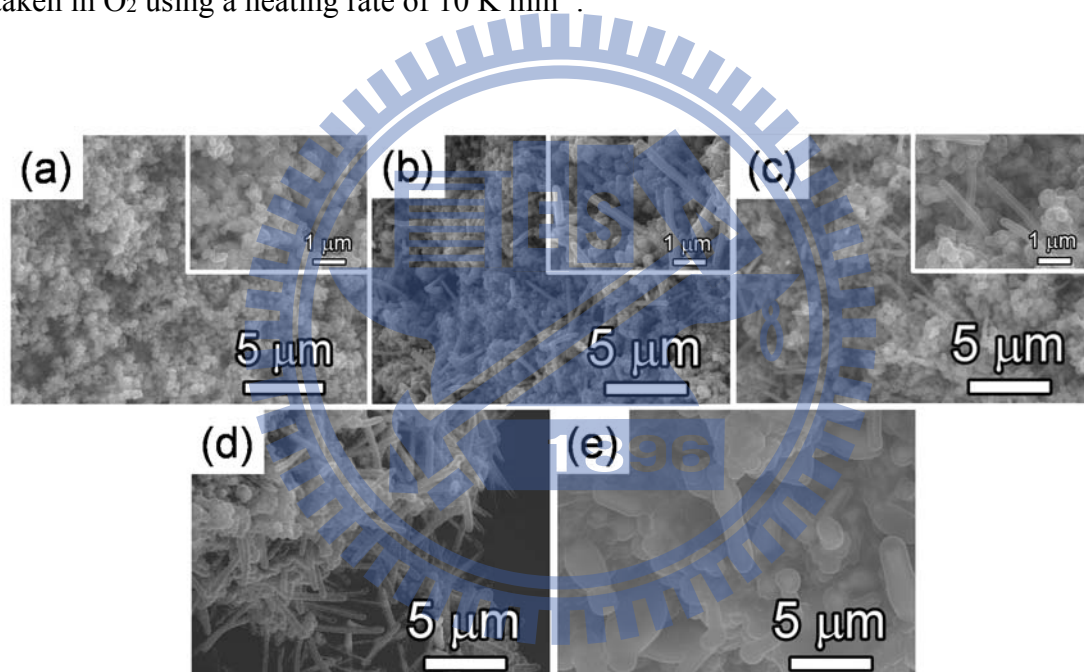


Figure 4.6 SEM images of samples prepared at (a) 873 K for 60 min, (b) 923 K for 30 min, (c) 973 K for 30 min, (d) 1073 K for 30 min, and (e) 1123 K for 30 min. C₂H₂ was flowing at 3 sccm under atmospheric pressure.

Results of transmission electron microscopy (TEM) studies of A are shown in Figure 4.7. From the images of several samples, Figure 4.7a–c, it is confirmed that the NWs have a core–shell structure with diameters 200–350 nm and shell thicknesses 30–70 nm. Inside the shell, in some cases, the inner core fills the space completely, as shown in Figure 4.7a. On the other hand, more partially filled NWs are formed, as shown in a couple of examples in Figure 4.7b.

From a section of a broken NW, low and high magnification views are shown in Figure 4.7c and d, respectively. From Figure 4.7d, selected area electron diffraction (SAED) patterns are taken and shown in Figure 4.7e and f. They correspond to the shell and the core, respectively. Figure 4.7e presents a pattern composed of three diffused rings. Starting from the most inside, these are assigned to the reflections from (005), (105) and (202) planes of the less ordered C. A dot pattern displayed in Figure 4.7f suggests that the core can be indexed to the 0 0 1 zone axis of single crystalline Sn. From the image, the lattice parameters a and c of a tetragonal crystal system are estimated to be 0.58 nm and 0.32 nm, respectively.³¹ Figure 4.7g shows a high resolution lattice image of the core. Two sets of parallel fringes, spaced at 0.29 nm and 0.21 nm, are observed. These are assigned correspondingly to the spacings of $\{0\ 2\ 0\}$ and $\{2\ 2\ 0\}$ planes of crystalline Sn. Combined with the SAED result, the growth of the Sn core is determined to be along the $[2\ 4\ 0]$ axis. An EDX spectrum shown in Figure 4.7h confirms that the NW contains both C and Sn. In a series of TEM images presented in Figure 4.8, it is suggested that the Sn core inside the C shell was liquefied upon continuous electron beam irradiations, as shown by the extending Sn boundary in the void displayed in the images. The presence of the cavities inside C shells is known to accommodate enormous volume variations during Li alloying and dealloying processes in anodes fabricated from Sn containing materials.^{9,10}

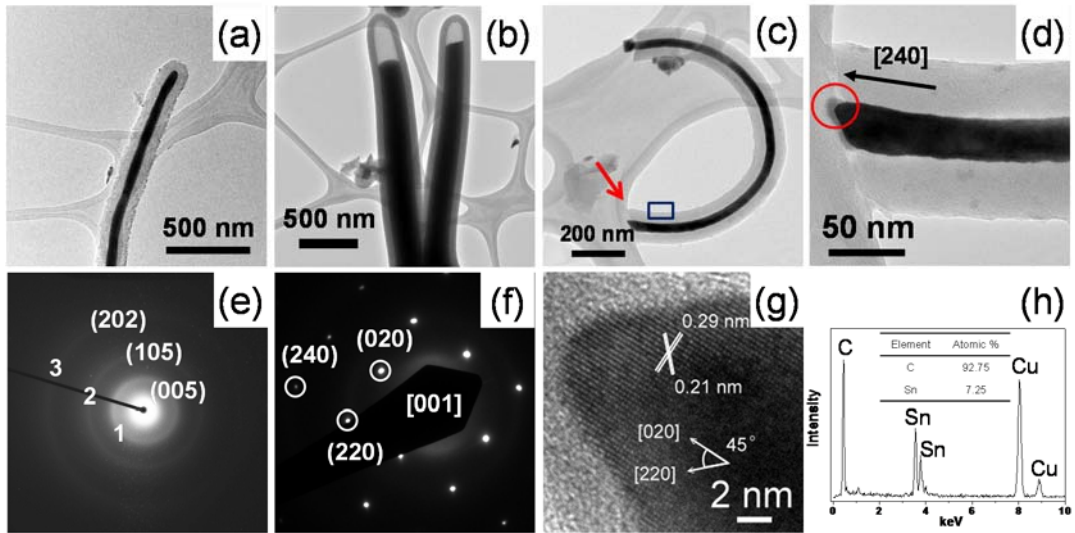


Figure 4.7 TEM studies of product A. (a) A completely filled core-shell NW, (b) a pair of partially filled NWs, (c) a section of a broken NW, (d) a high magnification image from the pointed region in (c), (e) SAED pattern from the rectangle area in (c) and (f) SAED pattern from the end of the core in (d). (g) HRTEM image from the region circled in (d). (h) EDX spectrum from (c).

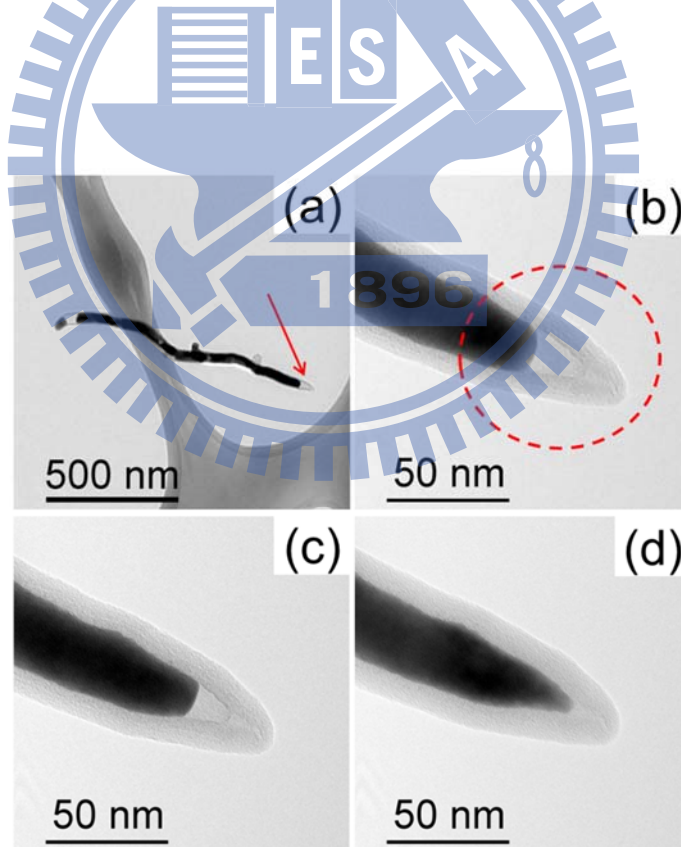


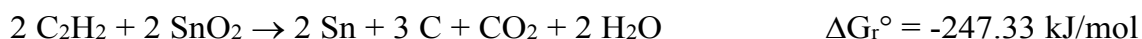
Figure 4.8 TEM images of a Sn@C core-shell NW. (a) Low magnification image and (b) high magnification view of the area marked by the arrow in (a) images taken after irradiating the circled area in (b) by an electron beam for (c) 60 s and (d) 180 s. The void shown in the circled area in (b) was filled by melted Sn after the electron beam irradiation.

4.3.2 Proposed reaction pathway

Growth of the Sn@C core-shell NWs is further discussed below to illustrate the important features of the reaction. The overall reaction stoichiometry between C₂H₂ and SnO₂ to produce Sn and C could be either

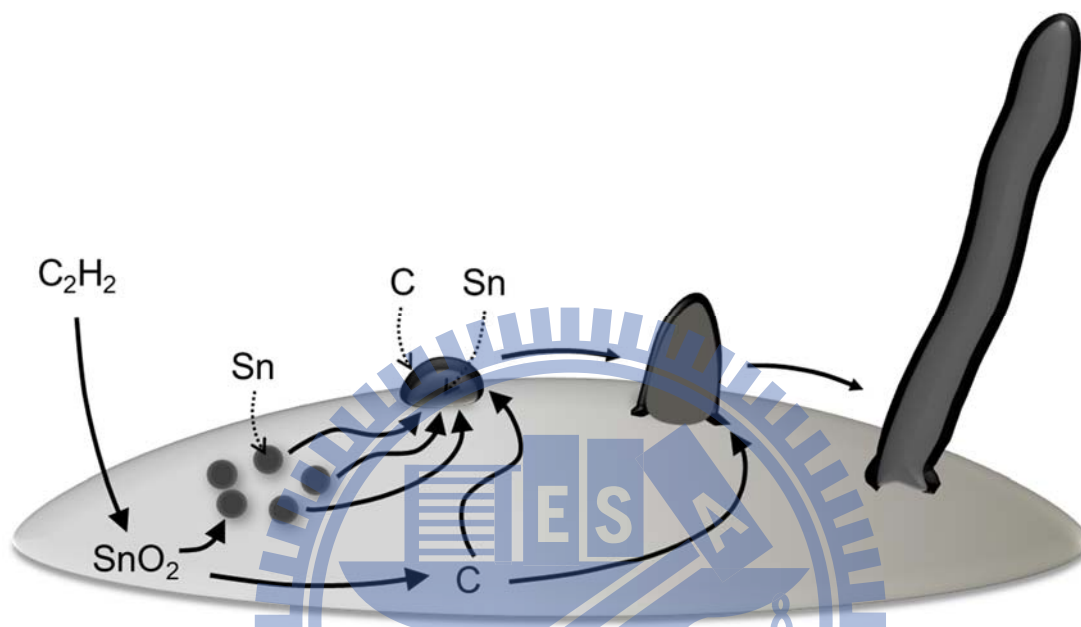


or



Both reactions are thermodynamically favored due to the negative standard Gibbs free energies of reaction (ΔG_r°).³⁵ In addition, we suggest that the core-shell NWs are grown via a VSRG pathway shown in Scheme 4.1. It is analogous to the ones proposed before for the growths of 1D CaF₂@ α -C NWs and SiC tubes.^{29,30} The reaction happens at the interface between the vapor phase C₂H₂ and the surface of the SnO₂ solid. From the SEM image displayed in the inset in Figure 4.6a, it is discovered that the oxide can be reduced to metallic Sn at 873 K.³⁶ Due to their large difference in surface energies, the as-formed products are composed of phase-separated Sn and C nanoparticles (NPs). As the Sn NPs coalesce to generate a core, the C NPs covered the Sn surface to form a shell. After more Sn and C products migrate and incorporate into this heterostructured seed, the high melting point C shell solidifies even though the low melting point Sn core stays in the liquid state. Since the solidified C shell possesses a certain width, incorporation of more products into the growing heterostructure can only extend one dimensionally into the observed core-shell NW morphology. In the experiments, growth of small diameter core-shell NWs is observed at 923 K, as shown in Figure 4.6b. It is known that as the size of a nanomaterial increases, its melting point increases as well. Thus, we anticipate that the NWs grown at higher temperatures should have larger diameters. This is supported by the observations shown in Figure 4.1b and 4.1d and the data summarized in Table 4.2. The diameters of the NWs in A, grown at 973 K, are wider than those of B, grown at 923 K. The images in Figure 4.6b–d also demonstrate that as the growth temperature is

increased from 923 K to 1123 K, more and wider NWs are formed. It is worthwhile to mention that the proposed VSRG reaction proceeds *via* steps very different from the ones in typical vapor–liquid–solid (VLS) type growths.³⁷



Scheme 4.1 Proposed VSRG pathway to form Sn@C core–shell NWs.

4.3.3 Electrochemical properties of Sn@C core–shell NWs

According to the literature, employing SnO₂ and Sn for anode applications in LIBs presents several drawbacks. These include the irreversibility associated with the SnO₂ reduction, the capacity losses due to the formation of the solid electrolyte interface (SEI) on the Sn surfaces, and large volume variations during the Li⁺ insertion and extraction reaction steps.^{38–40} For the Sn@C core–shell NWs prepared in this study, we performed the following electrochemical studies. Half-cells composed of a Li foil, as the negative electrode (anode), and Sn@C core–shell NWs, as the positive electrode (cathode), were assembled into test cells. In Figure 4.9a, the first cyclic voltammetric (CV) profile of the NWs shows a reduction peak (cathodic scan) at 1.52 V. The peak is irreversible because it disappears in the later cycles. One possible origin

of the peak was from the SEI on Sn.⁴¹ However, another signal peak at 1.05 V usually accompanies the one near 1.52 V. In addition, since most of the Sn containing nanostructures are wrapped inside the C shells, it is less likely that the SEI could form on the Sn surface. The peak at 1.52 V cannot be assigned to the SEI on the C shells either because the reported signals were at 0.80 and 1.25 V.⁴¹ Thus, we ascribe the peak at 1.52 V to the formation of LiOH due to the presence of traces of H₂O in the electrolyte.⁴² The other reduction peaks are observed at 0.58 V, 0.46 V and 0.30 V during the discharging/alloying step while the oxidation peaks (anodic scan) are found at 0.54 V, 0.71 V, 0.80 V and 0.85 V during the charging/dealloying step. These are correlated with the interconversions among Sn and several Li_xSn (0 ≤ x ≤ 4.4) phases, including Li₂Sn₅, LiSn, Li₇Sn₃, Li₅Sn₂, Li₁₃Sn₅, Li₇Sn₂, and Li_{4.4}Sn.^{10,17,43,44} Previous studies indicated that primary lithiation and delithiation processes of amorphous carbon and graphite materials usually occurred below 0.25 V while amorphous carbon nanotube (CNT) and single-wall CNT showed Li deintercalation at 0.9-1.2 V.⁴⁵⁻⁵⁰ The CV profiles in Figure 4.9a display gradual current decreases below 0.25 V and no clear deintercalation peaks at 0.9-1.2 V in the initial cycles. The observations suggest that Li⁺ ions probably accumulate irreversibly in the carbon shells.

Figure 4.9b displays the voltage profiles of the half-cell made of the Sn@C NWs. The data were taken at a cycling rate of 500 mA g⁻¹ and between 0.005 and 2.00 V versus Li/Li⁺. The voltage profiles indicate that the NW electrode exhibits the characteristics of a Sn electrode.¹⁰ The first discharge and charge steps deliver specific capacities of 1760 and 1405 mA h g⁻¹, respectively. They correspond to a coulombic efficiency of 80%. The large initial capacity loss can be attributed, as mentioned above, to the formation of the SEI layer on the electrode surface during the first discharge step and the storage of Li⁺ ions in EC/DMC-based electrolytes, which are difficult to be extracted.^{10,17,39} The presence of multiple plateaus in the initial discharge-charge curves is assigned to the formation and decomposition of Li_xSn.^{43,44} In the following cycles, the plateaus become less and less discernible. For example, the plateaus at 0.58 V (the

transition between Sn and LiSn phases) and 0.46 V (the transition between LiSn and Li₇Sn₃ phases) decrease gradually with increasing cycle numbers. These observations agree with the CV results. They suggest that Li⁺ ions stored in the related Li_xSn phases may not undergo reversible cycling. The discharge capacities are found to be 1384, 804, 582, 515 and 490 mA h g⁻¹ at the second, tenth, twenty-fifth, fiftieth and one hundredth cycles, respectively.

Figure 4.9c depicts the specific capacity and the coulombic efficiency of the discharge-charge process of the half-cell with a cycling rate at a current density of 500 mA g⁻¹. Obviously, the capacity dropped swiftly for the first ten cycles. As discussed above, there are several possible pathways which may provide irreversible storage of Li⁺ ions. These include the formation of the SEI layer, the decomposition of electrolytes, and the accumulation of Li⁺ ions in carbon and tin materials. They offer an apparent capacity which exceeds the theoretical value. Between the twenty-fifth and the fiftieth cycles, the half-cell remains stable during the cycling and exhibits a fade rate of 0.47% per cycle. The half-cell continues to be stable for the next fifty cycles with a fade rate of 0.09% per cycle. The specific capacity is 490 mA h g⁻¹ at the end of the one hundredth cycle. The coulombic efficiency remains relatively stable at over 98% after the twenty-fifth cycle. In contrast, the cycling performance of a half-cell constructed from commercial Sn powders (particle size distribution 1–10 μm)

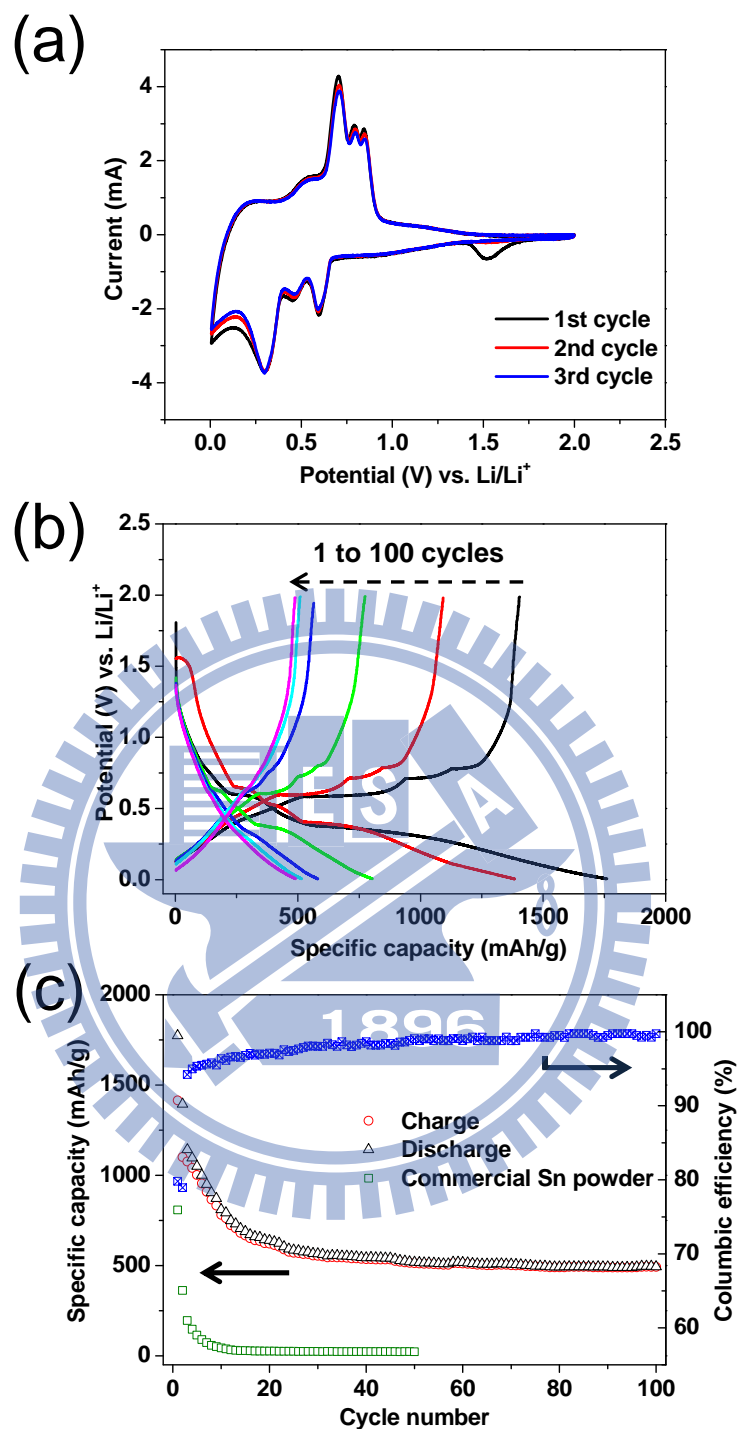


Figure 4.9 (a) Cyclic voltammograms of a Sn@C core-shell NW electrode (scan speed 0.5 mV s^{-1}). Electrochemical performance of the electrode cycled between 0.005 V and $2.0 \text{ V vs. Li/Li}^+$ (cycling rate 500 mA g^{-1}); (b) voltage profiles of the electrode after 1, 2, 10, 25, 50, and 100 cycles and (c) capacity fading of the electrode. Coulombic efficiency and reversibility of each cycle of the electrode are presented in the secondary y-axis on the right of (c). The discharge capacity of an electrode fabricated from commercial Sn powder was cycled at 100 mA g^{-1} .

Figure 4.10 shows the cycling rate capability of the half-cell constructed from the Sn@C core-shell NWs with a voltage window of 0.005–2.0 V. Figure 4.10 shows the discharge capacities of the device at current densities of 100, 500, 1000, and 3000 mA g⁻¹. After one hundred cycles, the discharge (Li alloying) capacities at these rates are 525, 490, 486, and 286 mA h g⁻¹, respectively. Both of the discharge capacities at 500 and 1000 mA g⁻¹, compared to the one at 100 mA g⁻¹, are about 93%. Even at 3000 mA g⁻¹, 55% of the capacity at 100 mA g⁻¹ remained. In Figure 4.10, a capacity of 905 mA h g⁻¹ is observed after the battery is cycled at 100 mA g⁻¹ for five times. Then, after continued cycling at 500 mA g⁻¹, 1000 mA g⁻¹, and finally 3000 mA g⁻¹ for five times each, the half-cell returns back to 626 mA h g⁻¹ at 100 mA g⁻¹. This demonstrates that even after fast discharge-charge cycles at 3000 mA g⁻¹, the electrode was not severely degraded and the half-cell still exhibited excellent cycling properties. Consequently, we conclude that the improved electrochemical performance of the half-cell is rooted in the special morphology of the Sn@C core-shell NWs.

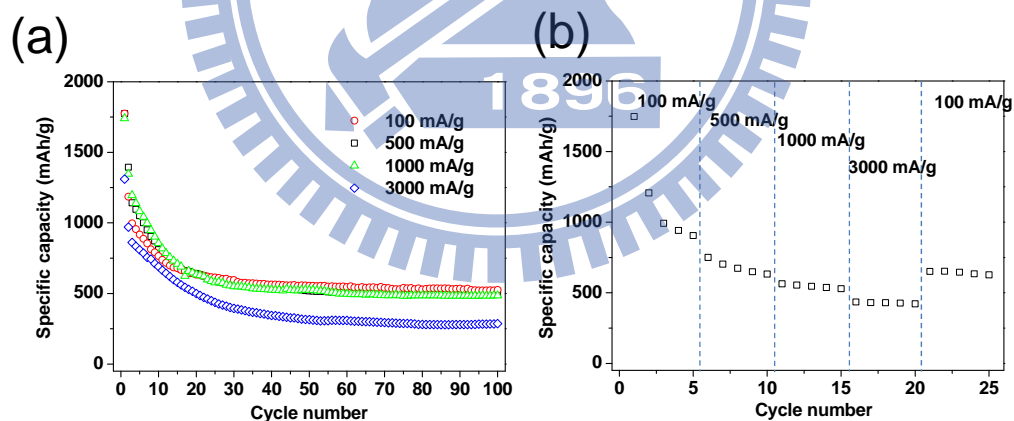


Figure 4.10 Electrochemical performance of a Sn@C core-shell NW electrode cycled between 0.005 V and 2.0 V vs. Li/Li⁺. (a) Curves of specific capacity versus cycle number of the electrode at cycling rates of 100 mA g⁻¹, 500 mA g⁻¹, 1000 mA g⁻¹ and 3000mA g⁻¹. (b) Discharge capacities of the electrode as a function of discharge rates (100–3000 mA g⁻¹).

The NW structure may shorten the transport lengths for both electrons and Li⁺ ions. The C shell layer probably acts as a good electronic conductor and serves as a buffer for the volume change during the lithiation-delithiation process. Figure 4.11a and 4.11b shows the images of

the as-prepared electrode material containing the Sn@C core-shell NWs. After one hundred discharge-charge cycles at 500 mA g⁻¹ (cycled between 0.005 and 2.0 V), many Sn@C core-shell NWs still maintain original diameters with clear core-shell structures in Figure 4.11c and 4.11d. Clearly, the volume expansion caused by the lithiation of the Sn cores was confined within the C shells. Two possible reasons are proposed to rationalize the observed confinements. One of them is attributed to the voids observed in Figure 4.1 and 4.7, which may accommodate some of the expansions. The other one may originate from the flexible amorphous C shells which could be deformed extensively during the volume variations.⁵¹ In Figure 4.11c and 4.11d, only some NWs are found to be destructed into aggregated particles, probably due to non-uniform volume changes. On the other hand, as shown in Figure 4.12, the electrode fabricated from commercial Sn powders shows severe aggregations after fifty discharge-charge cycles. Because the NWs retain most of the original morphology, they exhibit better battery performance than the Sn particles do. Comparison of our results to other literature reports is discussed below.

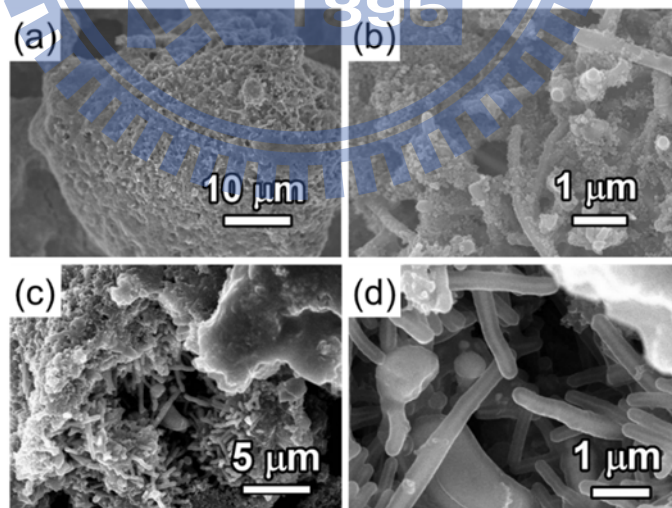


Figure 4.11 SEM images of the electrode prepared from Sn@C core-shell NWs. (a) Low and (b) high magnification views. (c) Low and (d) high magnification views of the electrode after 100 cycles of lithiation and delithiation. The electrode was fabricated with a mixture of carbon black and binder.

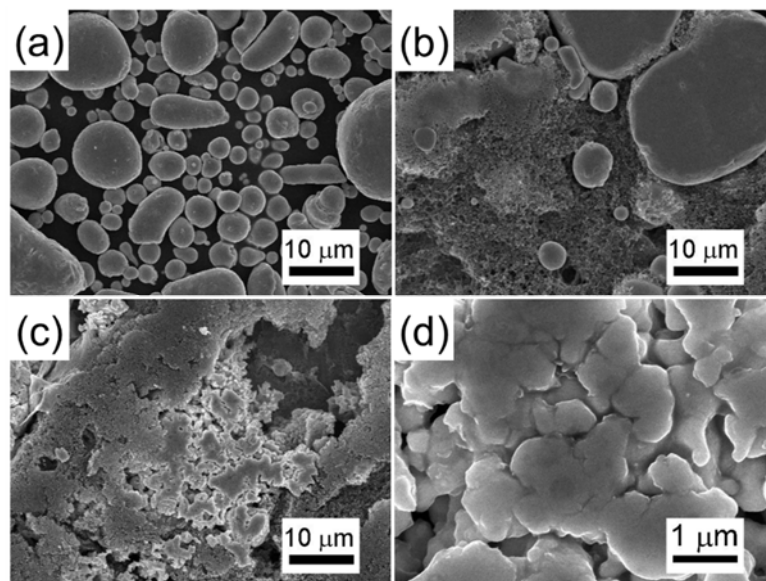


Figure 4.12 SEM images of (a) the commercial Sn powder, (b) the electrode prepared from the powder, and (c) low and (d) high magnification views of the electrode after 50 cycles of lithiation and delithiation. The Sn particles shown in (b) and (c) were mixed with carbon black and binder used for the electrode fabrication.

Employing SnO₂ as a potential anode material for LIBs has been attempted in many studies.^{21,22} Unfortunately, the oxide suffered from a high first-cycle irreversible capacity during the first charging because it has to be reduced to metallic Sn. To solve this problem, it is anticipated that metallic Sn could be applied directly. However, utilizing the metal presents another difficulty as discussed earlier. It undergoes enormous volume variation during the Li alloying and dealloying processes.^{17,20} One possible solution for this is to use nanostructured hollow and/or porous Sn containing materials. It is anticipated that the local empty spaces may accommodate the large volume change.^{52,53} Another possible answer is to restrain the active phases by controlling the size and morphology of the electrode materials. To achieve these, many nanostructured core-shell and composite materials have been developed.^{9-11,25} Literature reports related to solving the issues are summarized in Table 4.1. For example, the initial capacity of SnO₂ nanotubes (NTs) was 940 mA h g⁻¹. After eighty cycles at 0.05 mA cm⁻², a capacity of 525 mA h g⁻¹ was retained, corresponding to 55.8% of the initial value.²¹ In another example, SnO₂-core/C-shell NTs were investigated.²² This nanocomposite could be repeatedly

charged and discharged up to two hundred cycles with a capacity of 542 mA h g⁻¹ at 0.3 mA cm⁻². Some Sn metal containing cases presented in Table 4.1 are discussed below. For hydrobenzamide-capped Sn, a charge capacity of 500 mA h g⁻¹ was observed after thirty cycles at 0.2C.²³ In the second case, electrochemical tests of vertical arrays of 1D Sn NWs on Si substrates showed that a discharge capacity of 400 mA h g⁻¹ could be maintained after fifteen cycles at a high discharge-charge rate of 4200 mA g⁻¹.²⁴ Cases of Sn@C@CNT nanostructures and rambutan-like Sn–C nanocomposites offered capacities of 490 mA h g⁻¹ and 311 mA h g⁻¹, respectively.^{9,10} Lastly, examples of nanocomposites of Sn and Group 11 metals are presented. Sn@Cu core–shell NPs retained a capacity of 560 mA h g⁻¹ after one hundred seventy cycles at a rate of 0.8C.²⁵ The discharge capacity of Sn NPs supported on nanoporous Au was found to be 440 mA h g⁻¹ after one hundred forty cycles at 0.1C.¹¹ Performance of the devices fabricated from our core–shell NWs compares favorably against the results of the better ones shown in Table 4.1. The capacity of 525 mA h g⁻¹ was retained after one hundred cycles at a rate of 100 mA g⁻¹. Even at a high rate of 1000 mA g⁻¹ for one hundred cycles, our cell maintained a capacity of 486 mA h g⁻¹.

4.4 Conclusions

In summary, we have fabricated Sn@C core–shell NWs in high yields by a simple and straightforward process. By reacting vapor phase C₂H₂ with SnO₂ solids, we grew the 1D NWs *via* the VSRG pathway. Due to the unique 1D core–shell morphology, which provides an adequate void volume inside the flexible C shell, the NWs can respond to the large volume change caused by the formation and decomposition of Li_xSn alloys in the charge–discharge steps in LIBs. The electrodes show high reversible capacities, low rates of capacity fading, and consistent cycling performance.

4.5 References

1. M. Armand and J. M. Tarascon, *Nature*, 2008, **451**, 652.

2. B. Kang and G. Ceder, *Nature*, 2009, **458**, 190.
3. M. S. Whittingham, *MRS Bull.*, 2008, **33**, 411.
4. P. L. Taberna, S. Mitra, P. Poizot, P. Simon and J. M. Tarascon, *Nat Mater*, 2006, **5**, 567.
5. L.-F. Cui, R. Ruffo, C. K. Chan, H. Peng and Y. Cui, *Nano Lett.*, 2008, **9**, 491.
6. Y. Oumellal, A. Rougier, G. A. Nazri, J. M. Tarascon and L. Aymard, *Nat. Mater.*, 2008, **7**, 916.
7. Y.-K. Sun, S.-T. Myung, B.-C. Park, J. Prakash, I. Belharouak and K. Amine, *Nat. Mater.*, 2009, **8**, 320.
8. B. L. Ellis, K. T. Lee and L. F. Nazar, *Chem. Mater.*, 2010, **22**, 691.
9. Y. Wang, M. Wu, Z. Jiao and J. Y. Lee, *Chem. Mater.*, 2009, **21**, 3210.
10. D. Deng and J. Y. Lee, *Angew. Chem. Int. Ed.*, 2009, **48**, 1660.
11. Y. Yu, L. Gu, X. Lang, C. Zhu, T. Fujita, M. Chen and J. Maier, *Adv. Mater.*, 2011, **23**, 2443.
12. P. Wu, N. Du, J. Liu, H. Zhang, J. Yu and D. Yang, *Mater. Res. Bull.*, 2011, **46**, 2278.
13. B.-S. Lee, S.-B. Son, K.-M. Park, J.-H. Seo, S.-H. Lee, I.-S. Choi, K.-H. Oh and W.-R. Yu, *J. Power Sources*, 2012, **206**, 267.
14. G. Derrien, J. Hassoun, S. Panero and B. Scrosati, *Adv. Mater.*, 2007, **19**, 2336.
15. H. Nara, Y. Fukuhara, A. Takai, M. Komatsu, H. Mukaibo, Y. Yamauchi, T. Momma, K. Kuroda and T. Osaka, *Chem. Lett.*, 2008, **37**, 142.
16. I. A. Courtney, J. S. Tse, O. Mao, J. Hafner and J. R. Dahn, *Phy. Rev. B: Condens. Matter Mater. Phys.*, 1998, **58**, 15583.
17. M. Winter and J. O. Besenhard, *Electrochim. Acta*, 1999, **45**, 31.
18. M. Winter, G. H. Wrodnigg, J. O. Besenhard, W. Biberacher and P. Novak, *J. Electrochem. Soc.*, 2000, **147**, 2427.
19. M. Wachtler, M. Winter and J. O. Besenhard, *J. Power Sources*, 2002, **105**, 151.

20. B. Veeraraghavan, A. Durairajan, B. Haran, B. Popov and R. Guidotti, *J. Electrochem. Soc.*, 2002, 149, A675.
21. Y. Wang, J. Y. Lee and H. C. Zeng, *Chem. Mater.*, 2005, 17, 3899.
22. Y. Wang, H. C. Zeng and J. Y. Lee, *Adv. Mater.*, 2006, 18, 645.
23. Y. Kwon, M. G. Kim, Y. Kim, Y. Lee and J. Cho, *Electrochem. Solid-State Lett.*, 2006, 9, A34.
24. J.-H. Kim, S. Khanal, M. Islam, A. Khatri and D. Choi, *Electrochem. Commun.*, 2008, 10, 1688.
25. M. G. Kim, S. Sim and J. Cho, *Adv. Mater.*, 2010, 22, 5154.
26. K. T. Lee, Y. S. Jung and S. M. Oh, *J. Am. Chem. Soc.*, 2003, 125, 5652.
27. M. Y. Yen, C. W. Chiu, C. H. Hsia, F. R. Chen, J. J. Kai, C. Y. Lee and H. T. Chiu, *Adv. Mater.*, 2003, 15, 235.
28. C.-H. Hsia, M.-Y. Yen, C.-C. Lin, H.-T. Chiu and C.-Y. Lee, *J. Am. Chem. Soc.*, 2003, 125, 9940.
29. C.-H. Huang, Y.-H. Chang, C.-Y. Lee and H.-T. Chiu, *Langmuir*, 2005, 22, 10.
30. C.-H. Wang, H.-K. Lin, T.-Y. Ke, T.-J. Palathinkal, N.-H. Tai, I. N. Lin, C.-Y. Lee and H.-T. Chiu, *Chem. Mater.*, 2007, 19, 3956.
31. Joint Committee for Powder Diffraction (JCPDS) File No. 86-2265 and File No. 72-1147. International Center for Diffraction Data, 2002.
32. Y. Wang, D. C. Alsmeyer and R. L. McCreery, *Chem. Mater.*, 1990, 2, 557.
33. J. Schwan, S. Ulrich, V. Batori, H. Ehrhardt and S. R. P. Silva, *J. Appl. Phys.*, 1996, 80, 440.
34. Z. Ying, Q. Wan, Z. T. Song and S. L. Feng, *Nanotechnology*, 2004, 15, 1682.
35. Reaction-Web, Facility for the Analysis of Chemical Thermo-dynamics; CRCT, <http://www.crct.polymtl.ca>.
36. X. M. Sun, J. F. Liu and Y. D. Li, *Chem. Mater.*, 2006, 18, 3486.

37. R. S. Wagner and W. C. Ellis, *Appl. Phys. Lett.*, 1964, 4, 89.
38. I. A. Courtney, W. R. McKinnon and J. R. Dahn, *J. Electrochem. Soc.*, 1999, 146, 59.
39. P. Meduri, C. Pendyala, V. Kumar, G. U. Sumanasekera and M. K. Sunkara, *Nano Lett.*, 2009, 9, 612.
40. N. C. Li, C. R. Martin and B. Scrosati, *Electrochem. Solid-State Lett.*, 2000, 3, 316.
41. Y. S. Jung, K. T. Lee, J. H. Ryu, D. Im and S. M. Oh, *J. Electrochem. Soc.*, 2005, 152, A1452.
42. D. Aurbach, A. Zaban, Y. Ein-Eli, I. Weissman, O. Chusid, B. Markovsky, M. Levi, E. Levi, A. Schechter and E. Granot, *J. Power Sources*, 1997, 68, 91.
43. J. L. Tirado, R. Santamaría, G. F. Ortiz, R. Menéndez, P. Lavela, J. M. Jiménez-Mateos, F. J. Gómez García, A. Concheso and R. Alcántara, *Carbon*, 2007, 45, 1396.
44. W.-M. Zhang, J.-S. Hu, Y.-G. Guo, S.-F. Zheng, L.-S. Zhong, W.-G. Song and L.-J. Wan, *Adv. Mater.*, 2008, 20, 1160.
45. M. M. Thackeray, *Handbook of Battery Materials*, Wiley-VCH, Weinheim, 1999.
46. G.-A. Nazri, G. Pistoia, *Lithium Batteries: Science and Technology*, Kluwer Academic Plenum, Boston, 2004, 144.
47. R. A. Huggins, *Advanced Batteries: Materials Science Aspects*, Springer, New York, 2009, 131.
48. D. Aurbach, B. Markovsky, I. Weissman, E. Levi and Y. Ein-Eli, *Electrochim. Acta*, 1999, 45, 67.
49. G. T. Wu, C. S. Wang, X. B. Zhang, H. S. Yang, Z. F. Qi, P. M. He and W. Z. Li, *J. Electrochem. Soc.*, 1999, 146, 1696.
50. D. Ahn, X. Xiao, Y. Li, A. K. Sachdev, H. W. Park, A. Yu and Z. Chen, *J. Power Sources*, 2012, 212, 66.
51. J. W. Suk, S. Murali, J. An and R. S. Ruoff, *Carbon*, 2012, 50, 2220.

52. X. W. Lou, Y. Wang, C. Yuan, J. Y. Lee and L. A. Archer, *Adv. Mater.*, 2006, 18, 2325.

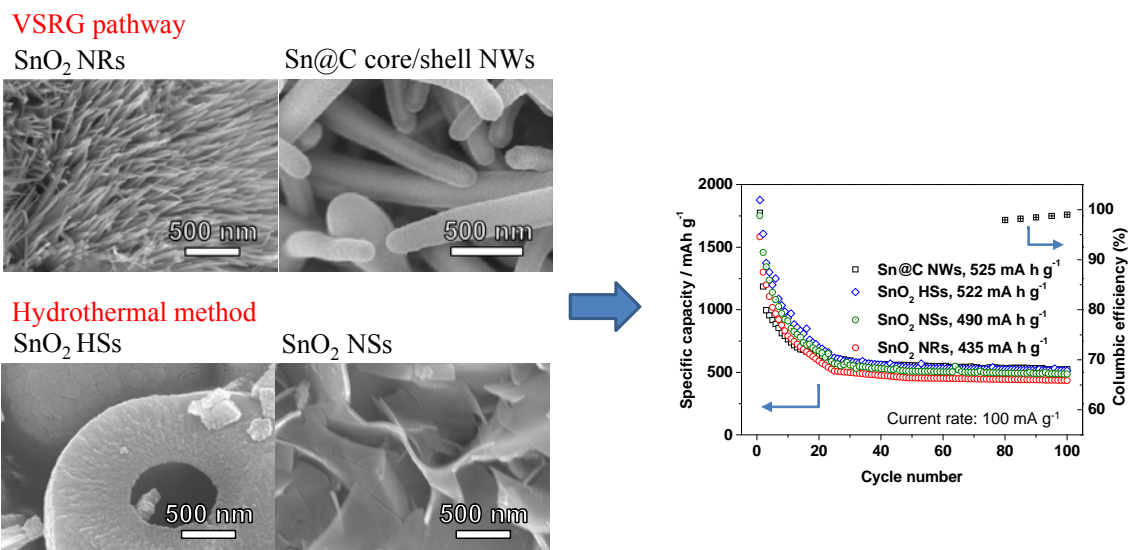
53. X. W. Lou, D. Deng, J. Y. Lee and L. A. Archer, *Chem. Mater.*, 2008, 20, 6562.



Chapter 5 Conclusions

In this thesis, we demonstrated a facile simple, and low cost fabrication of tin-based nanomaterials, including as SnO₂ nanorods, SnO₂ hollow spheres, SnO₂ nanosheets and Sn@C core-shell nanowires. Report a unique reaction employing vapor phase and solid particles as the reactants, one-dimensional SnO₂ nanorods and Sn@C core-shell nanowires are formed *via* vapor-solid reaction growth pathway. SnO₂ hollow spheres and nanosheets could be controlled by Sn^{+4/+2} precursors *via* a simple one-pot template-free hydrothermal method. These are summarized in Scheme 5.1. The SnO₂ nanorods were length 1-2 μm and diameter 10-20 nm. The shell thickness of the hollow spheres was around 200 nm with diameter 1-3 μm, while thickness of the nanosheets was 40 nm. The Sn@C core-shell nanowires was 100-350 nm with 30-70 nm C shell thickness and length was several micrometers.

The effect of morphological modification on the electrochemical properties of tin-based nanomaterials for LIBs were further evaluated. Based on the results, reducing the active particle size to the nanometer range and using the specific morphology of active materials can significantly improve the cycling performance. Also, propose a conception that due to the even distribution of the voids among the inactive matrix, the mechanical stress caused by the volume changes could be alleviated during cycles. At the end of the one hundredth cycle, the specific capacity and the columbic efficiency stay relatively stable and the columbic efficiency over 98% are observed. The specific capacity of SnO₂ nanorods, SnO₂ hollow spheres, SnO₂ nanosheets and Sn@C core-shell nanowires are 435, 522, 490 and 525 mA h g⁻¹, respectively. In contrast, the cycling performances of commercial tin-based powders are poor. We anticipate that the tin-based nanomaterials can be utilized for LIBs upon further optimization.



Scheme 5.1 Illustration of tin-based nanostructures as electrochemical test for LIBs.

